Study on the Performance of Linear Fresnel Solar Collector with Sensible Thermal Energy Storage for Industrial Process Heat Generation

By

Betsegaw Gashu Kefa

A Thesis Submitted to

Thermal and Aerospace Engineering Program

School of Mechanical, Chemical and Material Engineering

Presented in partial fulfillment of the requirement for the degree of Master of Science in Thermal Engineering

Adama Science and Technology University

Adama, Ethiopia

October, 2019

Study on the Performance of Linear Fresnel Solar Collector with Sensible Thermal Energy Storage for Industrial Process Heat Generation

By: Betsegaw Gashu Kefa

Advisor: Dr. Gezahegn Habtamu

A Thesis Submitted to

Thermal and Aerospace Engineering Program

School of Mechanical, Chemical and Material Engineering

Presented in partial fulfillment of the requirement for the degree of Master of Science in Thermal Engineering

Adama Science and Technology University

Adama, Ethiopia

October, 2019

Declaration

I hereby declare that this M.Sc. Thesis entitled "Study on the Performance of Linear Fresnel Solar Collector with Sensible Thermal Energy Storage for Industrial Process Heat Generation" in partial fulfillment of the requirement of the degree of Master of Science in Thermal Engineering is an authentic record of my own work carried out from September 2018 to October 2019 under supervision of Dr. Gezahegn Habtamu, Assistant Professor of Thermal Engineering program, Adama Science and Technology University.

The matter embedded in this thesis has not been submitted for the award of a degree or diploma in any other university. All relevant resource information used in this paper has been duly acknowledged.

....	....	....
Student	Signature	Date

This is to certify that the above statement made by the candidate is correct to the best of our knowledge and belief. This has been submitted for examination with our approval.

....	....	....
Advisor	Signature	Date

Adama Science and Technology University

School of Mechanical, Chemical and Materials Engineering

Thermal and Aerospace Engineering Program

Approval of Board of Examiners

We, the undersigned, members of the Board of Examiners of the final open defense by Betsegaw Gashu Kefa have read and evaluated his thesis entitled "**Study on the Performance of Linear Fresnel Solar Collector with Sensible Thermal Energy Storage for Industrial Process Heat Generation**" and examined the candidate. This is, therefore, to certify that the thesis has been accepted in partial fulfillment of the requirement of the Degree of Master of science in Thermal Engineering.

………………………………….......	……………………………..	………………….
Chair person	Signature	Date
………………………………….......	……………………………..	………………….
Internal Examiner	Signature	Date
………………………………….......	……………………………..	………………….
External Examiner	Signature	Date

ACKNOWLEDGMENT

First and foremost, I would like to thank my Lord Jesus Christ for giving me the strength, knowledge, ability and opportunity to undertake this research study and to persevere and complete it successfully. Without his blessings, this achievement would not have been possible.

I am very grateful to my advisor Dr. Gezahegn Habtamu, for his inspiration, guidance, support and valuable instructions at all times.

I would like to thank my families and friends for they have been beside me all the time and supported, encouraged, and motivated me. Special thanks to my brother Natnael Gashu for his help in computer programming.

Many thanks to Ato Abera Dagnachew and his colleagues from Ah-Wan Food Complex. They have given me all the valuable information I need during my study.

ABSTRACT

Solar thermal energy to supply process heat in different industrial sectors has become very promising in recent years. Industries can reduce their fuel consumption by replacing them with solar process heat with non-conventional system integration and using clean energy.

Ah-Wan Food Complex is an industry with higher thermal energy consumption which is mainly used in the drying stage of the pasta production. Superheated water at 140 °C and 4.5 bar is used to control the temperature and humidity conditions of a pasta drying tunnel. Currently, the industry uses a conventional boiler which has a capacity of 11kg/s with average annual fuel consumption of 740,918 liters, costing approximately 12 million Birr. This energy demand can be replaced partially or wholly by a solar thermal system.

This thesis presents a performance analysis of solar thermal system consists of a linear Fresnel collector and concrete thermal energy storage for industrial process heat generation based on energy requirement of Ah-Wan Food Complex. A one-dimensional transient numerical model is developed for the linear Fresnel collector accounting of optical and thermal losses and coping up with the intermittent and inherent variable solar input. In addition to that, a transient numerical model is developed for concrete thermal energy storage which is integrated with the collector. The models were solved using a finite difference scheme which is implemented in a Python program. Based on the results from the numerical results in Adama metrological conditions 120 modules of Linear Fresnel collector with an aperture area of 2838 m^2 can fulfill the daily energy requirement of the factory (with 6 hours of thermal energy storage). Besides, 98 m^3 of concrete thermal energy storage is required for 6 hours of thermal energy storage. It is also noticed that the mass flow rate is the main parameter to control the output temperature from the collector.

Keywords: Solar thermal, Process heat, Linear Fresnel collector, Concrete, Thermal energy storage

TABLE OF CONTENTS

CONTENTS PAGE

LIST OF FIGURES

LIST OF TABLES

NOMENCLATURE

ABBREVIATIONS

CFD	Computational fluid dynamics
CPC	Compound parabolic concentrator
CSP	Concentrating solar power
GPS	Global positioning system
HEX	Heat exchanger
HTF	Heat transfer fluid
IAM	Incident Angle Modifier
LF	Linear Fresnel
LFC	Linear Fresnel collector
PTC	Parabolic trough collector
TES	Thermal energy storage

SYMBOLS

A	Area (m^2)
$\overline{H}$	Monthly average daily global radiation on a horizontal surface (W/m^2)
C	Specific heat capacity (J/kgK), Concentration ratio
D, d	Diameter (m)
DR	Diameter ratio
E	Equation of time
F	Focal distance (m)
H	Global radiation (W/m^2)
g	Gravity (m/s^2)
h	Convective heat transfer coefficient (W/m^2K)
I	monthly average hourly radiation on a horizontal surface
k	Thermal conductivity (W/mK)
L	Length, Effective length (m)

m	Mass (kg)
$\dot{m}$	Mass flow rate (kg/s)
n	Day of the year
N	Day time duration
Nu	Nusselt number
P	Perimeter (m), Pressure (Pa)
Pr	Prandtl number
Q	Heat flow (W), flow rate (kg/m^3)
q	Heat transfer per length (W/m)
R, r	Radius (m)
Ra	Rayleigh number
Re	Reynolds number
ST	Solar time (hr)
T	Temperature (K or ^oC)
t	Time (s)
U	Speed (m/s)
V	Volume (m^3)
W	Width (m)
f	Friction factor

GREEK LETTERS

α_s	Solar altitude
γs	Solar azimuth
Δ	Change
α	Thermal diffusivity, Absorptivity
β	Volumetric thermal expansion coefficient
γ	Intercept factor
δ	Declination angle

ε	Emittance
λ	Specific latent heat
μ	Dynamic viscosity
ν	Kinematic viscosity
ρ	Density
τ	Transmissivity
ψ	Tracking angle
ω	Hour angle
η	Efficiency
σ	Stefan-Boltzmann constant
θ	Incident angle
φ	Latitude angle, Position angle

SUBSCRIPTS

ABS	Absorber
amb	Ambient air
air	Air
ap	Aperture
atm	Atmospheric
b	Beam
block	Blocking loss
clean	Cleaning loss
conv	Convection
cosine	Cosine loss
crit	Critical
d	Diffuse
b	Beam
E	Effective
end	End loss
external	Heat transfer to environment
gained	Gained energy
GC	Glass cover
HTF	Heat transfer fluid
I	Irradiance
i	Internal
in	Inlet
L	Longitudinal
max	Maximum
min	Minimum
o	Outer
opt	Optical
out	Outlet
rad	Radiation heat transfer
s	Solid

shad	Shading loss
Sr	Sunrise
Ss	Sunset
T	Transversal
th	Thermal
t	Time
tot	Total
u	Useful
z	Zenith

CHAPTER ONE

INTRODUCTION

1.1 Background

According to U.S. Energy Information Administration (EIA) (2017), industries are responsible for around one-third of the total energy demand in the world. The major share of industrial energy demand is pertained to heat for industrial processes which are in the lower and medium temperature range. This reality does not only cause a release of a significant amount of CO_2, but it is also a substantial cost factor. Thus, as fuel prices continue to rise, industrial energy supply ultimately also affects the competitiveness of countries and industries. Solar energy is certainly the most considerable renewable and clean energy with the reserves of fossil energy decreasing, while the consumption increasing.

In Ethiopia, as the number of industries are growing drastically the process heat energy demand is also increasing. However, the use of renewable energy sources like solar energy is at its infancy stage. As a growing country, developing a technological trend of using renewable energy sources is very essential. One of the main potential areas of using renewable energy (specifically solar energy) is industrial process heating. This heat energy requirement can be obtained by using concentrated solar energy collectors, among other solar heating technologies.

Concentrated solar collectors are the most widely used solar collectors used in industries for process heating due to their high-quality solar power. Parabolic trough collectors and linear Fresnel collectors are the most common of this type and there are a number of manufacturers in different parts of the globe. Parabolic trough collectors are the most matured of the concentrating solar power technologies and the majority of worldwide installed capacity is of this type. They offer an acceptable performance level but some limitations do still exist. The curved mirrors are relatively expensive and aspects such as the need for flexible couplings and strong foundations to combat wind loads result in a high cost per kWh. The scope for future cost reduction is also limited.

The other line focusing type, the linear Fresnel collector (LFC), is comparatively new and offers much potential for cost reduction. It is projected to have a lower investment cost per kWh. The technology also uses simpler parts that could be manufactured locally. Small-sized linear Fresnel reflectors meet the medium temperature ranges (100 – 250^{o}C) for the generation of industrial process heat (Kalagirou, 2009). In addition, integration of this collectors with storage systems can substantially enhance their performance and feasibility for industrial use.

There are so many industries in Adama city that uses fuel or electricity for generating industry process heat. Since solar energy is abundant in Adama city these industries process heating demand can be completely or partially replaced using solar energy. For instance, Ah-Wan Food Complex is a food processing factory which is located in the industrially developed Adama town at Kebele 16, Wereda 2 of an industrial area which produces its process heating energy using fossil fuel. There are also other factories under its parent company, Ah-Wan Industry Group, which are; PP mat, PP bag, and plastic factories. The factory engages in the milling of wheat flour and converting to value-added products like Pasta and Macaroni, a fraction of the milled flour for in house consumption and excess for the local market. The pasta and macaroni products are being produced using pasta production equipment where the pasta drying section is the most important part of the production.

This thesis focuses on studying the performance of a linear Fresnel solar collector with sensible thermal energy storage in producing process heat under Adama weather condition. The study is based on a finite difference method by developing a python program and using process heat requirement of Ah-Wan Food Complex as a representative industry. This code can be easily adapted for other industries process heat generation requirement.

The linear Fresnel collector, which is concentrating type is the main component of the system which convert the solar energy in to heat. The collector has two main subcomponents, which are primary collector and a receiver tube through which a heat transfer fluid flows. As solar energy is intermittent in nature, a concrete heat storage device is also integrated, which accumulates heat when it is surplus and supply it if there is insufficient solar radiation for short period of time. In addition, the storage device reduces the influence of relatively unstable solar energy heat source and increases the stability of the system.

1.2 Statement of the Problem

It is well known that a considerable percent of industrial process energy requirement is in the form of heat. Currently, most of industries in Ethiopia are using electricity or fossil fuels to meet their heat energy demand. However, this has a negative economic impact for the industries as the price of electricity and fossil fuels is increasing each year and the government of Ethiopia have already stopped fossil fuel subsidiary.

There are many industries in Adama, one of industrial city in Ethiopia, among which Ah-Wan Food Complex is a food processing industry with large amount of process heating energy need. The current heat generation section of the company uses a conventional boiler to heat a pressurized water to a temperature of 140^{o}C that is used to control the temperature and humidity of a pasta drying machine. The company consumes around 740,918 liters of diesel fuel per year, costing it approximately 12 million of Birr only for pasta drying process. This is a substantial cost factor for the industry, affecting its profitability.

In this thesis a performance of solar heating system based on a linear Fresnel collector as an alternative source of energy for industrial process heat generation is studied. The system is designed to meet the partial energy demand of Ah-Wan Food Complex and it can be easily adapted for other industries. Even though a lot of researches have been done based on linear Fresnel solar heating systems most of them focuses in optical and thermal characterization of the system. As it is evident that the performance of solar heating system is mainly dependent on the geographical location and environmental variables, a diurnal performance analysis based on the location of the factories is essential. In addition, integration of a storage system can increase the performance and feasibility of the system as solar energy is intermittent in nature.

1.3 Objective of the Study

1.3.1 General Objective

The general objective of this thesis is to study the performance of linear Fresnel collector with sensible thermal energy storage constituted of concrete for industrial process heat generation based on thermal energy demand of Ah-Wan Food Complex pasta drying process.

1.3.2 Specific Objectives

The specific objectives of the study are

- To conduct optical and transient thermal performance modeling of the linear Fresnel collector.
- To carry out transient thermal performance evaluation of concrete thermal energy storage.
- To use the model for design a linear Fresnel solar collector for process heat generation in Adama weather condition.
- Estimate monthly performance of the linear Fresnel solar collector.
- Estimation of linear Fresnel collector size that can meet the energy demand of AH-Wan Food Complex throughout the day.

1.4 Significance of the Study

The industry under study (Ah-wan food complex) uses fossil fuel as a primary energy source for process heating. This results in a higher amount of energy cost for the factory, which is agitated by the rising of the cost of fossil fuels. If implemented in the industry, the system will minimize the cost and the environmental impact related to fossil fuels. Along that as many industries in Ethiopia are mainly dependence on fossil fuels the study will show a way for harnessing solar energy as a renewable source.

The linear Fresnel collector has many advantages for use in the industry relative to other concentrating systems including high ground usage, lower investment cost, low operation and maintenance cost, easy on cleaning of the mirrors and low wind load.

1.5 Scope and Limitations

1.5.1 Scope of the Study

This study mainly focuses on the theoretical performance analysis of a linear Fresnel solar collector that is designed to cover daily thermal energy consumption of Ah-Wan Food Complex. The study also includes the analysis of concrete thermal energy storage integrated to the linear Fresnel collector.

1.5.2 Limitation of the study

The study focuses on the study of the thermal and optical performance analysis of the main components of system. It doesn't include the design and analysis of tracking mechanisms, the mechanical or structural systems, piping and fittings, pumps and heat exchangers.

CHAPTER TWO

LITRATURE REVIEW

2.1 Solar Heat for Industrial Process

This section covers the application aspect of concentrating collectors specifically in the industrial sector which consumes a large proportion of the total power consumed. In many countries, oil products are used as an energy source for their industries. For example, according to U.S. Energy Information Administration (EIA) (2017), the share of oil products consumed by the industrial sector in Ethiopia is approximately 24.4%, even though there is no data for how much of it is for process heat generation. From long term experiences, the temperature ranges for most industrial application is 80°C-250°C and about 45% of the process heat is consumed in low and medium heat applications (Kalagirou, 2009). Table 2.1 shows a list of industries where there is a possibility of energy delivery through solar systems.

Table 2.1: Industrial processes and working temperature range (Kalagirou, 2009).

Industry	**Process**	**Temperature (°C)**
Dairy	Pressurization, Concentrates	60–80
	Drying , Sterilization	100–180
Tinned food	Sterilization	110–120
	Pasteurization, Cooking	60–90
Textile	Bleaching, dyeing	60–90
	Drying, degreasing, Fixing	100–180
Paper	Cooking, drying	60–80
	Bleaching	130–150
Chemical	Soaps	200–260
	Synthetic rubber	150–200
Plastics	Distillation, Preparation	120–150
	Separation	200–220
Flours and by-products	Sterilization	60–80

From Table 2.1, it can be inferred that a significant portion of low and medium temperature heat is required in food, beverages, paper, textile, and chemical sectors. Solar thermal systems for low heat (less than 140°C) basically consist of flat plate collectors, with or without an evacuated tube, which can supply energy at temperatures around 120°C. This technology has a major advantage since it is relatively mature and readily available.

However, as the temperature increases, non-concentrating collectors becomes inefficient and in order to supply medium heat (temperature range of 120°C-400°C) concentrating solar collectors are best suited because of high concentration ratio and efficiency. Concentrating collectors have been used for generating electricity for decades and smaller version of similar design can be employed to provide process heat with a capacity of 10 kW_{th} to 2 MW_{th} (Kalagirou, 2009).

2.2 Concentrating Solar Collectors

Concentrating solar thermal collectors are the devices which use a concentrator in order to concentrate the incident direct beam irradiation in the absorber area. So, high-temperature levels can be achieved because the heat flux values are high and so the thermal losses are restricted due to the small absorbing area. Solar concentrating technologies are separated into linear and point focus technologies. The linear technologies are the parabolic trough collector (PTC) and the linear Fresnel collector (LFC), while the point focus are the solar dish concentrators and the solar towers.

The most usual solar concentrating systems are the linear because the majority of the worldwide projects are based on them. The linear concentrating systems consist of a linear concentrator and a linear absorber. The concentrator has a parabolic shape or a segmented parabolic shape, while the absorber is located to the focal line (or very close to it). PTC is the most mature solar concentrating technology, while LFC is rapidly evolving technology which is being well-established with higher potential for improvement. The advantage of the PTC is the high efficiency and maturity, while the advantage of the LFC is the low investment cost and the decreased mechanical difficulties during the operation.

Figure 2.1: Linear concentrating solar technologies; a) Parabolic trough collector b) Linear Fresnel reflector (Lillo et al., 2017)

2.3 Fresnel Solar Collector

In this kind of collector, due to high concentration, very high temperatures of more than 400°C can be achieved. As the sun moves over the day and over the year concentrating collectors continually track the sun. The functioning principle of a linear Fresnel collector is similar to parabolic trough collector (PTC) but instead of using a parabolic reflector, flat or slightly curved mirror strips are used to achieve desired aperture area and approximate the parabolic profile. A heat transfer fluid (pressurized water, steam or thermal oil) circulates through the absorber and provides thermal energy to the process. The receiver is a fixed one unlike parabolic trough and thus made up of fewer moving parts which eliminates the need for strengthening materials. The whole idea of LFC is to provide cheaper alternative to PTC.

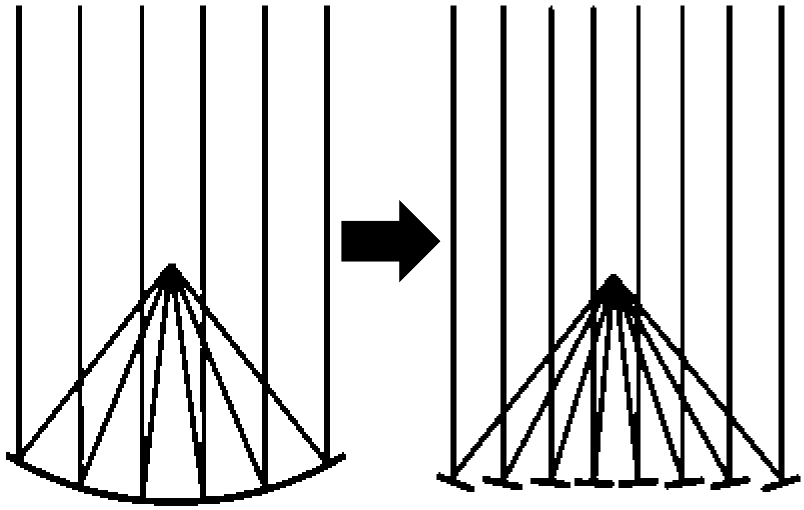

Figure 2.2: Working principle of linear Fresnel collectors (Gunther, 2017)

2.3.1 The Convectional LFC Design

Linear Fresnel collector is a solar concentrating technology with concentration ratio in the range of 10–50. The LFC has segmented primary reflectors which are placed close to the ground. This design makes the mechanical difficulties due to wind loads to be low and also the land utilization is low with this concentrating technology (Baharoon et al., 2013).

The receiver of the LFC does not move and it is located some meters over the ground. It is useful to state that the LFC has a lightweight supporting system which makes the collector cost to be relatively low. The receiver of the LFC has usually evacuated tube collector coupled to a secondary concentrator. The secondary concentrator has a parabolic shape which is usually a compound parabolic concentrator (CPC). Another conventional design is with a trapezoidal cavity receiver with many tubes inside it. The drawback of this kind of receiver is that, due to the width of the flat window, it is difficult to evacuate which in turn decreases the system efficiency by convection losses and selective coating is difficult due to air is in contact. In addition to that, the pumping power is higher due to the number of collector tubes with smaller diameter. Figure 2.3 shows the conventional receivers of LFC, the trapezoidal design in Figure 2.3a and the design with an evacuated tube coupled to a secondary concentrator in Figure 2.3b.

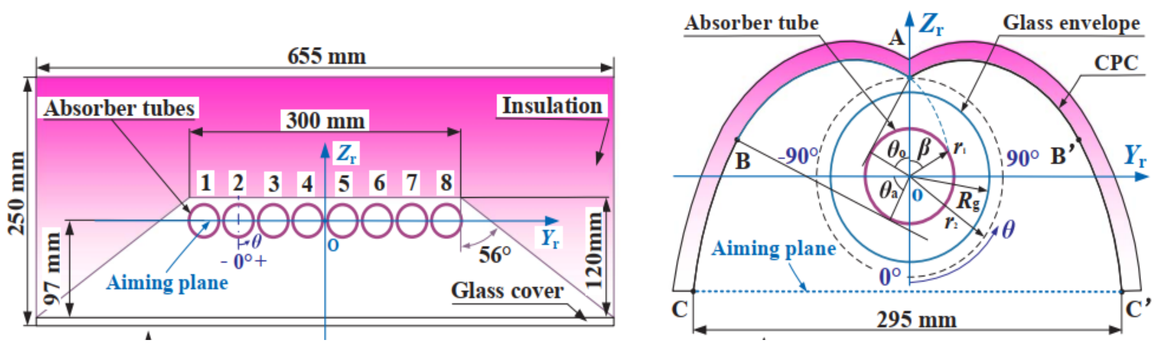

(a) (b)

Figure 2.3: Conventional receivers of LFC a) Multi-tube cavity receiver b) Single tube receiver with a secondary concentrator (Bellos and Tzivanidis, 2019)

The primary reflectors can be flat or curved. The flat reflectors are less expensive but they introduce higher optical losses. The curved mirrors have a parabolic shape and they can increase the overall optical efficiency. But the curved reflectors have problems because of the need for curved mirrors and so their cost is increased. Figure 2.4 depicts both the flat and the curved design. According to the results obtained by Benyakhlef et al., (2016), it has been suggested that a small deflection of 2 mm is the optimal design for the LFC primary mirrors.

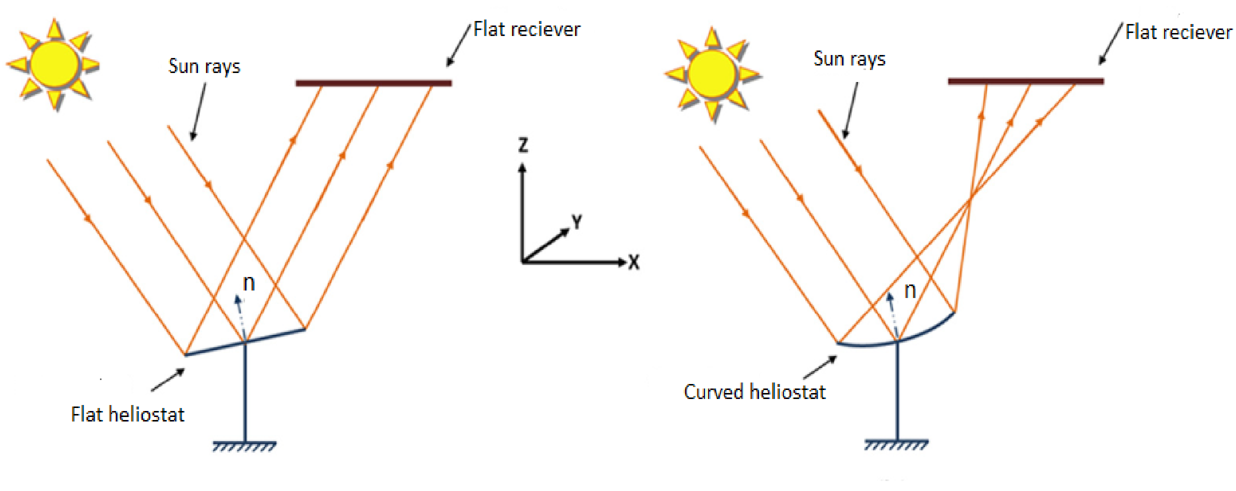

(a) (b)

Figure 2.4: Primary reflectors of an LFC a) Flat mirrors b) Curved mirrors (Benyakhlef et al., 2016)

Related to working fluids, thermal oils, water or steam can be used for various thermal applications up to 400 °C. The molten salts can be also used for power production applications which use also the molten salt for storage purposes. In the work of Bellos et al., (2018) it is reported that the operation with molten salt leads to higher thermal efficiency compared to the operation with thermal oil and also it is highlighted that the molten salt gives the possibility for operation in higher temperatures up to 600 °C.

2.3.2 Comparison of LRC with PTC

The basic competitive technology of the LFC is the PTC. Both are linear concentrating technologies which present similarities and differences. PTC and LFC usually are compared in energy and financial terms in order to determine the most suitable choice for every application. The similarities of these collectors are based on the linear character of their concentrators. So, the absorbers are linear and in many cases, the absorbers of the PTC (evacuated tubes) can be used in the LFC configurations. The concentration ratios are in the same ranges from 10 up to 50 and generally, the operating temperatures of both technologies can reach up to 400–500 °C. The working fluids are similar and they can be water, steam, thermal oils or molten salts.

However, their difference is many and important. Firstly, the primary concentrator of the LFC is segmented, while the PTC has a continuous concentrator. So, the wind loads are great in the PTC and low in the LFC (Montes et al., 2017). The tracking system of the LFC is simpler because the primary mirrors are rotated close to the ground and there are not great movements of all the systems.

Furthermore, the receiver of the PTC is moving during its operation while the LFC is constant. This situation makes simpler the connections in the LFC because they can be stable and not flexible as in the PTC. So, the risks for working fluid leakage are lower something that reduces the safety measures that have to be taken. All these facts make the LFC be a low-cost technology compared to the PTC. Moreover, the design with the segmented mirrors in the LFC gives the possibility of increasing the concentration ratio without great land utilization (Wendelin et al., 2014).

In the efficiency comparison, the PTC presents higher thermal efficiency performance than the LFC because of the important optical losses of the LFC. The segmented primary reflectors introduce important optical losses due to blocking and shading effecting among them. Also, the optical end losses of the LFC are more important than the PTC because the focal length to distance ratio is greater in the LFC, the fact that increases the shaded part of the receiver especially in low solar altitude cases (Bellos et al., 2018). Figure 2.5 shows the Incident Angle Modifiers (IAMs) for PTC and LFC. It is clear that the existence of two different factors in the LFC, transversal and longitudinal (IAM_L and IAM_T), makes the overall optical efficiency of this technology lower than the PTC which has only one factor (IAM).

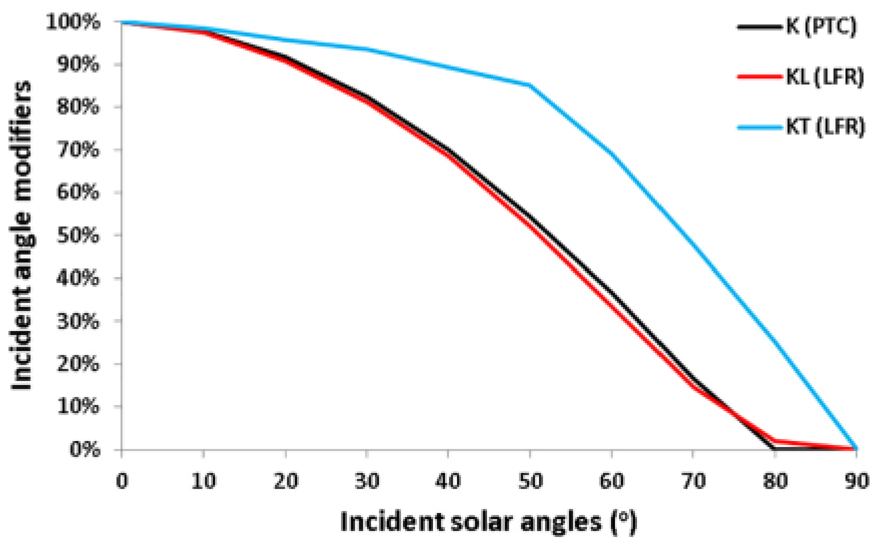

Figure 2.5: Comparison of IAM for LFC and PTC (Bellos et al., 2018)

Moreover, it is important to state that both technologies need a single axis tracking mechanism in order to follow properly the sun position. The LFC is always located with the linear axis in the South-North direction while it follows the sun in the East-West direction. This strategy is also usual in the PTC systems but the PTC can operate with other strategies such as their axis in the East-West direction and tracking the sun in the South-North direction, as well as with polar tracking systems (Sharma et al., 2013).

About the cost, the LFC seems to be a less expensive technology compared to the PTC. Generally, the cost of the LFC can be found in lower values in the literature such as Askari et al., (2017). It is also important to state that in all the comparative literature studies between LFC and PTC, the cost of the LFC is always lower to the PTC, the fact that makes clear the cost relationship between these technologies. Furthermore, the operation and maintenance costs are lower for the LFC compared to the PTC due to the smaller movement of the concentrator and the stable receiver (Huang et al., 2014).

In addition, cleaning of mirrors is one of the most important factors for performance and cost. LFC, with flat primary mirrors and the possibility to position all primary reflectors horizontally offers the advantage of an easily accessible surface that can also be cleaned with very little water consumption.

2.4 Related Studies on LFC

Qiu et al., (2014), developed a model for performance analysis of LFC with receiver comprising evacuated tube and compound parabolic reflector. The heat transfer fluid used in the model was molten salt. First, optical efficiency was obtained through Monte Carlo ray tracing code and was then coupled with finite volume method to evaluate thermal performance. The peak optical efficiency was found to be 65% and collector efficiencies for all conditions were more than 46%. The flux and temperature distribution on absorber had similar profile.

Beltagy et al., (2016) presented a theoretical and experimental study of a prototype using Fresnel solar collector system. The theoretical model used to determine various essential parameters design of the set up that are easily compared to measured data. It has been shown that thermal power production and daily efficiency are well predicted as compared to measurements. For a 250 kW installed thermal prototype, a thermal daily efficiency over 40% was measured.

Reddy and Kumar, (2014), performed a two-dimensional numerical analysis of convective and radiation losses in an inverted trapezoidal cavity receiver with multiple tubes and glass shield. The study was done by varying receiver dimensions, operating temperature and ambient conditions. In the optimum design proposed in the research, convective and radiative heat losses were 12.76% and 54% lower, respectively. Furthermore, radiation losses from glass shield were found to be most significant compared to other losses for all geometries considered in the study.

Sen et al., (2013), studied performance analysis of small scale LFC with two-tube trapezoidal cavity receiver. The collector was equipped with four bar link mechanism for single axis tracking and orientation was along North-South axis. The collector could produce 2.4 kg\h and 6.3 kg\h steam at 1.5 bar with reflector area of 5 m^2 and 13 m^2, respectively.

In another study a one dimensional heat loss model was developed by Pino et al., (2013), for a LFC with secondary reflector and evacuated tube receiver. The maximum output temperature was set to be 170°C and 13 m^3/h flowrate. This model was compared with experimental results and the difference between calculated and measured output temperature and heat absorbed by receiver was found to be below 1% and 7%, respectively. Along with this, during the experiment, the average efficiency of the receiver was 72%.

Ghodbane et al., (2019), perform a transient numerical one dimensional simulation on a linear Fresnel solar reflector directed to produce superheated water steam for the power plants, in order to determine its efficiencies (optical and thermal), where the heat transfer fluid mass flow inside the copper absorber tube is 0.045 kg/s. The optical efficiency of the LFC solar receiver has reached 63.7% where the thermal efficiency has reached 47.5%, while the pressure drop within the absorber pipe has reached 2.0 bars. As for superheated steam temperatures variations, it ranged between 233.35 and 263.75 ^{o}C, with water steam inlet temperature when entering the absorber tube is equal to 140 ^{o}C.

A detailed study on effect of radiation absorption by secondary reflector on receiver heat loss through thermal resistance model was done by Hofer et al., (2015). Three types of receiver configurations were considered, absorber with non-evacuated glass envelope, evacuated tube absorber and absorber tube with flat glass shield. The analysis was done for temperature range 100 to 550°C where 100-250°C called small-scale, and 250-550°C as large-scale. The heat losses as well as secondary reflector surface temperatures were least for evacuated tube receiver. Also, for small-scale applications, it was suggested to use receiver with glass shield because of easier construction and performance similar to non-evacuated receiver.

Two different methods were presented by Hemisath et al., (2013), to calculate the heat loss and temperature distribution of a receiver. First ray tracing combined with CFD was used. The thermal resistance model gave similar results when compared with CFD model, however, the advantage of latter was detailed representation of convection and temperature distribution but was relatively time consuming. It was concluded that for absorber temperature close to 350°C and above, the radiation absorbed by secondary reflector should be taken into consideration.

Foristall, (2008), had performed a detailed thermal analysis of an evacuated tube. He uses both one and two-dimensional thermal analysis. The results were then compared with the ones obtained from laboratory tests and good agreement was seen between theoretical and experimental surface temperatures.

In another study, Xu et al., (2015), developed a thermal resistance model to calculate thermal losses and useful energy gain in a non-evacuated tube receiver with secondary reflector and glass shield. The results obtained from thermal analysis were later used to estimate performance of an LF for direct steam generation.

A small sized LF was studied by Mokhtar et al., (2016). The collector, located in Blinda (Algeria), was made up of reflective mirror strips and trapezoidal cavity receiver and was used for heating tap water. The study was conducted both theoretically and experimentally. The theoretical model was based on energy balance and finite difference method. Results from both numerical and experimental analysis showed good agreement and thermal efficiency of collector was slightly above 29%.

Qiu et al., (2015), have proposed a similar study for an LFC with a trapezoidal cavity receiver, showing that the radiation loss is the dominant mode and contributes more than 80% to the total heat loss from the tubes. In addition, they found that the temperature profiles on the tubes follow the no uniform solar fluxes and that the heat loss increases with the steam temperature but varies slightly with direct normal irradiance.

A model for optical analysis of a solar azimuth tracking LFC was presented by Huang et al., (2014). The results obtained from analytical model were compared with ray tracing software SolTrace. According to the model the total efficiency of the Linear Fresnel Collector is 61% and it is greater than parabolic trough collector which operate at similar condition. In addition to this, it was observed that height of receiver affects shading and blocking among mirror rows, as height was increased, shading and blocking also went up. Also, width of receiver influenced heat loss significantly.

A design method was developed by He et al., (2012), to calculate efficiency of mirror elements through ray tracing and geometrical study. Simulations were performed by varying mirror width and receiver height using an LFC with eight mirror rows. It was found that mirrors closer to the central line of the collector had higher efficiency than outer rows at normal incidence. Furthermore, in the morning rows on the East side performed better than Western rows, however, the reverse was observed for the times after solar noon, that is, West side efficiency was higher than East side during second half of the day.

An analytical approach called First OPTIC was developed by Zhu (2013). The model was basically a batch of MATLAB code. The results were validated by comparing with previously verified ray tracing program SolTrace. The study focused on calculation of incidence angle modifier (IAM) and suggested that dividing IAM into longitudinal and transversal can provide results with reasonable accuracy.

Bellos et al., (2018), has developed analytical expressions for the Incident Angle Modifiers of a Linear Fresnel reflector for the longitudinal and the transversal directions. Simple and accurate formula for all the possible solar angles ranges is created for flat mirrors. The developed equations are tested with literature data from other studies and from commercial collectors. It is found that the developed equations lead to accurate results with mean deviations up to 5%. Moreover, the trends of the Incident Angle Modifier curves are the same between the model and the literature data. It is suggested that, the developed analytical expressions can be used for the quick calculation of the optical performance of a Linear Fresnel reflector, as well as they can be used for the geometry optimization of the collector.

2.5 Worldwide Installed Projects Based on LFC

In addition to theoretical and experimental studies, projects related to process heat generation through linear Fresnel collectors have been done. The projects can be small scale experimental setups and full-sized industrial installation setups. One of the largest experimental installations is at Engineering School of Seville, Spain where a linear Fresnel collector is constructed on the roof-top which generates steam and produces 174kW_{th} supplied to a double effect lithium-bromide water absorption chiller (Pino et al., 2013). The solar steam system is also assisted by an auxiliary gas boiler. The project's target is to analyze the performance of the collector and suggest possible improvements in design in order to come up with a set of guidelines for future projects. According to the experiments conducted nominal temperature output was 174°C with 72% average absorber efficiency.

Figure 2.6: Experimental unit installed in Seville, Spain (Pino et al., 2013)

Other previous projects based on similar LFC is a prototype installation in Freiburg, Germany where experimental analysis was done and another 132 m^2 system manufactured in Bergano, Italy, shown in which was coupled with ammonia-water absorption chiller .

In addition to experimental prototypes, an operational industrial setup is installed in South Africa at datacenter of a telecommunication company (Industrial solar). This roof top unit as shown in Figure 2.7 has a peak cooling capacity of 330 kW and used as a power source for driving a lithium bromide-water absorption chiller. Employing such a system for cooling purposes brings down both ozone depletion potential and global warming potential of the refrigerant to naught. The total collector area was 484 m^2 and made up of 22 LFC modules (11 mirror rows in each module). Tracking is done through a computer code in which GPS coordinates, date, time and mirror inclination are control inputs. The receiver is a combination of an evacuated tube and compound parabolic secondary reflector to prevent radiation spillage. The working fluid is water which is heated to maximum temperature of 180°C at 12 bars and return temperature is 165°C. The output of the system is controlled either by varying flowrate of the water or defocusing mirror rows in case of excess energy collection.

Figure 2.7: The roof-top installation in South Africa (Industrial solar)

In Jordan, a LF based direct steam generation unit is installed in a pharmaceutical company (Haagen et al., 2015). The collector comprises of 18 Fresnel modules of 22 m^2 each which are set up on factory's roof top. The receiver is evacuated tube place 4.5 m above ground and other components are steam drum, recirculation and feed pumps, treated water tank and steam interface to the factory. The plant capacity is 222 kW_{th} and is used to supply steam at 166°C and 6 bars as depicted in the Figure 2.8.

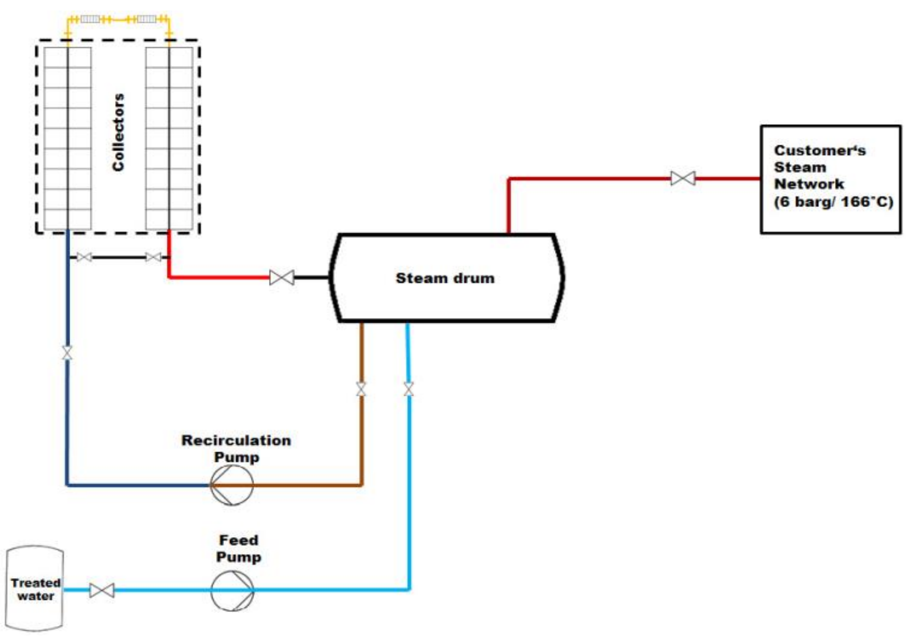

Figure 2.8: Diagram of direct-steam LFC system in Jordan (Haagen et al., 2015)

2.6 Thermal Energy Storage

Thermal energy storage (TES) systems allow the storage of heat or cold for later use. The main use of TES is in all the applications where exist a mismatch between energy production and use like in the case of renewable energies which are by nature intermittent and whose availability is further reduced by weather perturbation. Solar energy is available only during the day, and hence, its application requires an efficient thermal energy storage so that the excess heat collected during sunshine hours can be stored for later use during the night. Similar problems occur in heat recovery systems and industrial processes where the waste heat availability and utilization periods are different, requiring some thermal energy storage.

Accordingly, power stations have to be designed for capacities sufficient to fulfil the peak load. Otherwise, very efficient power distribution would be required. Better power generation management can be carried out if some of the peak load could be shifted to the off-peak load period, which can be achieved by energy storage. Hence, the successful application of load shifting depends to a large extent on the method of energy storage adopted. Generally, it is possible to divide thermal storage systems in active and passive systems. An active storage system contains a mechanically assisted component for enabling the heat transfer between the system and the heat source. Therefore, this system is characterized by forced convection heat transfer into the storage material that circulates through a heat exchanger, a solar receiver or a steam generator. In a passive storage system, the heat transfer between the system and the heat source occurs by means of natural convection or buoyancy forces (due to density gradient) without the assistance of any external devices. Active storage systems can be divided into direct and indirect systems. In the direct systems, the heat transfer fluid (HTF) is used also as storage medium, while in the indirect systems, a second medium is used for storing the heat.

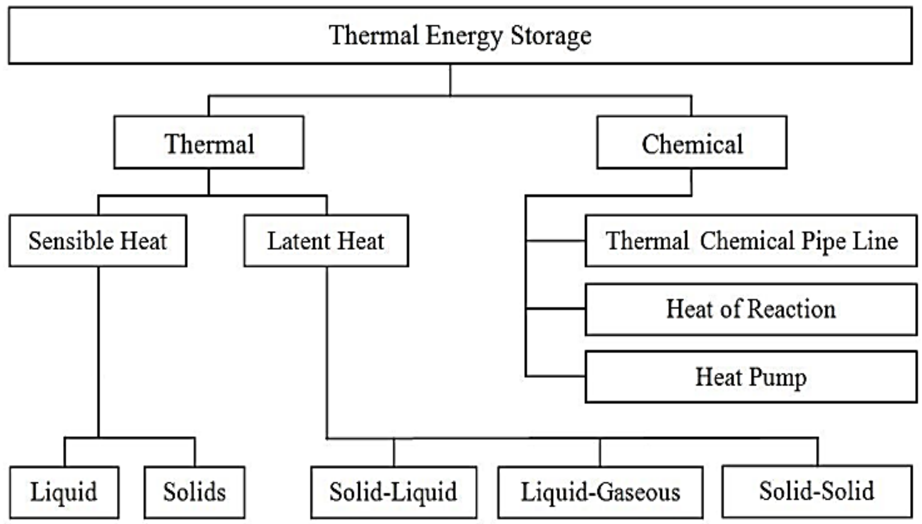

Figure 2.9: Methods of thermal energy storage (Kalaiselvam and Parameshwaran, 2014))

Latent Thermal Energy Storage

Latent heat storage is based on the heat absorption and release when a storage material undergoes a phase change. Phase change can occur in different forms: solid–solid, solid–liquid, solid–gas, and liquid–gas. Solid–liquid transitions are an economically attractive option for use in thermal energy storage systems. In fact, these transformations have comparatively smaller latent heat than liquid–gas, but involve only a small change (of about 10% or less) in volume. The storage capacity of the latent heat storage system with a solid-liquid process is given by (Farid et al., 2004):

$$Q = m\left[\int_{T_i}^{T_m} C_{p,s} dT + \lambda + \int_{T_m}^{T_f} C_{p,l} dT\right] \tag{2.1}$$

The first term of the second member is the sensible heat of the solid phase, λ represents the specific latent heat and, finally, the third term is the sensible heat of the liquid phase. In the Equation 2.1 $C_{p,s}$ and $C_{p,l}$ are specific heat of solid and liquid phase respectively and T_m is the melting temperature of the material.

Thermochemical Heat Storage

Thermochemical thermal energy storage systems use an endothermic chemical reaction, where the energy associated with a reversible reaction is required for the dissociation of the chemicals. In this case, the heat stored is given by equation:

$$Q = a_r m \Delta h_r \tag{2.2}$$

where a_r is the extent of conversion, m is the amount of storage material and Δh_r is the endothermic heat of reaction. Thermochemical materials have higher energy densities relative to PCMs and sensible storage media. Because of higher energy density, thermochemical systems can provide more compact energy storage relative to latent and sensible thermal energy storage systems. This attribute is particularly beneficial where space for the thermal energy storage is limited or valuable. Drawbacks include complexity and high cost.

Sensible Heat Storage

In sensible heat storage systems, thermal energy is stored by raising the temperature of a solid or liquid media. Sensible heat storage is by far the common method for heat storage, for example, hot water heat storage is used for domestic heating and domestic hot water in every household. The amount of energy stored is given by the relation (Kalaiselvam and Parameshwaran, 2014):

$$Q = \int_{T_i}^{T_m} mC_p dT = m\overline{C_p}\left(T_f - T_i\right) \tag{2.3}$$

where Q is the amount of heat stored in the material, m is the mass of storage material, $\overline{C_p}$ is the mean specific heat of the material evaluated in the operative temperature range and T_i and T_f are the initial and final temperature of the process, respectively. A large number of materials are available in any required temperature range therefore, the storage material is usually selected according to its heat capacity and the available space for storage. Gases have very low volumetric heat capacity and therefore are not used for sensible heat or cold storage. Table 2.2 reports some common materials used in sensible solid heat storage systems (Kalaiselvam and Parameshwaran, 2014).

Table 2.2: Typical materials used in sensible heat storage systems (Kalaiselvam and Parameshwaran, 2014)

Material	Density [kg/m^3]	Specific heat [J/kg·K]	Volumetric thermal capacity [MJ/m^3·K]
Clay	1458	879	1.28
Brick	1800	837	1.51
Sandstone	2200	712	1.57
Wood	700	2390	1.67
Concrete	2000	880	1.76
Glass	2710	837	2.27
Aluminum	2710	896	2.43
Iron	7900	452	3.57
Steel	7840	465	3.68
Gravelly earth	2050	1840	3.77
Magnetite	5177	752	3.89
Water	988	4182	4.17

2.7 Concrete Thermal Energy Storage

The TES system using concrete as the sensible heat storage media is usually implemented by embedding a tube register heat exchanger in concrete to transfer thermal energy to or from the heat transfer fluid (see Figure 2.10). The advantages of concrete thermal energy storage system include:

- Low cost of thermal storage media,
- Relatively adequate heat transfer rates into and out of concrete,
- Available in worldwide
- Uncomplicated processing (Easy on site processing) and
- Aggregates for concrete available everywhere cheaply

As a result, the application of concrete system is an attractive option regarding investment and maintenance costs in solar thermal processes.

Figure 2.10: Concrete thermal energy storage (without insulation) (Valentina et al., 2014)

Concrete materials for thermal storage are principally composed of a binder system, aggregates and a small amount of auxiliary materials. The thermo-physical properties of the solid storage materials, such as density, specific heat capacity, thermal conductivity, coefficient of thermal expansion and cycling stability as well as availability, costs and production methods are of great relevance. A high heat capacity reduces the storage volume and a high thermal conductivity increases the dynamic in the system. The coefficient of thermal expansion of the storage material and the embedded metallic heat exchanger should fit. A high cycling stability is important for a long lifetime of the storage.

With respect to these techno-economic aspects, high-temperature resistant concrete as developed for parabolic trough power plants is proposed as suitable solid storage material (Laing et al, 2008). For the high-temperature concrete, blast furnace cement is used as binder, again iron oxides are used as main aggregate, as well as flue ash and again a small amount of auxiliary materials. The material properties have been analyzed at German Aerospace Center (DLR). Shear stress analysis has proven that the contact between tubes and the solid is very good at ambient temperature as well as at elevated temperatures until 350 ^oC.

Between 1991 and 1994, two concrete storage modules were tested at the storage test facility at the Centre for Solar Energy and Hydrogen Research (ZSW), a research Centre belonging to DLR, in Stuttgart. ZSW in collaboration with other companies examined the performance, durability and cost of using solid thermal energy storage media in parabolic trough power plants. The system uses the standard HTF in the solar field, which transfers its heat through an array of pipes system, imbedded in the solid storage media. The main advantage of this approach is the low cost of the material, including a good contact between the concrete and piping, and the heat transfer rates into and out of the solid medium.

These tests took place in the Plataforma Solar de Almeria (PSA) in Southern of Spain during 2001–2006. DLR performed initial testing and found that both castable ceramic and high-temperature concrete were suitable for solid media, sensible heat storage systems. However, the high-temperature concrete is favored.

German aerospace center has performed an experiment on solid storage based on concrete (Laing et al, 2008). A 20 m^3 solid media storage test module was built in Stuttgart and is cycled by an electrically heated thermal oil loop. By end of October 2008, the solid media storage test module had accumulated four months of operation in the temperature range between 300 and 400 °C and about 50 thermal cycles with a temperature difference of 40 K.

A one-dimensional unsteady model of the heat transfer and energy storage in a solid heat storage module was developed using a modified lumped capacitance method in the work of Yongfang et al., (2014). The method is valid for large Biot numbers with the introduction of an effective heat transfer coefficient. Experiments using water as the heat transfer fluid and concrete as the storage material were used to validate the model. The model was used to analyze a cylindrical energy storage unit to study the energy storage in the storage module and optimize the design.

Rungrudee and Sukrudee, (2016), made an experiment on solid storage based on concrete material. The thermal energy storage prototype was composed of pipes embedded in a concrete storage block. The storage prototype had the dimensions of 0.5 x 0.5 x 4 m. The charging temperature was maintained at 180°C with the flow rates of 0.009, 0.0012 and 0.014 kg/s whereas the inlet temperature of the discharge was maintained at 110°C. The performance evaluation of a thermal energy storage prototype was investigated for charging/discharging process. The experiment found that the increase or decrease in storage temperature depends on the heat transfer fluid temperature, flow rates, and initial temperature. The energy efficiency of the thermal energy storage prototype at the flow rate of 0.012 kg/s was the best because it dramatically increased and gave 41% of energy efficiency in the first 45 minutes after which it continued to rise yet only gradually. Over

180 minutes of operation time, the energy efficiency at this flow rate was 53% and the exergy efficiency was 38%, respectively.

Jian et al., (2014), studied a one-dimensional unsteady model using the modified lumped capacitance method for a solid cylindrical concrete heat storage unit. A modular charging/discharging control strategy is proposed to improve utilization of the solid storage material. The control strategy of modular charging/discharging using two modules could increase the storage material utilization from 33.4% to 38%.

Bai et al., (2008), studied sensible heat storage unit with a hollow cylinder of solid media semi-analytically. The heat transfer process in the heat storage medium was solved by using an integral approximate method. The forced convective heat transfer inside the tube was coupled with the heat conduction in the heat storage media. This method enables evaluation of the performance of the storage device in transient conditions. Different heat transfer fluids such as water and air with variable thermal properties dependent of temperature are used in calculations. Concrete and cast iron are selected as heat storage materials. From the simulation results presented in this paper, the thermal conductivity, the distance between the tubes, heat transfer fluid, tube size and flow velocity are the key parameters for such heat storage unit design.

2.8 Conclusion from Literature Review and Research Gap

The previous literature review shows that using LFC for process heat generation in industries is a promising choice. The thermal and optical performance characterization of the collector is the main focus point of the studies. Adequate performance, coupled with relatively low cost makes this collect's application feasible. The collector have been applied in many applications such as electricity production, steam production, space-cooling and desalination etc. Various systems have been studied worldwide, especially in locations with relatively high solar potential. Ethiopia, as located near the equator, is a country with high solar potential, which reaches 6.5 $kWh/m^2/day$ (Samuel and getachew, 2014). Adama is relatively hotter climate city in Ethiopia; and it is a representative location for solar energy utilization. So, in this paper, a comprehensive model is developed to study the energetic performance of LFC by integrating it with a concrete thermal energy storage.

The model is based on previously discussed works, but unlike most of researches presented in literature where main focus is optical or thermal performance and lacks detailed studies about the daily performance and characterization of integrated LFCs, this research presents a diurnal analysis of the collector by integrating it with a low cost, newly emerging concrete thermal energy storage in Adama weather condition.

CHAPTER THREE

PERFORMANCE ANALYSIS OF LINEAR FRESNEL COLLECTOR

3.1 The Examined Linear Fresnel Collector

The examined linear Fresnel reflector is depicted in Figure 3.1 where the main dimensions of this collector are given. This collector has been also examined by (Haagen et al., 2015; Christian and Oliver, 2012). Main components of the system are

- Supporting structure (1)
- Primary reflectors (2)
- Receiver, consisting of secondary reflectors and absorber tubes (3)

The collector has a receiver containing an absorber with a selective absorber coating. A detailed thermal performance of the receiver is presented in the next chapter. Moreover, Table 3.1 gives data about the receiver and the overall collector system.

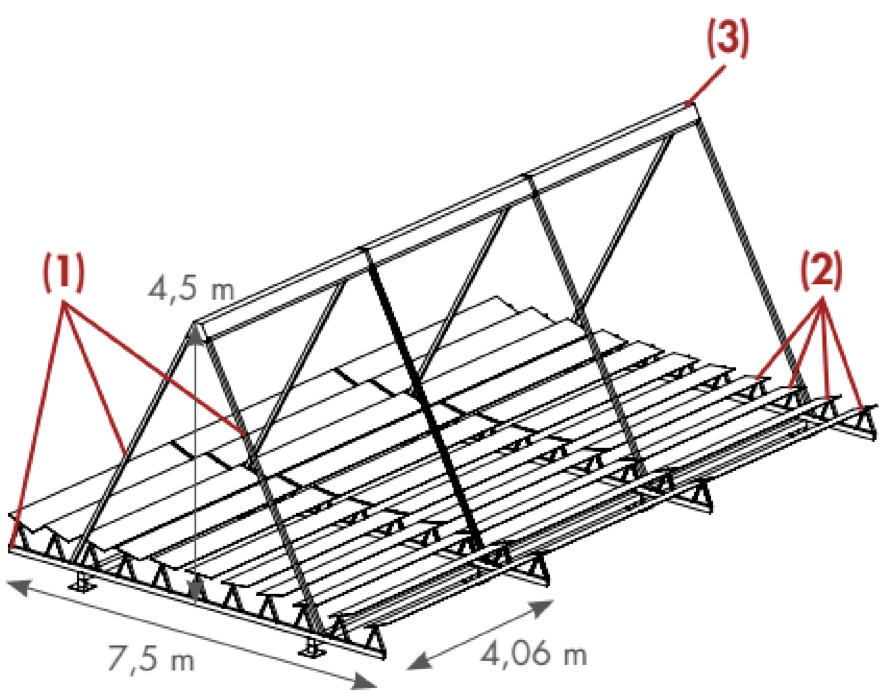

Figure 3.1: The examined linear Fresnel collector with three modules (Haagen et al., 2015)

Table 3.1: Specifications of the linear Fresnel collector.

Primary mirror geometrical specifications (Industrial Solar LF-11 Technical data sheet)	
Width	7.5 m
Parallel mirror rows	11 m
Aperture width	5.5 m
Height	~4.5 m
Aperture area per module	22 m^2
Gap between mirror rows	0.2 m
Receiver geometrical specifications (Mokhtar et al., 2019, Industrial Solar**)**	
Receiver length	4 m
Inner absorber diameter	0.066 m
Outer absorber diameter	0.070 m
Inner glass cover diameter	0.125 m
outer glass cover diameter	0.115 m
Optical specifications (Mokhtar et al., 2019, Schott Solar CSP GmBH**)**	
Primary mirror (coated glass) reflectivity	0.94
Absorber absorptance	0.95
Absorber emittance	0.09
Glass cover absorptance	0.02
Glass cover emittance	0.43
Glass envelope transmittance	0.95
Intercept factor	0.94

1. **Geometry**

The simplified two dimensional geometry of the examined LFC is given in Figure 3.2 with details. This LFC has flat primary mirrors with a width (W_o) and the distance between the mirrors (D_w). The focal distance (F) and the distance of every mirror (Fi) and the position angle (φ_i) are also important parameters of the collector.

Abbas et al., (2018) compared different secondary reflector shapes, more specifically the compound parabolic concentrator, the adaptive design concentrator and the segmented parabolic secondary concentrator (CPC). From these, CPC shows a higher efficiency for higher heat flux ranges. In this study, for possibility of operation at higher heat fluxes CPC is used as a secondary concentrator. In addition, this kind of concentrator is simple in design and construction.

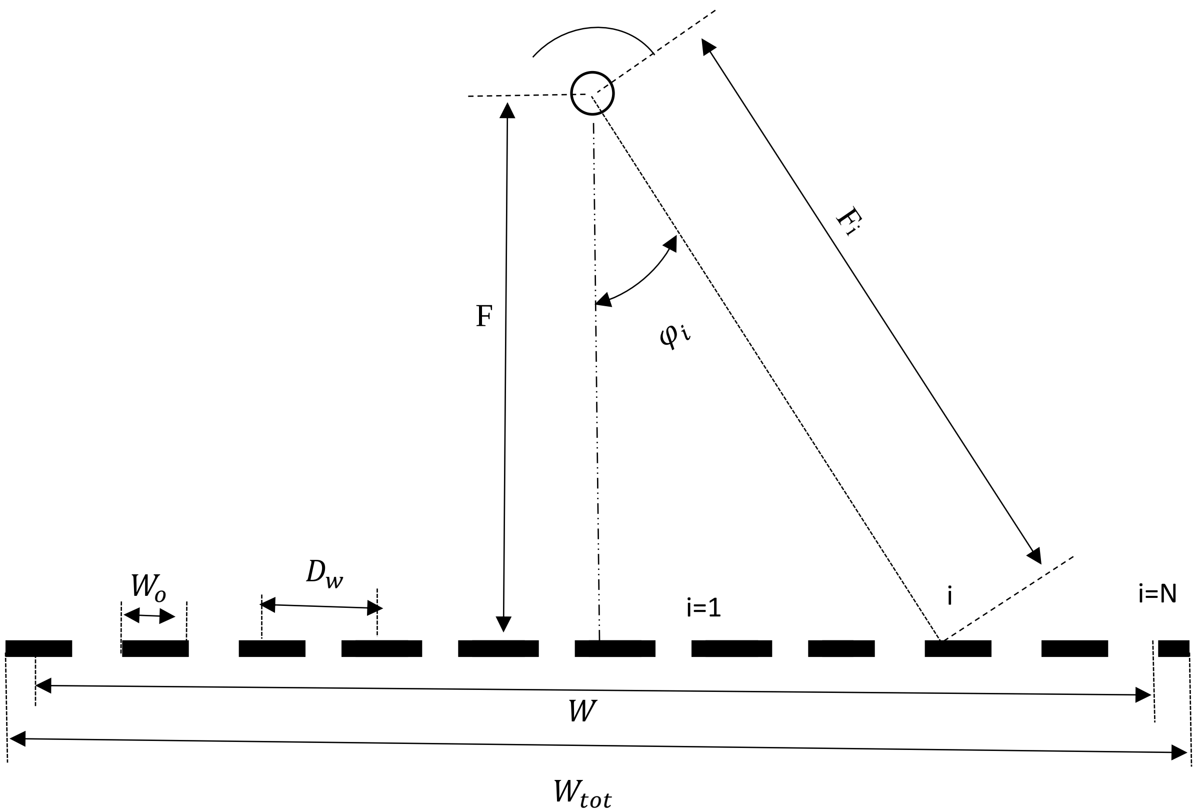

Figure 3.2: A simplified model for an LFC, Adopted from (Bellos and Christos, 2018)

The total collector width (W_{tot}) is equal to (Bellos and Christos, 2018)

$$W_{tot} = W + W_o \tag{3.1}$$

The collector width (W) is the distance between the centers of the mirrors in the right and in the left sides. Totally there are ($2N + 1$) mirrors. The parameter (W) is calculated as (Bellos and Christos, 2018).

$$W = (2N + 1)D_w \tag{3.2}$$

The location of every mirror (X_i) is calculated as

$$X_i = iD_w \tag{3.3}$$

2. **Aperture Area**

The aperture area of a reflected element is an important construction parameter of a solar radiation concentrating system, as it determines the maximum solar radiation captured. The aperture area, A_i, of each reflective element, i, is calculated as the product of its aperture width, W_i, and its length, L_i:

$$A_i = W_i . L_i \tag{3.4}$$

If the size of each mirror is the same the total aperture area is found by multiplying Equation 3.4 by n (number of mirrors).Thus the selected collector has an aperture area of 22 m^2 per module.

The distance (F_i) is calculated as:

$$F_i = \sqrt{F^2 + i^2 {D_w}^2} \tag{3.5}$$

The position angle (φ_i) of every mirror can be calculated as (Bellos and Christos, 2018):

$$\cos(\varphi_i) = \left[1 + i^2 \left(\frac{D_w}{F}\right)^2\right]^{-1/2} \tag{3.6}$$

Table 3.2: Position angle of each mirrors (symmetrical mirrors have equal angle)

Mirror number	1	2	3	4	5	6
Position angle (φ_i)	0.0	9.92	19.29	27.69	34.99	41.19

3. Concentration Ratio

The concentration ratio of a solar radiation concentrating system is another important parameter which affects the construction's efficiency. It determines the operating temperatures of the system. The concentration ratio,C is defined as the ratio of the direct solar radiation flux incident on the aperture of the reflector, F_m, to the solar radiation flux concentrated on the receiver, F_r:

$$C = \frac{F_m}{F_r} \tag{3.7}$$

However, the concentration ratio, C, can be determined without any measurement. It is equivalent to the ratio of the reflectors' effective aperture area, A_m, to the receiver illuminated aperture area, A_r.

$$C = \frac{A_m}{A_r} \tag{3.8}$$

Another possibility is to take the irradiated absorber surface area as the receiver aperture area. However, since the reflective elements are not arranged perpendicular to the incoming solar radiation, their effective aperture surface is smaller and the collected solar radiation is lower. The effective aperture area, A_i, of the i^{th} reflective elements as encountered by the approaching solar light rays in the transversal plane can be calculated by the formula:

$$A_i = W_i . cos\theta_i . L_i \tag{3.9}$$

Where (θ_i) is the solar radiation incidence angle on the i^{th} reflector.

3.2 Tracking Angle (Mirror Inclination)

LF is equipped with single axis tracking system and it changes the inclination of mirrors throughout the day. The inclination angle (ψ) depend on position of sun, height of receiver (F) and position of the mirrors relative to central axis and is found by means of Equation 3.11 and using geometries shown in Figure 3.3.

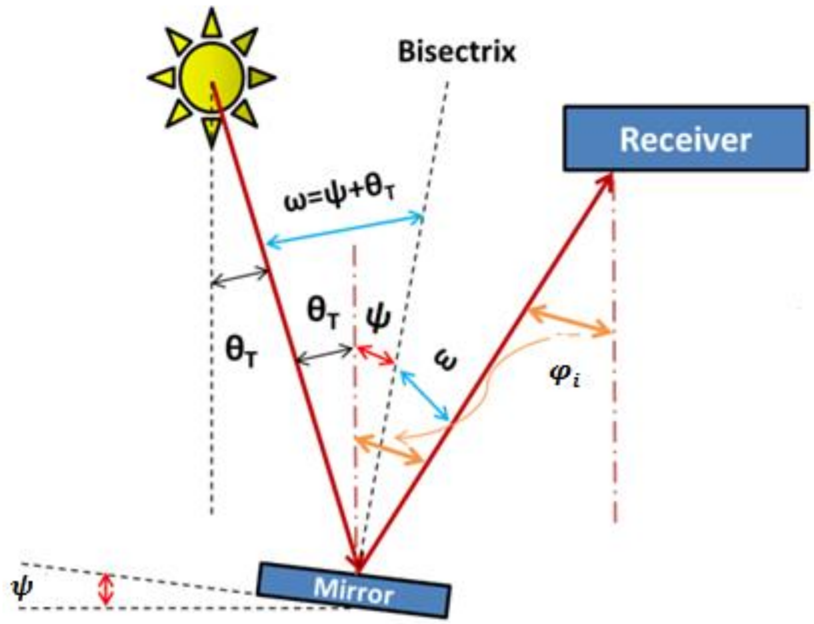

Figure 3.3: Slope of primary flat mirror in the LFC (Bellos, 2018)

In order to obey to the Snell-Descartes low (the incident angle is equal to the angle of reflection), each mirror admits its own normal surface. The tracking angle ψ_i is then defined according to Rabl (Bello and Tzivanidis, 2018), as the tilt angle: angle between the horizontal plane and the plane containing the reflective mirror:

$$\psi_i = \frac{\varphi_i - \theta_T}{2} \tag{3.11}$$

Where φ_i is the angle between the optical axis and the line joining the mirror and the receiver (the position angle of each mirrors), and θ_T is the transversal incident angle. At noon, the incident angle is close to zero, and then the tracking angle is:

$$\psi_i = \frac{\varphi_i}{2} \tag{3.12}$$

On differentiating Equation 3.11 with respect to time:

$$\frac{d\psi_i}{dt} = -\frac{1}{2}\frac{(d\theta_T)}{dt} \tag{3.13}$$

According to Equation 3.13, the rate of change of ψ_i depends solely on sun's motion. Therefore, tracking for all primary mirrors can be achieved with a single motor with constant angular velocity.

However, in practice, each primary mirror has its own tracking motor to increase tracking accuracy and ease of energy dumping.

3.3 Optical Efficiency

The main objective of the optical analysis is to determine the amount of energy from solar rays reflected from mirrors and intercepted by the receiver at any sun position. The ratio of solar energy absorbed by the receiver and solar energy that impinges on the reflectors is the optical efficiency and for a LFC, it depends on sun's position, focal length of primary mirrors, height of the absorber above the primary mirror plane, width of primary mirror strips, latitude of location, gap between the mirror strips and number of parallel mirror rows. In addition, the optical efficiency relies on many factors such as tracking error, geometrical error, and surface imperfections.

Similar to other linear concentrating collectors like PTCs, the optical performance analysis of a LFC systems can be evaluated by studying and analyzing the influence of the most important phenomena. These are shadowing by the receiver and adjacent reflectors, blocking by adjacent reflectors, reflectors' slope error, reflected solar radiation spillage on the receiver, Sun tracking errors, and material characteristics. As a consequence, the optical analysis plays a significant role in LF systems design. It is also important to know that optical analysis of a the collector is purely geometrical dependent due to the fact that the directions of sun rays and the considered phenomena (solar rays' reflection and refraction) are independent of the solar radiation values.

The optical efficiency of linear Fresnel collectors is a function of dimensions, design parameters, material properties and environmental effects. The efficiencies due to environmental effects are not considered here because they are difficult to parametrize.

$$\eta_{optical} = \eta_{cosine} \cdot \eta_{shad} \cdot \eta_{block} . \eta_{end} . \eta_{clean} \tag{3.14}$$

Where:

- η_{clean} describes the reduction of the optical efficiency due to soiling of the reflectors; it is considered to be equal to 1 as it is difficult to be parameterized and prescribed and depends on the reflectors cleaning system.
- η_{end} accounts for the energy losses due to the fact that when the incident angle of the solar radiation is different from the normal, a part of the reflected solar irradiation misses

the receiver, while at the same time another part of the receiver does not receive any solar radiation at all.

- η_{shad} and η_{block} account for shading and blocking effects that occur when Sun's elevation angle, is low, or else, Sun is near the horizon.
- η_{cosine} occur due to cosine effect

The optical efficiency, $\eta_{optical}$, can also be described using the product of the maximum optical efficiency, η_{max} and Incident Angle Modifier, IAM, as expressed by Equation 3.15. The optical efficiency at normal incidence on perfectly clean reflectors which are not shaded and the reflected solar radiation is not blocked is given by Equation 3.16 **(**Mohamed and Amr, 2016).

$$\eta_{optical} = \frac{q_{absorbed}}{A_{ap} x \bar{I}_b} = \eta_{max}.IAM \tag{3.15}$$

$$\eta_{max} = \tau.\rho.\gamma.\alpha \tag{3.16}$$

In Equation 3.15 and 3.16 $q_{absorbed}$ represents the absorbed radiation . $\bar{I}_b$ represents the beam component of solar radiation, τ, ρ, γ, and α represents the transmitivity of glass cover, reflectivity of primary mirrors, Intercept factor and absorptivity of the absorber, respectively. The intercept factor γ is defined as the fraction of the reflected radiation that is incident on the absorbing surface of the receiver.

Incidence Angle Modifier (IAM)

A linear Fresnel collector attains peak optical efficiency in case of normal incidence and there is decline in optical performance at off-normal incidence due to dependence of optical properties of the collector on direction of incident sun rays. So IAM is used to correct the collector's performance at normal incidence to off normal directions (Bello and Tzivanidis, 2018). In case of LFC, biaxial IAM is required, that is, one for transversal incidence angle (θ_T) and other for longitudinal (θ_L) as shown in Figure 3.4.

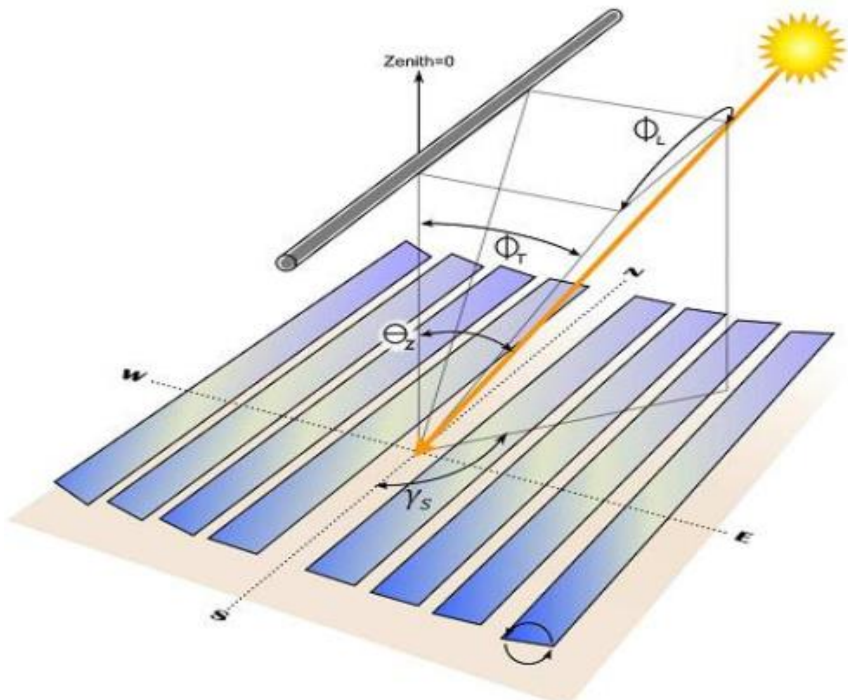

Figure 3.4: Transversal and longitudinal incidence angle for LFC (Wagner, 2012)

The relation between θ_T, solar azimuth (γs) and solar altitude (α_s) for North-South orientation is shown in Equation 3.17 and for θ_L by Equation 3.18 .

$$\tan(\theta_T) = sin(\gamma_s).\tan(\theta_Z) \tag{3.17}$$

$$\tan(\theta_L) = \cos(\gamma_s)\,.\tan(\theta_Z) \tag{3.18}$$

Zenith angle (θ_Z), can be found from the relation given by (Duffie and Beckman, 2013):

$$\cos(\theta_Z) = \cos(\varphi)\,.\cos(\delta).\cos(\omega) + \sin(\varphi)\,.\sin(\delta) \tag{3.19}$$

Here, φ represents the longitude of the location, ω the hour angle and δ the declination angle. The IAM is determined by taking product of two components, (Mohamed and Amir, 2016) as shown in Equation 3.20.

$$IAM(\theta_L, \theta_T) = IAM(\theta_L, 0) * IAM(0, \theta_T) \tag{3.20}$$

IAM is a complex parameter and its calculation usually needs a ray tracing software like TracePro, Tonatiue or Soltrace. It is computationally intensive process as the method relies on generating a large number of vectors (rays) and calculating their interaction with optical materials. However the model developed by Bellos and Christos (2018) shows that the IAM can be calculated analytically with reasonable accuracy. The model is developed for flat mirrors which neglects the existence of curvature in primary mirror field. The analytical model accounts the following optical losses:

- Cosine losses
- Shading losses
- Blocking losses
- End losses

The transversal IAM can be expressed as (Bellos and Christos, 2018):

$$IAM_T(\theta_T) = \cos\left(\frac{\theta_T}{2}\right) - \frac{\frac{W}{4}}{F+\sqrt{F^2+\left(\frac{W}{4}\right)^2}}\sin\left(\frac{\theta_T}{2}\right) \quad \text{for } \theta_T < \theta_{T,crit} \tag{3.21}$$

$$IAM_T(\theta_T) = \cos\left(\frac{\theta_T}{2}\right) - \frac{\frac{W}{4}}{F+\sqrt{F^2+\left(\frac{W}{4}\right)^2}}\sin\left(\frac{\theta_T}{2}\right)\left[\frac{D_W}{W_0}.\frac{\cos(\theta_T)}{\cos\left(\frac{\theta_T+\varphi_m}{2}\right)}\right] \quad \text{for } \theta_T \geq \theta_{T,crit}..$$

....(3.22)

The expression in Equation 3.22 utilizes only primary perimeters of the collector geometry (W_o, D_w, φ_m, w and F) and the transversal solar angle (θ_T). The mean value of the angle (φ_m) angle can be calculated as follows:

$$\varphi_m = 2.\arctan\left(\frac{\frac{W}{4}}{F+\sqrt{F^2+\left(\frac{W}{4}\right)^2}}\right) \tag{3.23}$$

Where;

$$\theta_T, crit = 94.46 - 2.519.\lambda - 55.71\lambda^2 - 0.48\varphi_m + 1.77\frac{\varphi_m}{1000} + 1.15.\lambda.\varphi_m \tag{3.24}$$

The parameter (λ) is the ratio of the mirror width to the distance between the mirrors (λ=W_o/D_w). The angles ($\theta_T, crit$) and (φ_m) are in degrees. Moreover, this equation is valid for the following conditions:

$20^o < \varphi_m < 70^o$ and

$0.5 < \lambda < 0.95$

The longitudinal IAM can be expressed in the following expression (Bellos and Christos, 2018):

$$IAM_T(\,\theta_L) = \cos(\theta_L) - \frac{F}{L}.\sqrt{1 + \left(\frac{W}{4F}\right)^2}\,.\sin(\theta_L) \qquad (3.25)$$

Equation through 3.21 to 3.25 can be used to calculate the daily IAM for LFCs. Figure 3.5 shows variation of IAM with incident angles and Figure 3.6 shows the hourly IAM variation of January 17 for Adama in north-south orientation (East-West tracking).

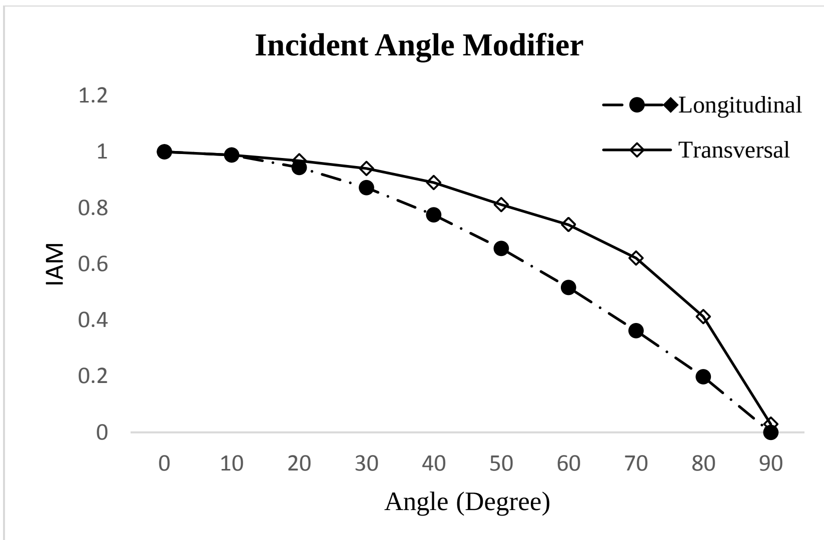

Figure 3.5: Incident Angle Modifier vs. Angle of Incidence

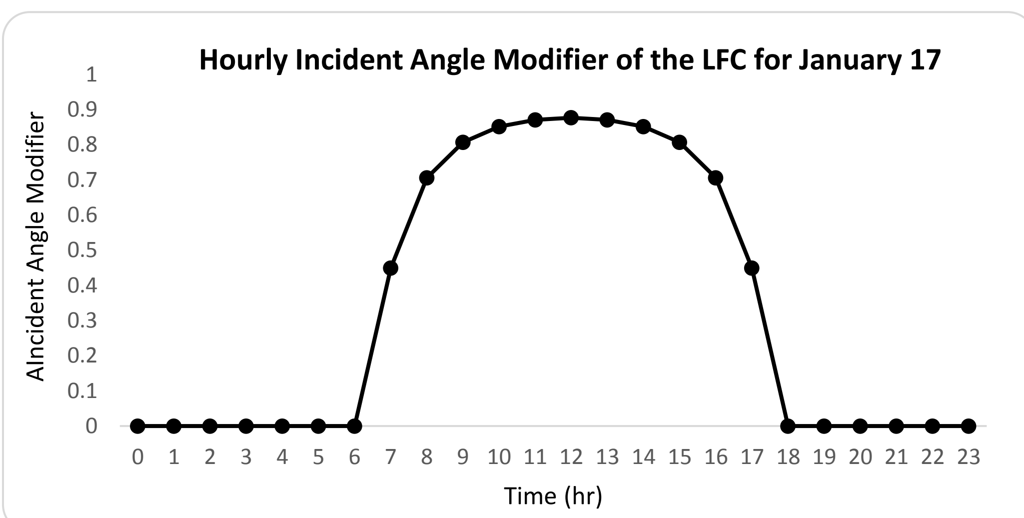

Figure 3.6: Hourly IAM of the LFC in January 17 for East-West tracking

To simplify the analysis a daily mean Incident Angle Modifier is used in this paper.

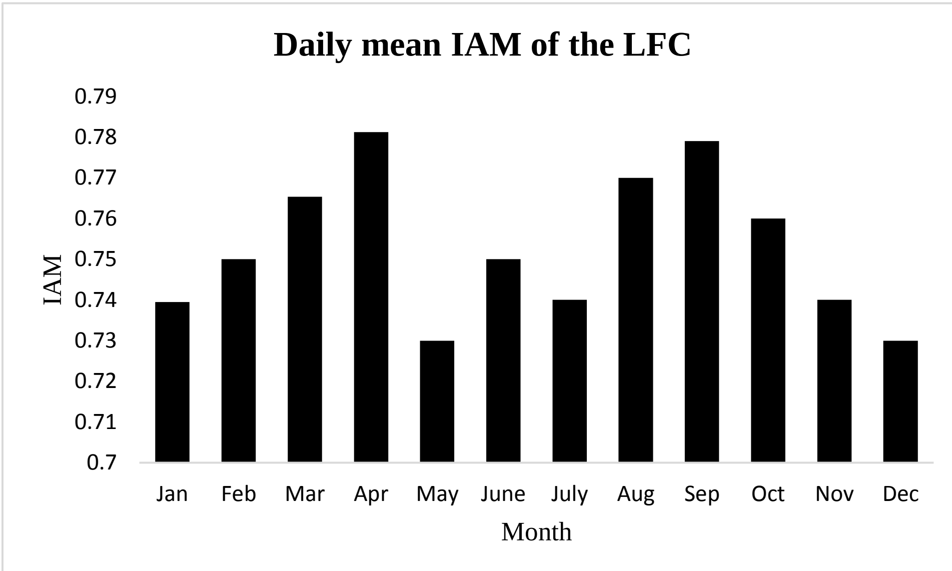

Figure 3.7: Daily mean Incident Angle Modifier for Adama in North-South orientation

The absorbed solar energy, which is reaching the absorber can be calculated by **(**Mohamed and Amr, 2016).

$$q_{absorbed} = \eta_{opt} x A_{ap} x \bar{I}_b = [\alpha . \rho_m . \tau . \gamma .\ IAM_{mean}] A_{ap} . \bar{I}_b \quad (3.26)$$

Where: $\bar{I}_b$ is the beam component of global radiation.

Concentrated solar power technologies utilize only the beam component of the solar radiations and beam radiation reaches the earth surface without any hindrances (absorption and reflection) from the atmosphere. The estimation of solar radiation is presented in Section 3.8 based on Adama weather condition.

3.4 Thermal Performance of the LFC

Useful energy gain by the heat transfer fluid in the absorber tube section of the LFC is given by:

$$q_u = \dot{m}_{HTF} C_{HTF} (T_{HTF,o} - T_{HTF,i}) \quad (3.27)$$

Where:

- q_u represents useful heat generated
- $\dot{m}_{HTF}$ the mass flow rate of HTF
- C_{HTF} the specific heat capacity of HTF
- $T_{HTF,i}$ and $T_{HTF,o}$ the inlet and outlet temperature from the LFC

The HTF is assumed to be in a single phase region in its working temperature range. So only sensible heating should be considered in useful energy calculation.

The instantaneous thermal efficiency of the LFC, η_{th}, is calculated based on the heat gain, solar intensity and aperture area of the collector and it given as

$$\eta_{th} = \frac{q_u}{A_{ap}\bar{I}_b} \tag{3.28}$$

The heat gain of the circulating water in the pasta drying line, q_{line}, can be given by:

$$q_{line} = \dot{m}_w c_w (T_{w,o} - T_{w,i}) \tag{3.29}$$

Where:

- $\dot{m}_w$ represents the mass flow rate of water
- c_w the specific heat capacity of the water
- $T_{w,i}$ and $T_{w,o}$ the inlet and outlet temperature of the water

3.5 Description of Industrial Process and Requirements

The drying stage of the pasta production in Ah-Wan Food Complex requires a large amount of thermal energy necessary to dry the product. Superheated water at 140 °C and 4.5 bar (liquid state) is used to control temperature and humidity conditions of the pasta drying tunnel. The drying tunnel consists of a series of drying sections namely: pre-dryer, dryer, stabilizer and humidifier each of them with different temperature need. The drying process for each production line is managed by a Programmable Logic Controller (PLC) which, collecting data from sensors to manage climate regulation within the different areas (sections) of the dryer.

The pasta making process needs, besides high-temperature thermal energy required for drying the product, even cooling energy. The product must be cooled from drying out and the heat produced during the extrusion of product (the extrusion pressure is about 100 bar) must be dissipated. Both these sections are equipped with a cooling tower and a vapor compression refrigeration chiller. However these energy needs are out of the scope of this thesis.

3.5.1 Thermal Energy Consumption

As stated before, the thermal loads are due to the heat required of the pasta dryers that employ 140 °C and 4.5 bar superheated water. The temperature of superheated water at the exit of the dryers is about 120 °C with a mass flow of about 11 kg/s. The superheated water is also used to produce hot water (45 °C) necessary to obtain a good mixture in kneaders. The water is heated using a conventional water super heater which uses fuel as a primary energy source.

The currently installed heat generation section has a boiler with 1760 kW rated thermal output and 1933 kW rated heat input. Based on this, the boiler has an efficiency of 0.91 neglecting the decrease in efficiency with time. The Nameplate of the boiler can be found in APPENDIX (ANNEX B). From The factory, heating load was found by investigating the annual diesel fuel consumption, the number of working days, the boiler efficiency and the net heating value of the diesel fuel.

Based on the company's long term experience a 2 weeks of maintenance schedule with no production per year is considered. Therefore there are 351 working days per year. The net heating value of diesel fuel is taken as 38 MJ/lit. From Table 3.3 we can infer that the industry consumes about 740,918 liters of diesel fuel per year which corresponds to 845 kW of power. The monthly fuel consumption of the industry shows that there is a quite flat annual thermal load profiles and differences occur mainly due to electricity supply fluctuation in the city which forces the factory to stop production.

Table 3.3: Monthly fuel consumption of the factory (Ah-Wan Food Complex)

Month	**Fuel consumption (Liter)**	
	July 2017-June 2018	**July 2018-June 2019**
January	58806	37647
February	85436	51609
March	69303	48920
April	70634	54403
May	69200	67480
June	82909	68952
July	76864	65181
August	62310	61241
September	73552	67317
October	65840	63086
November	32940	54787
December	33950	59470
Total	**781744**	**700093**

3.5.2 Integration Concepts

The most important criteria in industrial process heating system design is to distinguish the level at which solar heat is integrated. As described by Bastian (2016), it can be distinguished between supply level and process level. Many industries have a central boiler house for heat generation and distribution. Mainly natural gas or fuel oil is used to generate steam or pressurized water, which is transferred via a central distribution system to the different decentralized heat consuming processes. A general distinction between supply and process level seems reasonable to simplify the integration of solar heat, since generalizations regarding the required temperature levels can be done and thus conclusions regarding suitable collector technologies can be drawn (Bastian, 2016).

3.5.2.1 Process Level

The integration at process level usually comes along with lower solar set temperatures, since all process are operated below the supply temperature. However, the effort for integration of solar heat can be higher compared to supply level. In the case of Ah-wan Food Complex, the process for this integration concept can be pre-drier (41-65 °C), drier (79-86 °C), and stabilizer (68-69 °C) sections of the drier tunnel or to produce hot water (45 °C) necessary to obtain a good mixture in kneaders.

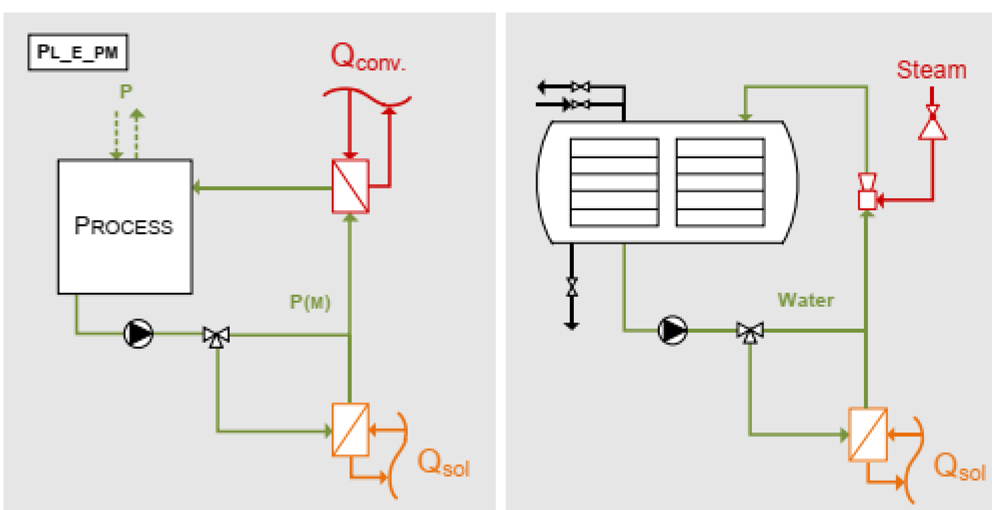

Figure 3.8: Integration concept for solar heating of product or process media with external heat exchanger at process level (Bastian, 2016)

3.5.2.2 Supply Level

Generally, the integration of solar heat at supply level is less complex compared to process level. Besides the heating of make-up water, all integration concepts come along with high set temperatures that have to be provided by the solar heating system. The minimum set temperature for a solar heating system is approximately 100 °C, and can easily exceed 200 °C, based on the respective system concept (parallel or serial integration) and the boundary conditions of the heat generation and supply system (hot water or steam circuit) Therefore, the integration on supply level should be preferred in regions with very good irradiation (Bastian, 2016).

Using concentrating collectors at locations with sufficient direct irradiation, solar steam can be generated that is fed into the existing heat supply system. Therefore, the integration concept illustrated in Figure 3.9 can be applied. In addition, concentrating collectors with pressurized water or thermal oil as heat transfer medium are used to feed a heat exchanger. The produced steam or pressurized water is fed into the process line and provided to the different heat loads within the factory.

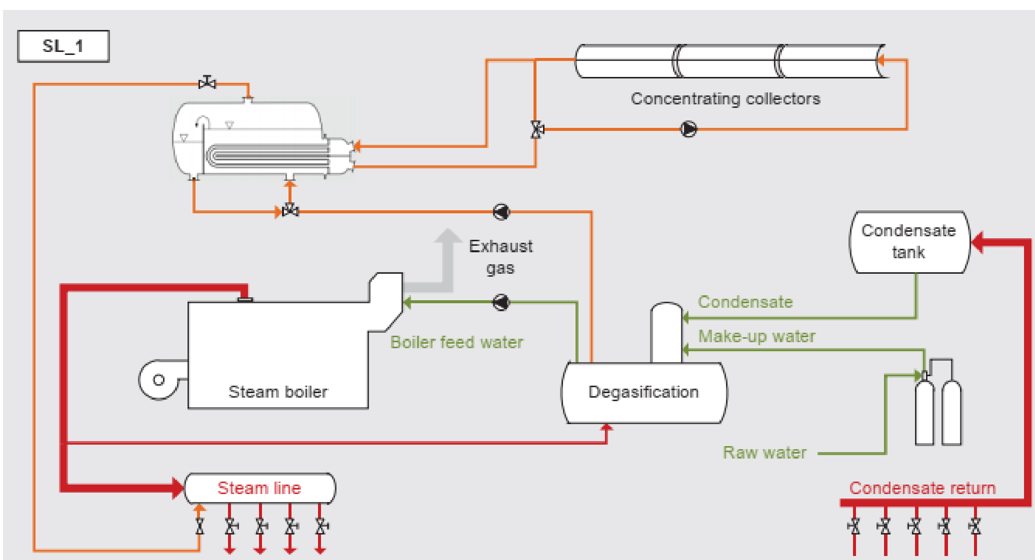

Figure 3.9: Integration concept for indirect solar steam generation at supply level (Bastian, 2016)

Even though most industries employ a steam for processes some of them may use circulating pressurized water or oil. In this study the heat transfer fluid through the process is pressurized water so a similar integration concept can be taken as in indirect steam generation with a simple modification.

3.5.3 Solar Integration for the Direct Production of Thermal Energy at Supply Level

As discussed before, the knowledge of where the solar heating system is integrated is critical. A supply level integration is chosen here due to the availability of adequate solar radiation in the factory location i.e. Adama and its simplicity in integration. It is also important to note that the control system shouldn't be compromised. Integrating in a process level can interfere in the production process which is already existed. The solar heating system is designed to cover the daily energy requirement of the factory including night time. The possibility of integrating the conventional production of thermal energy by means of a solar plant is with a concrete thermal energy storage is illustrated in Figure 3.10. The solar thermal plant can be described by the following three basic elements:

1. The pasta factory thermal plant, where the Heat Transfer Fluid (HTF) is superheated water (circulating with a Mass flow rate of 11 kg/s at 4.5 bar) which must be regularly heated from 120 °C to 140 °C;
2. A concentrating solar thermal power plant made up of a system of small-size linear Fresnel collectors which heats the HTF above 140 °C (as functions of the direct normal irradiance and the external air temperature);
3. A sensible thermal energy storage constituted of concrete

As a food production factory the industry has its own food safety standard so the HTF flowing through the solar collector and thermal energy storage is a food grade oil (Paratherm-NF) to prevent any possible toxic contamination of the superheated water passing through the heat exchanger. A shell and tube heat exchanger is used to hydraulically disconnect the solar plant from the pasta factory production lines, allowing the transfer of the thermal energy from the oil to the superheated water.

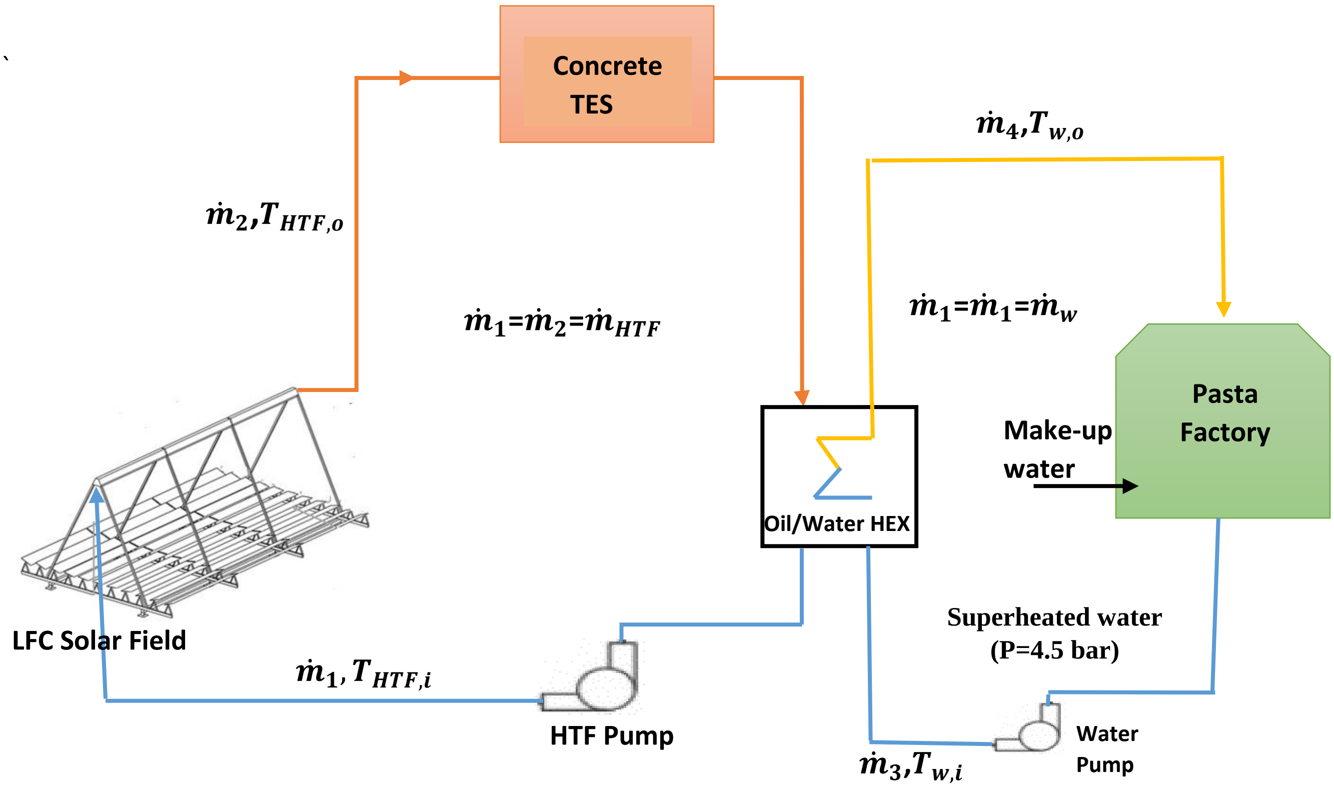

Figure 3.10: Schematic diagram of the proposed system for Ah-Wan Food Complex

The LFC solar field consists of a number of modules connected in series and parallel arrangement. A parallel arrangement of the whole solar field with three modules in series is used for analysis. Therefore the total mass flow rate in the solar field is the product of the mass flow rate in three modules by the number of parallel lines. It is also important to note that the water circulating through the industry drying section is at liquid state.

3.6 Collector Loop Pressure Drop

Classical formulae are used to evaluate the pressure drop and power requirement along the LFC pipe system. Properties are evaluated at average temperature in the absorber. The estimation of the pressure drop is with an assumption of internal flow in a straight pipe (neglecting joints and bends) to have an order of the magnitude idea of the power requirement in the LFC loop.

The Bernoulli‟s head loss and pressure drop can be written as the function of Fanning friction factor, f. Zigrang-Sylvester equation is used to evaluate the friction factor, where ε is the surface roughness of the pipe material (for steel ε =0.015mm).

$$\frac{1}{\sqrt{f}} = -4\log[\frac{\varepsilon}{3.7D_{Abs,i}} - \frac{5.02}{Re_{HTF}}\log(\frac{\varepsilon}{3.7D_{Abs,i}} + \frac{12}{Re_{HTF}})] \tag{3.30}$$

$$\Delta P = 2f(\frac{L}{D_{Abs,i}})(\rho_{HTF} * V^2) \tag{3.31}$$

$$Power = \Delta P * Q(kW) \tag{3.32}$$

In Equation 3.30 through 3.32;

- $D_{Abs,i}$ represents internal diameter of the absorber pipe
- Re_{HTF} the Reynolds number inside the absorber pipe
- ρ_{HTF} the density of heat transfer fluid
- V the velocity of the HTF inside the pipe
- ΔP the pressure drop
- L the total length of the absorber pipe
- Q the volume flow rate inside the pipe in m^3/s.

3.7 Heat Exchanger

Figure 3.11 shows a schematic of an adiabatic countercurrent heat exchanger with inlet and outlet temperatures and capacitance rates of the hot and cold fluids.

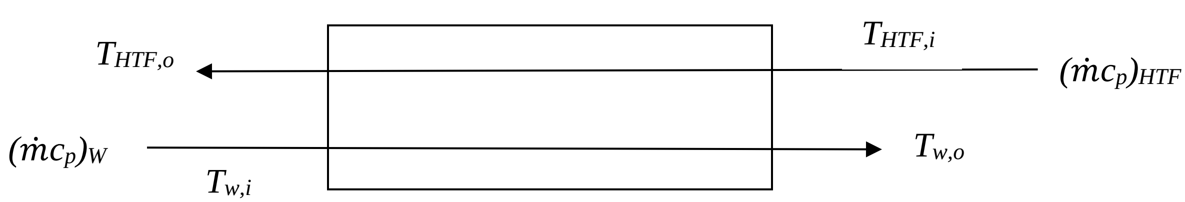

Figure 3.11: Schematic of an adiabatic counterflow heat exchanger (Duffie and Bechman, 2013)

The heat transfer based on the maximum possible temperature drop of the hot fluid from HTF inlet temperature ($T_{HTF,i}$) to water inlet temperature ($T_{w,i}$) can be expressed as (Duffie and Bechman, 2013):

$$Q_{max} = \left(\dot{m}c_p\right)_{HTF}(T_{HTF,i} - T_{w,i}) \tag{3.33}$$

The maximum possible temperature rise of the cold fluid would be from $T_{w,i}$ to $T_{HTF,i}$. The corresponding maximum heat exchange would be

$$Q_{max} = \left(\dot{m}c_p\right)_{w}(T_{HTF,i} - T_{w,i}) \tag{3.34}$$

The maximum heat transfer that could occur in the exchanger is thus fixed by the lower of the two capacitance rates, $\left(\dot{m}c_p\right)_{min}$and is given by:

$$Q_{max} = \left(\dot{m}c_p\right)_{min}(T_{HTF,i} - T_{w,i}) \tag{3.35}$$

Based on energy balance between HTF and water the actual heat exchange Q is given by

$$Q_{max} = \left(\dot{m}c_p\right)_{w}\left(T_{w,o} - T_{w,i}\right) = \left(mc_p\right)_{HTF}(T_{HTF,i} - T_{HTF,o}) \tag{3.36}$$

The actual heat exchange Q can also be related with overall heat transfer coefficient U and mean temperature difference ΔT_m which can be written as (Duffie and Bechman, 2013):

$$\mathrm{Q} = UA\Delta T_m \tag{3.37}$$

Where A is the total surface area of heat exhanger.

Effectiveness,ε is defined as the ratio of the actual heat exchange that occurs to the maximum possible, Q/Q_{max},

$$\varepsilon = \frac{Q}{Q_{max}} = \frac{\left(mc_p\right)_{HTF}(T_{HTF,i} - T_{HTF,o})}{\left(\dot{m}c_p\right)_{min}(T_{HTF,i} - T_{w,i})} = \frac{\left(\dot{m}c_p\right)_{w}(T_{w,o} - T_{w,i})}{\left(\dot{m}c_p\right)_{min}(T_{HTF,i} - T_{w,i})} \tag{3.38}$$

Since either the hot or cold fluid has the minimum capacitance rate, the effectiveness can always be expressd interms of the temperatures only.The working equation for the heat exchanger can be given by (duffie and beckman, 2013).

$$Q = \left(\dot{m}c_p\right)_{min}(T_{HTF,i} - T_{w,i}) \quad (3.39)$$

The dimensionless capacitance rate is given by :

$$C_r = \frac{(\dot{m}c_p)_{min}}{(\dot{m}c_p)_{max}} \quad (3.40)$$

Once Q_{max} and the effectiveness have been calcualted, the actual heat transfer between fluid streams can be determined as:

$$h_{w,o} = h_{w,i} + \frac{Q}{\dot{m}_w}. \quad (3.41)$$

The exit enthalphy, $h_{HTF,o}$, of the HTF is determined from an energy balance on the fluid:

$$h_{HTF,o} = h_{HTF,i} + \frac{Q}{\dot{m}_{HTF}} \quad (3.42)$$

The UA for the heat exchanger at the reference state is provided as a parameter to the exchanger model.at partial loads, the UA will decrease with the decreasing flow rates of the streams. The relationship between the reference UA/flow rate and a reduced UA/flow rate can be derived. The UA of an unfinned, tubular heat echanger is defined as the total termal resistance to heat transfer between two fluids.

$$\frac{1}{UA} = \frac{1}{h_i A_i} + \frac{R_{fi}{''}}{A_i} + \frac{\ln({}^{D_o}/_{D_i})}{2\pi kL} + \frac{R_{fo}{''}}{A_o} + \frac{1}{h_o A_o} \quad (3.43)$$

Where:

- h represents convective heat trnasfer coefficient
- A is surface area
- $R_f{''}$ is fauling factor,per unit area
- D is diameter
- k is the thermal conductivity of the material between the fluids
- L is the length of the heat exchanger
- Subscripts i and o refer to inner and outer tube surfaces

If it is assumed that there is negligible fauling in the heat exchangers and that the thermal resistance through the tubes can be neglected.With this assumptions, Equation 3.43 is reduced to:

$$\frac{1}{UA} = \frac{1}{h_i A_i} + \frac{1}{h_o A_o} \tag{3.44}$$

UA is a function of the inner and outer surface areas of the tubes and the heat transfer coefficient of each fluid. The surface area of the tubes will not change with partial load conditions.

3.8 Solar Radiation Estimation

For concentrator solar thermal energy systems, the tasks of performance simulation and succeeding economic evaluation require accurate estimates of direct beam irradiation data. This data is available from some weather ground stations. Solar irradiation data can also be derived from satellite imagery, where models of surface and cloud reflectivity allow the solar radiation at ground level to be estimated with reasonable accuracy. The purpose of this section is therefore to use the available sources of solar irradiation data, which is found from National Metrological Agency to arrive at a good estimate of the solar resource at Adama city, in such a way that subsequent modelling can predict the LFC system output with some confidence.

In this paper an empirical model to predict and estimate solar radiation is used due to the fact that there is a scarcity of trustworthy solar radiation data in the region. These models use climatological parameters of the location under study. Among which sunshine hours are the most widely and commonly used.

3.8.1 Calculation of Extraterrestrial Radiation

Extraterrestrial radiation is the amount of energy received per unit time on a unit area of a surface perpendicular to the sun outside the atmosphere of the earth**.** An astronomical model is used for determining the sun's position in the sky (as seen from Adama) as a function of the day of the year and of the time of the day. This model allows calculating for each day of the year, the day time duration, and, $\overline{H}_0$, the global daily solar irradiation (J/m^2 day) received by a horizontal surface located at the upper limit of the earth atmosphere.

Solar hour angle should be calculated first and to calculate the hour angle ω at any time for a specific location, a correction between local time and solar time must be made. Solar time is a time based on the apparent angular motion of the sun across the sky with solar noon the time the sun crosses the meridian of the observer and it is given by (Duffie and Beckman, 2013):

$$solar\ time = standard\ time + 4(L_{st} - L_{loc}) + E \qquad (3.45)$$

Where L_{st} represents Standard Meridian for the local time zone; in degrees west; 0° $\leq L_{st} \leq$ 360°, L_{loc} represents Longitude of the location in question; in degrees west; 0° ≤ L_{loc}≤ 360°. The parameter E is the equation of time (in minutes), and is given by (Duffie and Beckman, 2013):

$E = 229.2(0.000075 + 0.001868cos\beta - 0.032077sin\beta - 0.014615cos2\beta - 0.04089sin2\beta)$....(3.46)

In equation 3.46, B is obtained by using equation (Duffie and Beckman, 2013)

$$B = (n-1)\frac{360}{365} \qquad (4.47)$$

Where n is the nth day of the year, thus $1 \leq n \leq 365$

Hour Angle: angular displacement of sun east or west of the local meridian due to rotation of earth on its own axis at 15°/hour; morning negative, afternoon positive. And is given by (Duffie and Beckman, 2013)

$$\omega = 15(solar\ time - 12) \qquad (3.48)$$

Declination angle, angular position of the sun at solar noon (i.e., when the sun is on the local meridian) with respect to the plane of the equator, north positive; -23.45° ≤ δ ≤ 23.45°.The declination, δ, can be calculated using the approximate equation of Cooper (Duffie and Beckman, 2013)**:**

$$\delta = 23.45\sin(\frac{360}{365}(284 + n)) \qquad (3.49)$$

Where n is the nth day of the year.

The zenith angle θ_Z, the angle between the vertical and the line to the sun that is the angle of incidence of beam radiation on a horizontal surface. The relationship between the angle of incidence θ and the other angles is given by (Duffie and Beckman, 2013):

$$cos\theta = sin\delta sin\varphi cos\beta - sin\delta cos\varphi sin\beta cos\gamma + cos\delta cos\varphi cos\beta cos\omega + cos\delta sin\varphi sin\beta cos\gamma cos\omega + cos\delta sin\beta sin\gamma sin\omega \qquad (3.50)$$

If the slope, β, and the surface azimuth angle, γ , are zero, the above-mentioned relationship can be simplified to obtain the zenith angle:

$$cos\theta_Z = cos\ \varphi cos\ \delta cos\omega + sin\varphi sin\ \delta \tag{3.51}$$

Where: φ refers to the latitude and is equal to 8.54° for Adama.

At sunrise, the hour angle magnitude,ω_{sr}, and the local solar time, ST_{sr}, are calculated as follows:

$$cos\omega_{sr} = -tan\ \varphi tan\ \delta \tag{3.52}$$

$$ST_{sr} = 12 - \frac{\omega_{sr}}{15} \tag{3.53}$$

The local solar time at sunset, ST_{ss}, is given by:

$$ST_{ss} = 12 + \frac{\omega_{ss}}{15} \tag{3.54}$$

Thus, the day time duration, N (h), equals:

$$N = \frac{2}{15}\omega_{sr} \tag{3.55}$$

The global daily solar irradiance received by a horizontal surface at the upper limit of earth atmosphere, is calculated as follows (expressed in J/m^2 /day):

$$\overline{H}_0 = \frac{24*3600}{\pi} I_{SC}\left[1 + 0.033\cos\left(\frac{360n}{365}\right)\right] * \left[cos\varphi cos\delta sin\omega_{sr} + \pi\frac{\omega_{sr}}{180} sin\varphi sin\delta\right] \tag{3.56}$$

Where I_{SC} is the solar constant, is 1367 W/m^2.

3.8.2 Calculation of Monthly Average Daily Global Radiation on a Horizontal Surface

The monthly mean daily global radiation on a horizontal surface may be estimated from sunshine records by the modified Angstrom correlation, as suggested by Page and others as (Duffie and Beckman, 2013):

$$\frac{\overline{H}}{\overline{H}_o} = a + b\frac{n_s}{N_s} \tag{3.57}$$

Where $\overline{H}$ is global daily solar radiation on horizontal surface, $\overline{H}_o$ is the global daily solar radiation outside of the atmosphere for the same location, a and b are empirical constants, (Values are evaluated by regression), n_s is the daily hours of bright sun shine and N_s is the maximum possible daily hours of bright sunshine.

The regression parameters a and b can be obtained from:

$$a = -0.110 + 0.235cos\phi + 0.323(\frac{n_s}{N_s}) \tag{3.58}$$

$$b = 1.449 + 0.553cos\phi - 0.694(\frac{n_s}{N_s}) \tag{3.59}$$

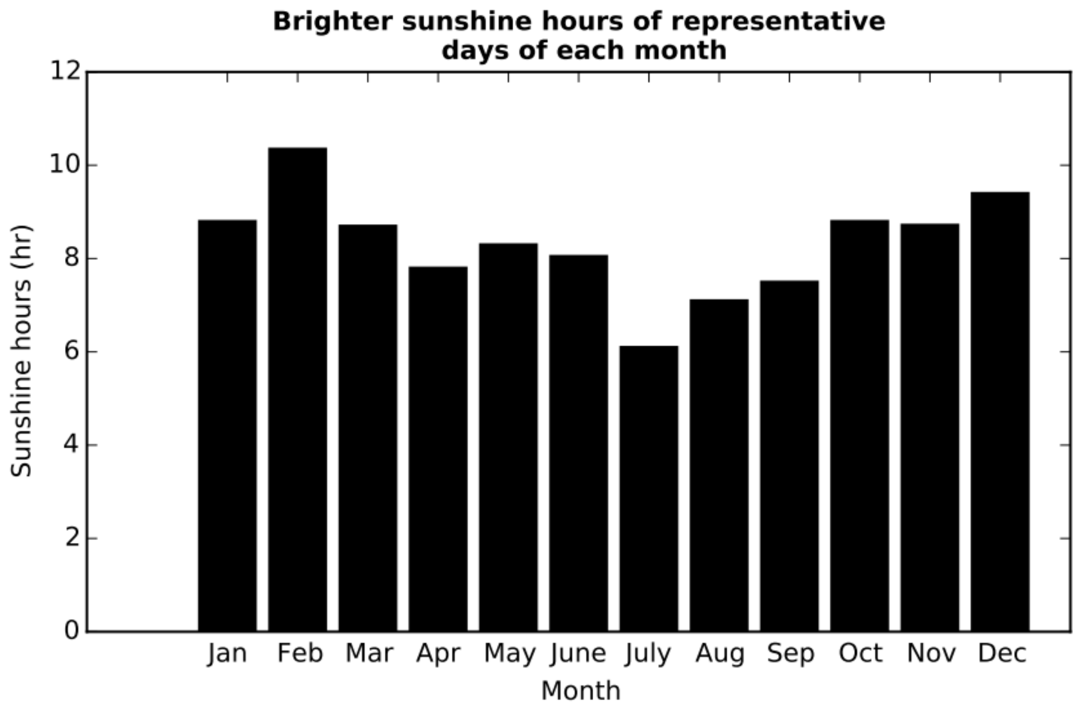

Figure 3.12: Bright sunshine hours for the representative days of each month for Adama (Ethiopia National Meteorology Agency)

3.8.3 Calculation of the Beam and Diffuse Daily Solar Irradiation on a Horizontal Surface

The monthly average daily diffuse radiation on a horizontal surface, $\overline{H}_d$, can be determined from the monthly average daily global radiation on a horizontal surface and the number of bright sunshine hours (Duffie and Beckman, 2013):

$$\frac{\overline{H}_d}{\overline{H}} = 0.931 - 0.814(\frac{n_s}{N_s}) \tag{3.60}$$

The daily beam solar radiation hitting a horizontal surface at ground level, $\overline{H}_b$ (J/m^{2}day), is can be found by simple deduction:

$$\overline{H}_b = \overline{H} - \overline{H}_d \tag{3.61}$$

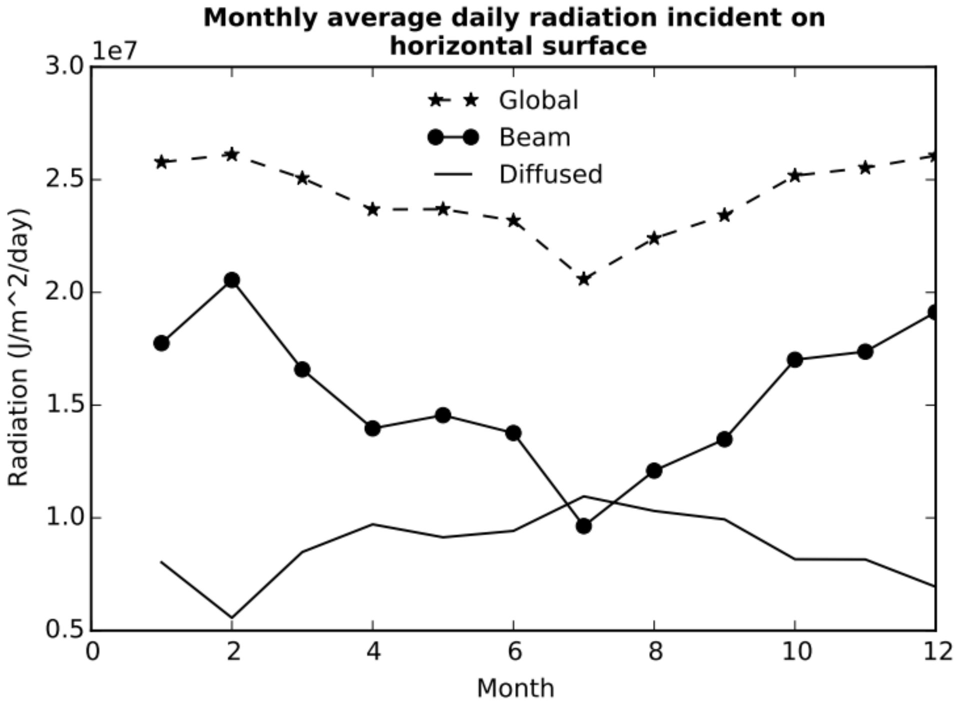

Figure 3.13: Monthly average daily global, beam and diffused radiation on a horizontal surface

3.8.4 Prediction of Monthly Average Hourly Radiation from Sunshine Duration

The monthly average hourly beam and diffuse radiation on a horizontal surface can be calculated from the knowledge of the monthly average daily global radiation on a horizontal surface by using the expression proposed by Collares-Pereira and Rabl, 1979, **(**Duffie and Beckman, 2013**).** In this thesis a one second resolution of solar radiation is taken for transient analysis in the subsequent sections. thick marks are used only for of differentiating between plots.

$$\bar{I}_d = \frac{\pi}{24*3600}[a + bcos\omega] * \frac{cos\omega - cos\omega_{sr}}{sin\omega_{sr} - \frac{\pi\omega_{sr}}{180}cos\omega_{sr}}\overline{H}_d \tag{3.62}$$

$$\bar{I}_b = \frac{\pi}{24*3600}[a + bcos\omega] * \frac{cos\omega - cos\omega_{sr}}{sin\omega_{sr} - \frac{\pi\omega_{sr}}{180}cos\omega_{sr}}\overline{H}_b \tag{3.63}$$

Where

$$a = 0.409 + 0.502\sin(\omega_{sr} - 60) \quad (3.64)$$

$$b = 0.661 - 0.447\sin(\omega_{sr} - 60) \quad (3.65)$$

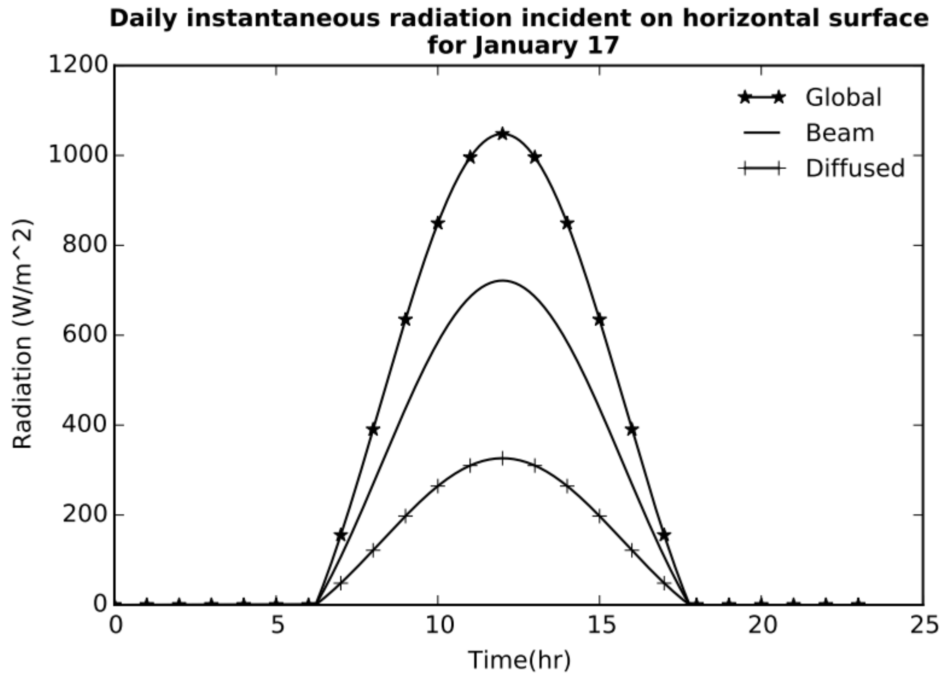

Figure 3.14: Global, beam and diffused radiation on a horizontal surface in January 17

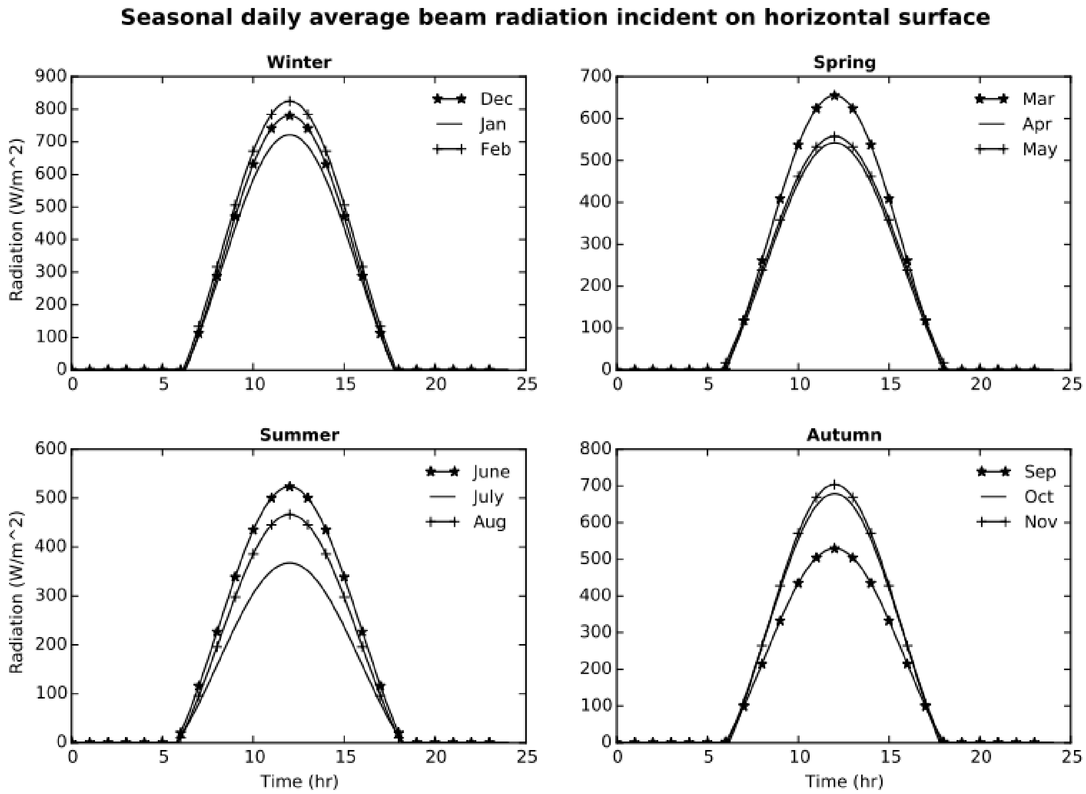

Figure 3.15: Instantaneous beam radiation on a horizontal surface for Adama seasons

3.8.5 Climatic Conditions

Adama region is characterized by a tropical climatic condition having high intensity of solar radiation. The monthly average temperature of Adama ranges between 18.7 ^{o}C in December and 22.8 ^{o}C in April. Five year average monthly average temperatures and wind speed in Adama are presented in Table 3.4.

Table 3.4: Monthly average annual climatic condition of Adama (Ethiopia National Meteorology Agence)

Temperature	Month											
	Jan	Feb	Mar	Apr	May	June	July	Aug	Sep	Oct	Nov	Dec
Min(^{o}C)	11.6	13.1	14.3	15.2	14.7	16.1	12.4	15.1	14.8	12.5	10.9	11
Max(^{o}C)	27.3	29.4	30.0	29.1	30.4	29.4	26.1	26.3	28.4	28.1	27.5	26.3
Average(^{o}C)	19.5	21.3	22.7	22.2	22.6	22.8	19.3	20.7	21.4	20.3	19.2	18.7
Wind speed	3.5	2.7	3.2	3.5	3.1	2.8	3.1	2.7	2.8	34	4.2	3.6

An estimation of hourly dry bulb temperature can be approximated from the daily mean maximum and daily mean minimum temperatures. A sinusoidal variation of the dry-bulb temperature throughout the day and the maximum temperature at 15:00 h sun time is assumed. The hourly variation of temperature, T(t) at any time t is given by:

$$T(t) = T_{max} - \frac{(T_{max} - T_{min})}{2}\left(1 - \sin(\frac{\pi t - 9\pi}{2})\right) \qquad (3.66)$$

Where, T_{max} is mean daily maximum temperature at 15:00 h sun time and $T_{min)}$ is mean daily minimum temperature. Figure 3.16 shows the diurnal atmospheric variation of Adama for one month in each seasons.

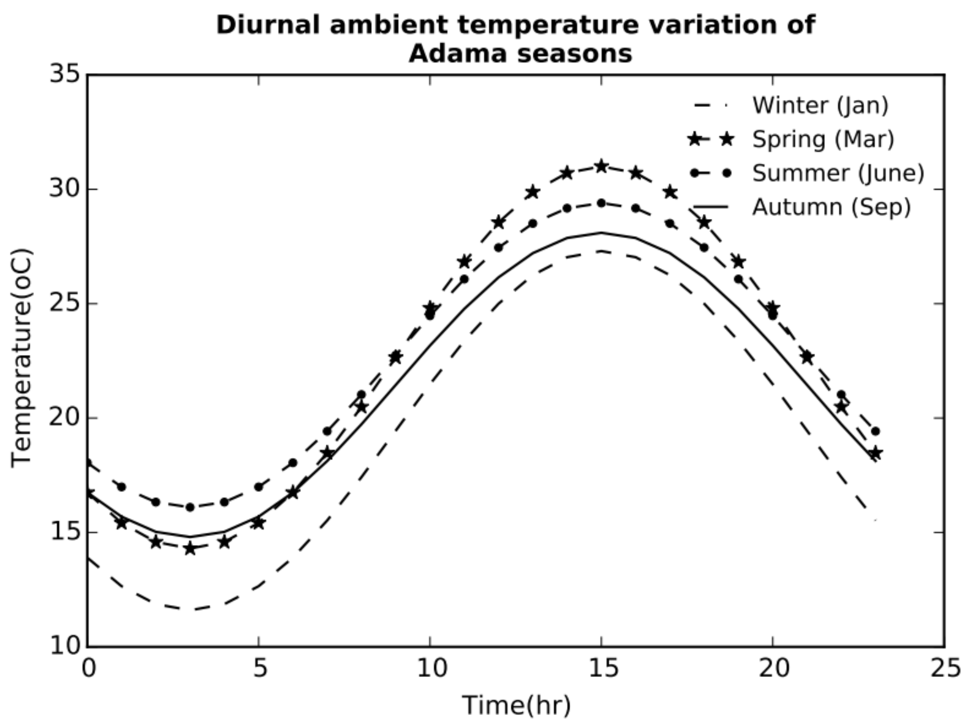

Figure 3.16: Diurnal ambient temperature variation of Adama seasons

CHAPTER FOUR

MODELING OF HEAT COLLECTING ELEMENT

4.1 Introduction

Linear Fresnel collectors are one of concentrated solar collector types used for power production in solar electric (power) generation and industrial process heating applications. LFCs comprise of a flat or slightly curved shiny surface to reflect solar beams on a heat collection element, known as receiver. The receiver may have single or multiple tubes depending on its construction.

In case of single tube construction as shown in Figure 4.1 the receiver carries heat transfer fluid and is usually covered with glass to minimize heat losses to the surroundings. In addition most LFCs use secondary concentrators to minimize spillage of reflected solar rays. Not shown in Figure 4.1 are bellows between different parts of the receiver to allow differential expansion between the glass and the stainless steel. There are flexible metallic hoses, between the receivers themselves and between the collector loops. Heat transfer fluid is usually water or oil for their heat capacity as well as their economical availability. However direct steam generation is also possible. Figure 4.1 shows the schematic of typical LFC receiver.

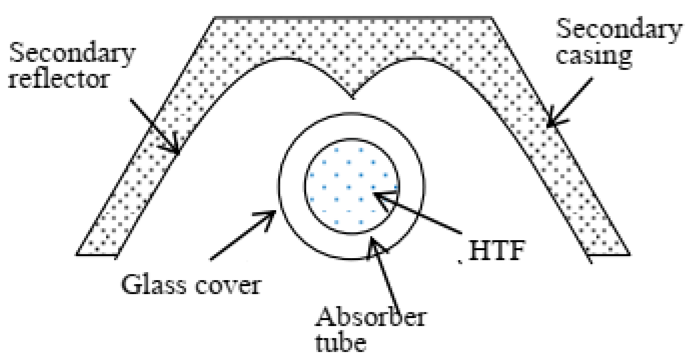

Figure 4.1: Schematic of a typical LFC heat collecting element (receiver) (Mohamed and Amr, 2016)

The heat transfer between the different parts of the receiver is shown in Figure 4.2. The sun's energy, reflected by the mirrors, falls on the absorber after passing through the glass envelope.

This absorbed solar energy is not fully transmitted to the HTF. There are heat losses from the absorber to the glass envelope. The glass envelope in turn is losing heat to the environment. These energy considerations lead to the development of the collector model. Here, only the absorber is assumed to be heated and no absorption on the secondary reflector is considered. This is a common state of art configuration and is similar to the modelling approach for parabolic trough receiver. The estimation of the absorbed solar energy from the direct normal solar radiation after optical losses is already discussed in the previous chapter.

4.2 Two-Dimensional Energy Balance Model of Receiver

The temperatures of the absorber, glass cover and heat transfer fluid are highly coupled and depend upon different modes of heat transfer of the system. Figure 4.2 shows the detail description of the modes of heat transfer.

A similar model is developed based on previous studies (Mohamed and Amr, 2016; Mokhtar et al., 2019) in which a two-dimensional term refers to building the thermal model for the simple cylindrical tube case by dividing a certain length of the absorber into N equal segments where energy balance correlations are sequentially solved for the first to the last segment through iteration and using explicit numerical methods. The radial heat flux is assumed to be homogeneously distributed normal to the tube circumference surface. The absorber wall temperature and heat transfer coefficient are assumed to be constant along each segment. With these assumptions, no longitudinal conduction through the absorber wall is taken into account in calculation, and the energy is transferred along the tube is merely by HTF. Thus, the two dimensional energy balance can be treated similar to the one-dimensional energy model (Forristall, 2003).

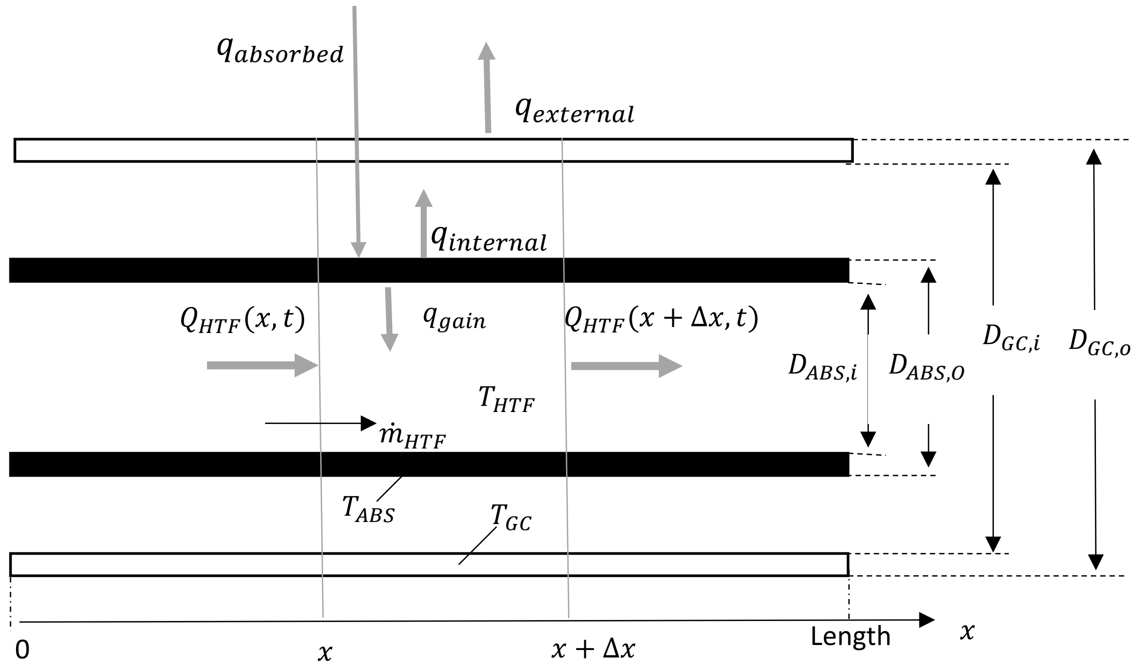

Figure 4.2: Schematic of the receiver

Assumptions

For the current LFC analysis, following assumptions are considered:

- One dimensional analysis is considered.
- Uniform and incompressible fluid flow neglecting any change of phase of the fluid with in the working temperature range.
- Material properties of air, receiver and glass cover are considered as constant with in the working temperature range.
- Constant wind velocity for the convective heat loss between glass cover and surroundings.
- Constant diameters of receiver and glass cover (thermal expansion is neglected).
- Longitudinal conduction heat transfer of the glass cover and the absorber is neglected.
- The axial conduction through the absorber and the glass cover is considered negligible due to their small thickness.
- Heat conduction along the supporting brackets is neglected.
- The heat transfer interaction of the compound parabolic concentrator (CPC) with the receiver is not taken in to consideration.

- The fluid enters the collector at a constant inlet temperature.
- Optical properties are independent of temperature.
- The glass cover is considered opaque to infrared radiation.
- The effective solar irradiation is considered as totally absorbed by the absorber selective coating since the absorption in the glass is neglected (solar absorptance about 0.02).

4.2.1 Heat Transfer Fluid Energy Balance

The modeling of the collector, as shown in Figure 4.2, starts by an energy balance for the HTF, which leads to a partial differential equation for the HTF temperature. The distance along the collector is indicated by x. The equation for the HTF heat change over time t on an element of length Δx at position x is:

$$\frac{\partial(Q_{HTF}(x,t))}{\partial t} = q_{gained}(x,t)\Delta x + Q_{HTF}(x,t) - Q_{HTF}(x+\Delta x,t) \tag{4.1}$$

Here q_{gained} is the heat transfer per length between the absorber and the HTF.

From thermodynamics, it follows that

$$Q_{HTF}(x,t) = \rho_{HTF} c_{HTF} A_{ABS,i}\, \Delta x\, T_{HTF}(x,t) \tag{4.2}$$

Where,ρ_{HTF}, c_{HTF} and T_{HTF} density, specific heat capacity and temperature of the heat transfer fluid, respectively. It is important to notice that the density and the specific heat capacity terms depends on the HTF temperature. $A_{ABS,i}$, represents the cross-sectional area of the inside absorber tube. The last two terms in the right side of equation 4.1 can be represented by partial differential equation:

$$Q_{HTF}(x,t) - Q_{HTF}(x+\Delta x,t) = \rho_{HTF} c_{HTF} \dot{V}_{HTF} \frac{\partial(T_{HTF}(x,t))}{\partial x} \tag{4.3}$$

Substituting Equation 4.2 and 4.3 in to Equation 4.1 with some arrangements a partial differential equation is obtained for the HTF temperature given by (Mokhtar et al., 2019):

$$\rho_{HTF} c_{HTF} A_{ABS,i} \frac{\partial(T_{HTF}(x,t))}{\partial t} = q_{gained}(x,t) - \rho_{HTF} c_{HTF} \dot{V}_{HTF} \frac{\partial(T_{HTF}(x,t))}{\partial x} \tag{4.4}$$

$\dot{V}_{HTF}$ is the volume flow rate of the heat transfer fluid in the absorber tube and depends only on the time t since the fluid is considered to be incompressible.

4.2.2 Absorber Energy Balance

Similar to equation 4.1, the differential equation for the absorber temperature, T_{ABS} , is obtained:

$$\frac{\partial(Q_{ABS}\,(x,t))}{\partial t} = \left(q_{absorbed}(t) - q_{internal}\,(x,t) - q_{gained}\,(x,t)\right)\Delta x \tag{4.5}$$

Here, $q_{internal}$ is the heat transfer per length between the absorber and the glass envelope. q_{gained} is the energy gain of the flowing heat transfer fluid through the absorber. From thermodynamics it is known that:

$$\Delta Q_{ABS}\,(x,t) = \rho_{ABS} c_{ABS} A_{ABS}\,\Delta x\; T_{ABS}(x,t) \tag{4.6}$$

Where ρ_{ABS} , c_{ABS} and T_{ABS} are the absorber density, specific heat and temperature, respectively. The cross-sectional area of the absorber is A_{ABS} . Substituting equation 4.6 into equation 4.5 and after a division by Δx (Mokhtar et al., 2019).

$$\rho_{ABS} c_{ABS} A_{ABS} \frac{\partial T_{ABS}(x,t)}{\partial t} = q_{absorbed}(t) - q_{internal}(x,t) - q_{gained}(x,t) \tag{4.7}$$

$q_{absorbed}$ is absorbed solar energy accounting optical losses of the primary and secondary reflectors. It is the function of beam component of solar radiation, optical characteristics and mean daily Incident Angle Modifier (IAM) of the collector (refer to Equation 3.26).

4.2.3 Glass Cover Energy Balance

The energy balance model for the glass cover temperature is gained through considerations similar to those used to obtain the differential equation for the absorber temperature. It is also important to note that the glass envelope is assumed to have no radial temperature gradients (Mokhtar et al., 2019).

$$\rho_{GC} c_{GC} A_{GC} \frac{\partial T_{GC}(x,t)}{\partial t} = q_{internal}(t) - q_{external}(x,t) \tag{4.8}$$

Where ρ_{GC} , c_{GC} , T_{GC} are the envelope density, specific heat and temperature, respectively. The heat transfer per length between the envelope and the environment is $q_{external}$.

The interacting dynamic of the temperatures given through the energy balance Equations 4.4, 4.7 and 4.8 is determined by the heat transfer between the HTF, the absorber, the envelope and the environment. For this reason, it is important to discuss heat transfer phenomenon equations to estimate the occurring heat transfer.

4.3 Modeling of Heat Transfer Phenomenon Correlations

4.3.1 Heat Transfer between HTF and Absorber

The heat transfer from the receiver to fluid (q_{gained}) depends upon the temperature difference of fluid (T_{HTF}) and receiver (T_{ABS}) and the convective heat transfer coefficient (H_{HTF}) and is determined by newton's law of cooling (Incropera, et al., 2011):

$$q_{gained} = \pi D_{ABS,i}\, h_{HTF}(T_{ABS} - T_{HTF}) \tag{4.9}$$

Where $D_{ABS,i}$ is the internal diameter of the absorber and h_{HTF} is convective heat transfer coefficient between the HTF and the absorber at T_{HTF}. For the single-phase flow calculation of the heat transfer coefficient requires knowledge on the Nusselt number and HTF conductivity and is given by (Incropera, et al., 2011):

$$h_{HTF} = Nu_{ABS,i}\,\frac{k_{HTF}}{D_{ABS,i}} \tag{4.10}$$

Where:

- $D_{ABS,i}$ represents absorber inner diameter
- k_{HTF} the thermal conductance of the HTF at T_{HTF}
- $Nu_{ABS,i}$ the Nusselt number based on $D_{ABS,i}$

The Nusselt number depends on the type of flow through the absorber. At typical operating conditions, the flow in an absorber is well within the turbulent flow region. However, during off-solar hours, the flow in the absorber tube may become transitional or laminar because of the viscosity of the HTF at lower temperatures. Therefore, to model the heat losses under all conditions, the model must include all the flow regimes to determine type of flow. The Nusselt number used for each flow condition is outlined.

To model the convective heat transfer from the absorber to the HTF for turbulent and transitional cases (Reynolds number > 2300) the following Nusselt number correlation developed by Gnielinski (1976) is used (Incropera, et al., 2011).

$$Nu_{HTF} = \frac{f/8(Re_{HTF}-1000)Pr_{HTF}}{1+12.7\sqrt{f/8}\left(Pr_{HTF}^{2/3}-1\right)}\left(\frac{Pr_{HTF}}{Pr_{ABS}}\right)^{0.11} \tag{4.11}$$

Here, Re expresses the Reynolds number based on inner absorber diameter and is given by:

$$Re_{HTF} = \frac{\dot{m}_{HTF}\, D_{ABS,i}}{A_{ABS}\, \mu_{HTF}} \tag{4.12}$$

The friction factor "f" at the inner absorber wall with assumption of smooth pipe with no roughness and is given by Mokhtar et al., (2019):

$$f = (1.82\log_{10}(Re_{HTF}) - 1.64)^{-2} \tag{4.13}$$

Pr_{HTF} is Prandtl number, and it is evaluated at the bulk mean temperature of HTF while Pr_{ABS} is evaluated at the inner absorber surface temperature. The Gnielinski's correlation is valid for large range of Reynolds and Prandtl number. It is considered to be valid for 2300 $\leq Re \leq 10^6$ and 0.5 $\leq Pr \leq$ 2000 (Mokhtar et al., 2019). Prandtl number is calculated by the following equation:

$$Pr_{HTF} = \frac{\nu_{HTF}}{\alpha_{HTF}} \tag{4.14}$$

Where ν_{HTF} is the kinematic viscosity; the ratio of the HTF kinematic viscosity, μ_{HTF} and density of the HTF, ρ_{HTF}. The fluid thermal diffusivity α_{HTF} is calculated as follow:

$$\alpha_{HTF} = \frac{k_{HTF}}{\rho_{HTF} \times C_{HTF}} \tag{4.15}$$

For laminar flows, i.e. Reynolds number less than 2300, convective heat transfer coefficient, h_{HTF}, can be calculated using Equation (Incropera, et al., 2011).

$$h_{HTF} = \frac{4.36 k_{HTF}}{D_{ABS,i}} \tag{4.16}$$

4.3.2 Heat Transfer between the Absorber and the Glass cover

The heat transfer between the absorber and the glass cover, $q_{internal}$ consists of convection and radiation heat transfers.

$$q_{internal} = q_{internal,conv} + q_{internal,rad} \tag{4.17}$$

Assuming only partial evacuation of the annulus between the absorber and the glass cover, the occurring free convection is estimated through relations for a free convection flow in the annular space between long, horizontal, concentric cylinders (Incropera, et al., 2011). The air ascends along the absorber and descends along the glass envelope since the glass envelope is usually cooler than the absorber ($T_{ABS} > T_{GC}$).The convection heat transfer, $q_{Internal,conv}$, may be expressed as (Mokhtar et al., 2019).

$$q_{internal,conv} = h_{internal,conv}(T_{ABS} - T_{GC}) \tag{4.18}$$

The internal convection heat transfer coefficient is given by:

$$h_{internal,conv} = \frac{2\pi k_{eff,air}}{\ln\left({}^{D_{GC,i}}/_{D_{ABS,o}}\right)} \tag{4.19}$$

Here the effective thermal conductivity, $k_{eff,air}$ is the thermal conductivity that the stationary air should have to transfer the same amount of heat as moving air. The following correlation can be used for calculating $k_{eff,air}$ (Mokhtar et al., 2019).

$$\frac{k_{eff,air}}{k_{air}} = 0.386\left(\frac{Pr_{air}}{0.861+Pr_{air}}\right)^{\frac{1}{4}}(Ra_c{}^*)^{1/4} \tag{4.20}$$

Where

$$Ra_c{}^* = \frac{\left[\ln({}^{D_{GC,i}}/_{D_{ABS,o}})\right]^4}{L^3(D_{ABS,o}{}^{-3/5} + D_{GC,i}{}^{-3/5})} Ra_L \tag{4.21}$$

In Equation 4.20 k_{air} and Pr_{air} are the thermal conductivity and the prandtl number of air respectivily and in Equation 4.21, L represents the effective length and is given for the annulus by:

$$L = 0.5(D_{GC,i} - D_{ABS,o}) \tag{4.22}$$

The Rayleigh Number of air, Ra_L , is defined as

$$Ra_L = \frac{g\beta_{Air}(T_{ABS} - T_{GC})L^3}{\alpha_{air}\nu_{air}} \tag{4.23}$$

Where g is gravitational acceleration (g = 9.81m.s^{-2}), β_{Air} ,the volumetric thermal expansion coefficient of air and the thermal diffusivity of air, calculated as:

$$\alpha_{air} = \frac{k_{air}}{\rho_{air} c_{p,air}} \tag{4.24}$$

Here ρ_{air} is the density of air in the annulus and, $c_{p,air}$ is the specific heat of air. The kinematic viscosity of air, ν_{air}, is given by:

$$\nu_{air} = \frac{\mu_{air}}{\rho_{air}} \tag{4.25}$$

With the viscosity of air, μ_{air} .The properties of air in the annulus, α_{air} , β_{Air} , k_{air} , μ_{air} ,ν_{air} Pr_{air} and ρ_{air} are dependent on the mean temperature in the annulus (i.e.0.5($T_{ABS} + T_{GC}$)).

Radiation heat transfer Heat exchange through radiation between outer surface of absorber and inner glass cover surface can be calculated for long concentric cylinders in W/m as (Incropera, et al., 2011)

$$q_{internal,rad} = \pi D_{ABS,o} h_{internal,rad} (T_{ABS} - T_{GC}) \tag{4.26}$$

The internal radiative heat transfer coefficient is given by:

$$h_{internal,rad} = \frac{(T_{ABS}^2 - T_{GC}^2)(T_{ABS} - T_{GC})}{\frac{1}{\varepsilon_{ABS}} + \left(\frac{1-\varepsilon_{GC}}{\varepsilon_{GC}}\right)\left(\frac{D_{ABS,o}}{D_{GC,i}}\right)} \tag{4.27}$$

Where

- σ is the Stefan-Boltzmann constant, $5.67x10^{-8}\ W/m^2K^4$
- ε_{ABS} is emittance of absorber tube's outer surface
- ε_{GC} is emittance of inner glass cover surface

The total heat transfer coefficient in the annulus can be given as the summation of the radiation and the convection terms:

$$h_{internal} = h_{internal,conv} + h_{internal,rad} \tag{4.28}$$

4.3.3 Heat Transfer between Glass Envelope and the Environment

The heat transfer between the envelope and the environment is assumed to be due to convection and radiation.

Convection heat transfer from glass cover to surrounding

Similar to Section 4.3.1, Newton's law of cooling can be written between the absorber surface and the air stream around (Incropera, et al., 2011):

$$\dot{q}_{external,rad} = \pi D_{GC,i} \dot{h}_{air,amb}(T_{GC} - T_{amb}) \tag{4.29}$$

$$h_{air,amb} = \frac{k_{air,amb}}{D_{GC,o}} Nu_{GC,o} \tag{4.30}$$

Where:

- $k_{air,amb}$ represents the thermal conductance of air at $(T_{GC} + T_{amb})/2$
- T_{amb} the ambient temperature
- $h_{air,amb}$ the convection heat transfer coefficient for air at $(T_{GC} - T_{amb})/2$
- $Nu_{GC,o}$ the average Nusselt number based on glass cover outer diameter

Here, the Nusslet number is dependent upon the air stream velocity around the absorber that can be considered in two cases as follows:

No wind case: Under no wind condition, the convection heat transfer is purely done by a natural convection mechanism. In this case, the Nusselt number is estimated by Churchill and Chu's correlation valid for a long isothermal horizontal cylinder (Incropera, et al., 2011).

$$Nu_{GC,o} = \left\{0.60 + \frac{0.387 Ra_{GC,o}^{1/6}}{\left[1+\left(0.559/Pr_{GC,o}\right)^{9/16}\right]^{8/27}}\right\}^2 \tag{4.31}$$

$$Ra_{GC,o} = \frac{g\beta(T_{GC} - T_{amb})L^3}{\alpha_{air,amb}\nu_{air,amb}} \tag{4.32}$$

$$\beta = \frac{1}{T_{GC} + T_{amb}} \tag{4.33}$$

$$Pr_{air,amb} = \frac{\nu_{air,amb}}{\alpha_{air,amb}} \tag{4.34}$$

Where:

- $Ra_{GC,o}$ represents Rayleigh number for air based on the glass cover outer diameter,
- $Pr_{GC,o}$ the Prandtl number for air based on outer glass cover

- $\alpha_{air,amb}$ the kinematic viscosity for ambient air at film temperature $(T_{GC} + T_{amb})/2$
- β the volumetric thermal expansion coefficient (ideal gas)
- $\alpha_{air,amb}$ the thermal diffusivity for air at film temperature
- g the gravitational constant, 9.81 m/s^2

This correlation is valid for the Rayleigh number within the range $10^5 < Ra < 10^{12}$. In this correlation, a film of air with average temperature between the glass cover exterior surface and the ambient is considered for air property determination.

Wind case: The environmental air flows around the envelope with a wind speed, v_{wind}. The fluid motion is assumed to be normal to the axis of the envelope's circular cylinder. The heat transfer due to convection, $v_{external,conv}$, is estimated through a correlation suggested for a circular cylinder in cross flow (Incropera, et al., 2011).An average conditions is used here.

$$\overline{Nu}_{ENV,o} = 0.3 + \frac{0.62 {Re_{ENV,o}}^{1/2} {Pr_{air,amb}}^{1/3}}{\left[1+\left(\frac{0.4}{Pr_{air,amb}}\right)\right]^{1/4}} \left[1 + \left(\frac{Re_{ENV,o}}{280{,}000}\right)^{5/8}\right]^{4/5} \tag{4.35}$$

For the circular glass envelope cylinder, the Reynolds Number, $Re_{ENV,o}$, is defined as

$$Re_{HTF} = \frac{\rho_{air,amb}\, v_{wind} D_{GC,o}}{\mu_{air,amb}} \tag{4.36}$$

Where $\rho_{air,amb}$ represents the density of the ambient air, and $\mu_{air,amb}$ as the kinematic viscosity of the ambient air. $Pr_{air,amb}$ is the Prandtl number of the ambient air.

Radiation heat transfer between glass cover and environment

For calculation of the radiation heat loss in the parabolic trough application, it is assumed that the absorber tube is mostly seen by the sky; hence, the radiation heat transfer occurs by temperature differences between the glass cover and the effective sky temperature. As an approximation, the effective sky temperature is assumed 8°C below the ambient temperature (Forristall, 2008). However, this assumption is not applied for LFC due to the fact that in Fresnel systems, the absorber tube is mainly seen by the ground and mirror field. In this case, the effective sky temperature is assumed 5°C above the ambient temperature that will lead to a slightly lower radiation loss compared to the parabolic trough (Pye et al., 2006). The net radiation transfer between the glass cover envelope and surrounding becomes (Incropera, et al., 2011):

$$q_{absorbed,rad} = \pi D_{GC,o} \varepsilon_{GC} \sigma h_{external,rad} (T_{GC} - T_{amb}) \tag{4.37}$$

However absorption due to the glass cover is not considered in this model.

$$h_{external,rad} = \frac{\varepsilon_{GC} \sigma \left(T_{GC}^4 - T_{sky}^4\right)}{(T_{GC} - T_{amb})} \tag{4.38}$$

Where:

- σ represents the Stefan-Boltzmann constant, $5.67x10^{-8}\ W/m^2K^4$
- T_{sky} the effective sky temperature (K)
- ε_{GC} the emissivity of the glass cover

4.4 Transient Analysis of Linear Fresnel Receiver Using Finite Difference Method

In Section 4.2, the mathematical model used to simulate the dynamic behavior of LFCs is developed. To solve the model, the collector is divided in to three nodes (glass cover, absorber and fluid) perpendicular to the flow direction. The deferential equation describing the energy balance equations are solved using the explicit finite difference method. The thermo-physical properties of absorber and glass cover are considered to be independent of temperature. However, the thermo-physical properties of HTF is considered temperature dependent.

The transient temperatures are evaluated iteratively, using relations derived for the equation of energy balance for each node.

1. **Absorber**

$$\rho_{ABS} c_{ABS} A_{ABS} \frac{{T_{ABS}}^{t+\Delta t} - {T_{ABS}}^{t}}{\Delta t} = q_{absorbed} - \pi D_{ABS,o} h_{internal} \left({T_{ABS}}^{t} - {T_{GC}}^{t}\right) - \pi D_{ABS,o} h_{internal,conv} \left({T_{ABS}}^{t} - {T_{GC}}^{t}\right) - \pi D_{GC} h_{external,rad} \left({T_{GC}}^{t} - {T_{Amb}}^{t}\right) \tag{4.39}$$

After some transformations, the following formulae is obtained for temperature of absorber in a new time step:

$$T_{ABS,j}{}^{t+\Delta t} = (1 - B*\Delta t - C*\Delta t - D*\Delta t)T_{ABS,j}{}^{t} + A*\Delta t*q_{absorbed} + (B*\Delta t + C*\Delta t)T_{GC}{}^{t} + D*\Delta t*T_{HTF,i}{}^{t} \tag{4.40}$$

2. Heat transfer fluid

$$\rho_{HTF}c_{HTF}A_{HTF}\frac{(T_{HTF,j}{}^{t+\Delta t} - T_{HTF,j}{}^{t})}{\Delta t} = q_{absorbed,GC} + \pi D_{ABS,i}h_{HTF}\left(T_{ABS,j}{}^{t} - T_{HTF,j}{}^{t}\right) - \dot{m}c_p\frac{(T_{HTF,j}{}^{t} - T_{HTF,j-1}{}^{t})}{\Delta x} \tag{4.41}$$

Similar to the glass cover, the following formulae is obtained for temperature of glass cover in a new time step:

$$T_{HTF,j}{}^{t+\Delta t} = (E*\Delta t + F*\Delta t)T_{HTF,j}{}^{t} + E*\Delta t*T_{ABS,j}{}^{t} -*\Delta t*T_{HTF,j-1}{}^{t} \tag{4.42}$$

3. Glass Cover

$$\rho_{GC}c_{GC}A_{GC}\frac{T_{GC,j}{}^{t+\Delta t} - T_{GC,j}{}^{t}}{\Delta t} = q_{absorbed,GC} + \pi D_{ABS,o}h_{internal}\left(T_{ABS,j}{}^{t} - T_{GC,j}{}^{t}\right) - \pi D_{GC}h_{external,conv}\left(T_{GC,j}{}^{t} - T_{Amb,j}{}^{t}\right) - \pi D_{GC}h_{external,rad}\left(T_{GC,j}{}^{t} - T_{Amb}{}^{t}\right) \tag{4.43}$$

Similar to the glass cover, the following formulae is obtained for temperature of glass cover in a new time step:

$$T_{GC,j}{}^{t+\Delta t} = (1 - H*\Delta t - I*\Delta t - J*\Delta t)T_{GC,j}{}^{t} + G*\Delta t*q_{absorbed,GC} + H*\Delta t*T_{ABS,j}{}^{t} + (I*\Delta t + J*\Delta t)T_{amb}{}^{t} \tag{4.44}$$

In equation (4.40), (4.42) and (4.44) :

$$A = \frac{1}{\rho_{ABS}c_{ABS}A_{ABS}} \tag{4.45}$$

$$B = \frac{\pi D_{ABS,o}h_{internal,conv}}{\rho_{ABS}c_{ABS}A_{ABS}} \tag{4.46}$$

$$C = \frac{\pi D_{ABS,o}h_{internal,rad}}{\rho_{ABS}c_{ABS}A_{ABS}} \tag{4.47}$$

$$D=\frac{A_{ABS,i}\,h_{HTF}}{\rho_{ABS}c_{ABS}A_{ABS}} \tag{4.48}$$

$$E=\frac{A_{ABS,i}\,h_{HTF}}{\rho_{HTF}c_{HTF}A_{C,ABSi}} \tag{4.49}$$

$$F=\frac{\dot{m}}{\rho_{HTF}A_{ABS}\Delta x} \tag{4.50}$$

$$G=\frac{1}{\rho_{GC}c_{GC}A_{GC}} \tag{4.51}$$

$$H=\frac{\pi D_{ABS,o}h_{internal}}{\rho_{GC}c_{GC}A_{GC}} \tag{4.52}$$

$$I=\frac{\pi D_{GC,o}h_{internal,conv}}{\rho_{GC}c_{GC}A_{GC}} \tag{4.53}$$

$$J=\frac{\pi D_{GC,o}h_{internal,rad}}{\rho_{GC}c_{GC}A_{GC}} \tag{4.54}$$

Initial conditions

- The glass cover is at initial temperature of mean ambient air temperature and vary along the representative days.
- The absorber is assumed to be 15^{o}C above the ambient air.
- The fluid is assumed to be at an initial temperature of 150 ^{o}C.

Boundary condition

- The inlet HTF temperature in to the LFC should be higher than the required temperature in to the production line. An inlet temperature of 150 ^{o}C is assumed here base on Ah-wan food complex hot water temperature..

4.5 Solution Method

The equations and expressions discussed above and in the previous chapter form a physical model for the linear Fresnel collector field. In addition, the concrete TES model which is discussed in the next chapter is implemented. The models can be used to predict the outlet temperature verses time of the collector field with the known variables and parameters as an input. Based on the heat transfer fluid outlet temperature the useful heat and the efficiency of the collector can be defined.

Input parameters

- Geometrical properties
- Inner and outer diameters of the absorber and the glass envelope.
- Aperture area of the LFC.

Optical properties

- All the optical specifications that do not depend on the temperature; absorptivity, transmissivity, and emissivity of the glass envelope and absorptivity, emissivity of the absorber.

Geographical coordinates

- Latitude of the location.

Input variables

- Inlet temperature
- Mass flow rate
- Ambient temperature
- Thermal properties of the working fluid.

The LFC model consists of three parts: solar radiation model, optical model, and thermal model. For the solar radiation model, inputs are month, day, and Longitude and latitude of the system location. For the optical models, the inputs are all the optical specifications of the mirror and the tube including reflectivity, emissivity, transitivity, and absorptivity. For the thermal model, the energy balance system consists of three unknown temperatures and three non-linear transient partial differential equations. A concrete TES is also integrated in the simulation. To solve these problems a first order finite difference method is used which is discussed in Section 4.4. The simulation method can be summarized by flow chart given in Figure 4.3 and is it implemented in Python programming software.

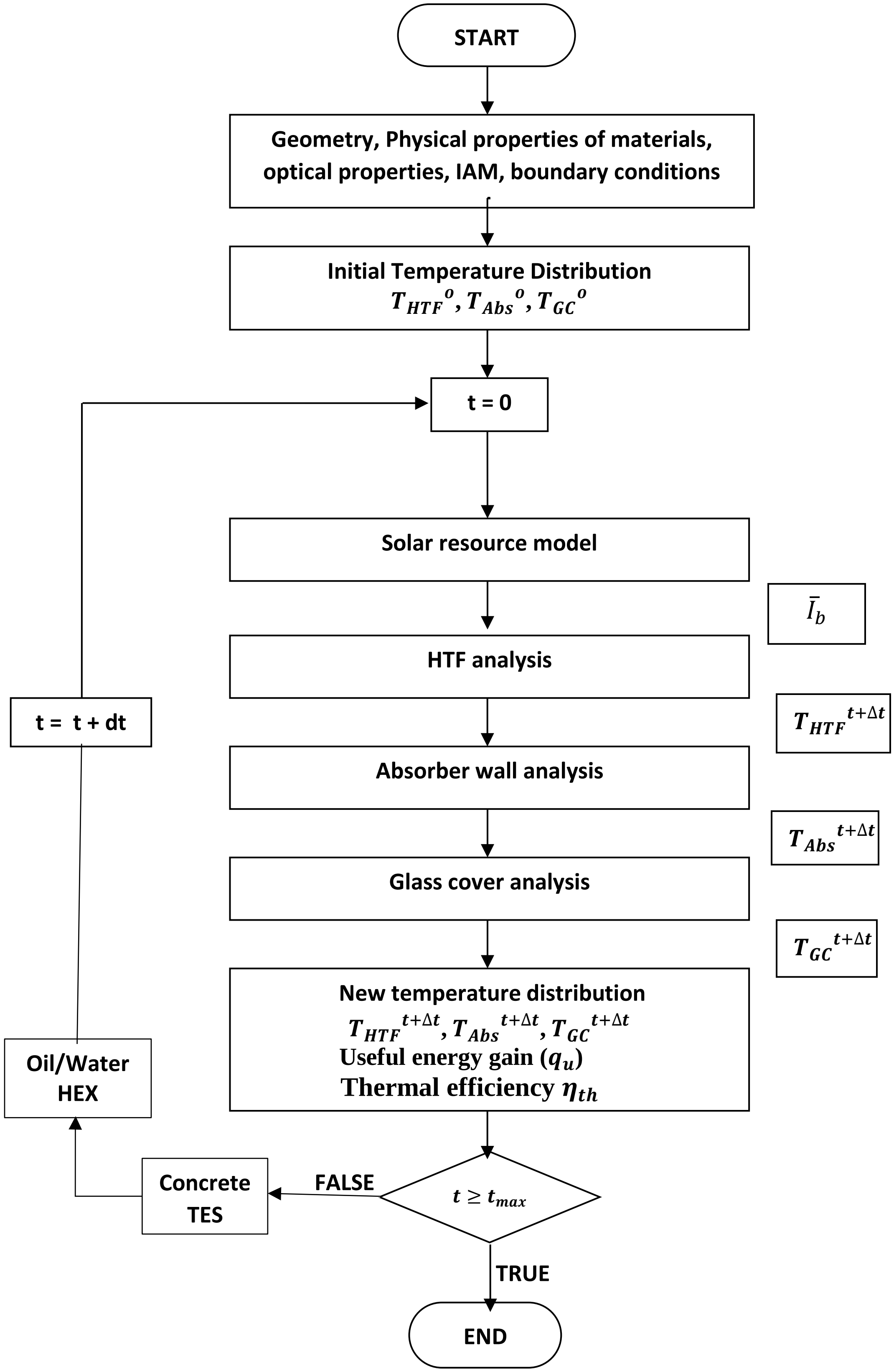

Figure 4.3: Flow chart of the collector simulation process

Grid sizing

In order to find the effect of the computational size (Number of nodes n) on the error and to achieve grid independency, the model is checked by simulating one single case at various grid sizes (65, 51, 41, 33 and 17 nodes). Results of 65 nodes are considered as the benchmark values to compare with the lesser grid sizes. The error is calculated for both the outlet temperature and useful energy gain at steady state. To check the grid independency, the working fluid inlet temperature in to the receiver is assumed varying with the flow rate of 0.39 kg/sec, 700 W/m^2 as the solar energy input, 27.3°C and 3.5 m/s as the average ambient temperature and wind speed respectively, are fed into the model as inputs.

Table 4.1: Grid independency test

Number of nodes	T_{HTF}	q_u
17	473.8122327	38.37056
33	473.7799401	38.346104
41	473.7735247	38.341245
51	473.7684026	38.337366
65	473.7639283	38.333977

$$Error_{T_{HTF}} = T_{HTF}(65) - T_{HTF}(n) \tag{4.55}$$

Equation 4.55 represents the error for the outlet temperature, where the $T_{HTF}(65)$ and $T_{HTF}(n)$ show the outlet temperature at 65 and lesser nodes (n), respectively.

Similarly, Equation 4.56 shows the error for the average useful energy gain at the steady state conditions, where $q_u(65)$ and $q_u(n)$ show the average useful energy gain at steady state conditions at 51 and lesser nodes.

$$Error_{q_u} = q_u(65) - q_u(n) \tag{4.56}$$

In Figure 4.4 errors at 51 nodes and 33 nodes are very similar. Although there is a little difference, with the operating temperature ranges these two nodes almost give the same outlet temperatures. Similarly, for the useful energy absorbed to the system at steady state, different nodes also show insignificant errors. Hence, in order to save the computational resources, the model is implemented with 33 nodes.

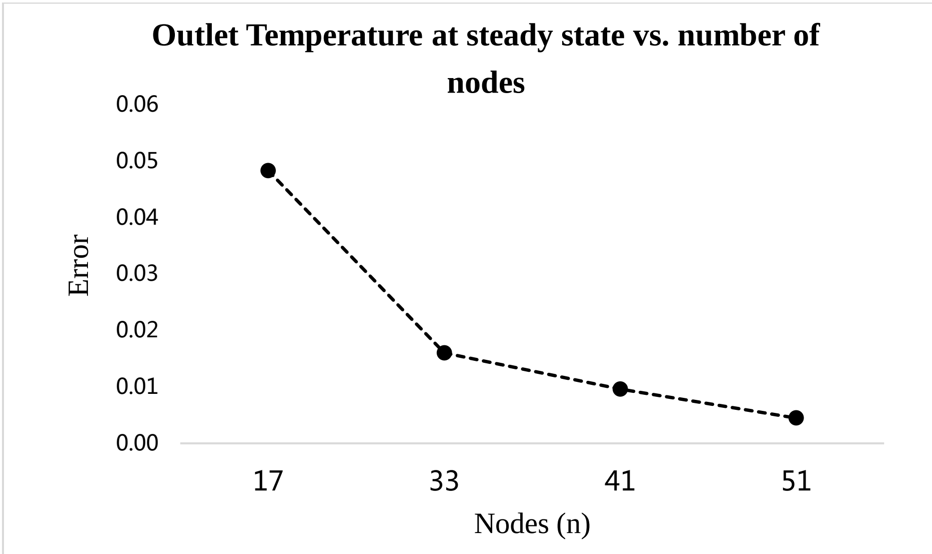

Figure 4.4: Error vs. number of nodes of outlet temperature

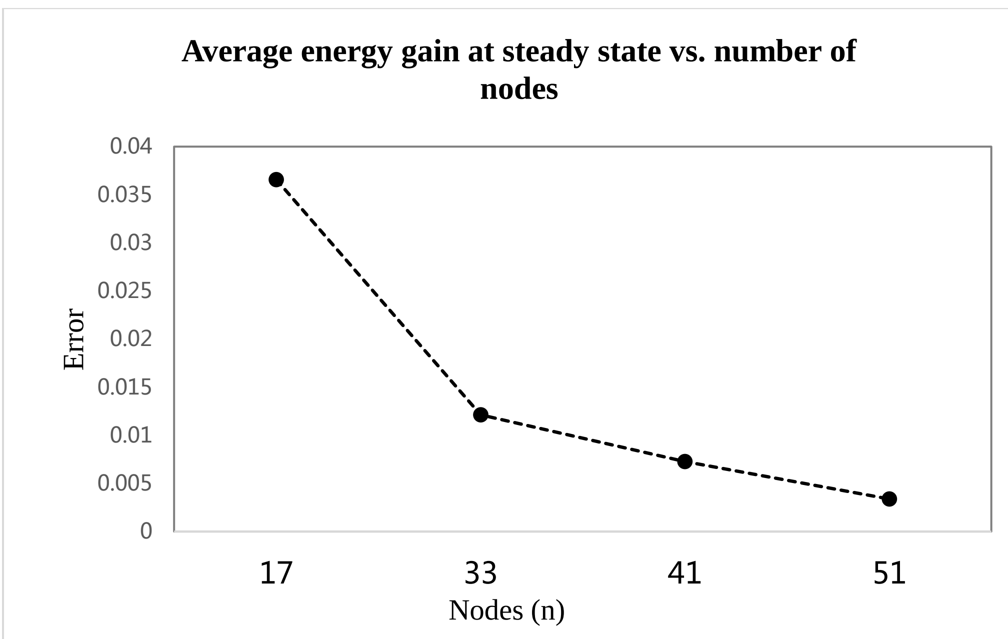

Figure 4.5: Error vs. number of nodes of useful heat

Mass flow rate

The average mass flow rate in the collector for transient calculation of each months is obtained by simulating the model at steady state condition at average radiation of 700 W/m^2 .The simulation is performed for adequate time until steady state condition is attained and the mass flow rate corresponding to the required temperature outlet is selected. Figure 4.6 shows the temperature profiles of the inlet, outlet and middle nodes of the computational domain HTF temperature for the simulation showing steadiness in the solution and Figure 4.7 shows the variation of collector outlet temperature with mass flow rate at steady state condition.

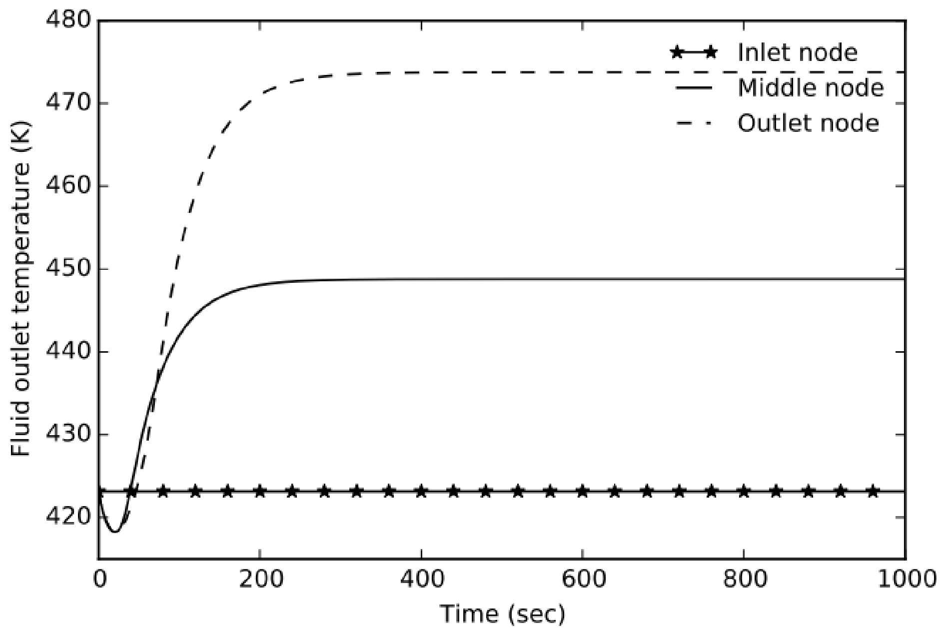

Figure 4.6: Steadiness of the solution

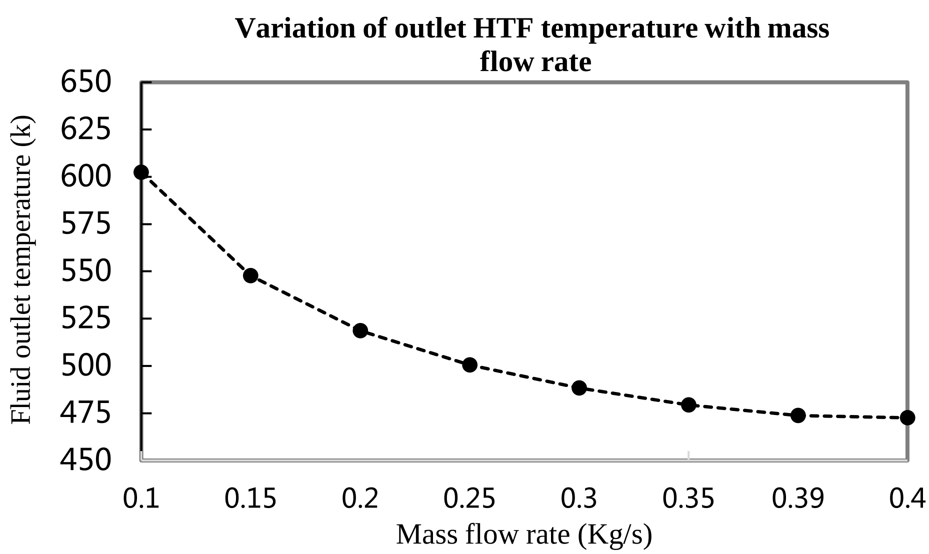

Figure 4.7: Variation of outlet HTF outlet temperature with mass flow rate

As shown in the Figure 4.7, as mass flow rate increases; heat transfer fluid outlet temperature decreases. The mass flow rate of heat transfer fluid is selected for the outlet heat transfer fluid temperature of 200 ^{o}C and guarantee a turbulent flow in the collector. Based on these selection criteria the mass flow rate of heat transfer fluid is equal to 0.39 kg/s.

CHAPTER FIVE

PERFORMANCE ANALYSIS OF CONCRETE SOLAR THERMAL ENERGY STORAGE

5.1 Introduction

A major problem faced by solar thermal heating systems today is the intermittent nature of the solar energy supply. Due to this, thermal energy storage (TES) systems are usually used to eliminate this intermittence by storing solar thermal energy during sunshine hours for later use. Stored thermal energy allows the continued operation of the system after the sun sets or during cloud cover as the supply of heat from the collector field fluctuates. The stored thermal energy can increase the system's efficiency by maintaining the temperature of the HTF flow from the collector field at the desired operating temperature for the load and extending life expectancy of components due to the reduction of thermal transients.

Thermal energy storage can be stored as a change in internal energy of a material as sensible heat, latent heat and thermochemical or combination of these. Among these sensible thermal energy storage is one of the most widely used thermal energy storage in concentrated solar power (CSP) plants and industrial heating systems due to its simple system design and relatively low cost.

5.2 Concrete Thermal Energy Storage

Concrete TES is one of the preferable sensible heat storage systems due to low exergy loss, low cost and easy management of the material .Concrete materials, tested at the Platforma Solar de Almeria (PSA) (Laing et al., 2008), present appropriate characteristics for being adopted as sensible heat storage media. Solid storage systems adopting concrete fall in the category of passive storage systems which are generally "double material": HTF flows in the storage just to charge and discharge a solid material. HTF transfers the heat received from the source of primary energy (the sun) towards the storage module during the charge process and receives energy from the module itself during discharge.

The advantages of concrete storage systems are:

- low costs of storage media,
- high thermal exchange fluxes within the solid (or from this one towards outside) due to the contact between piping and concrete,
- Easy workability of the material,
- Low degradation of heat transfer between exchanger and storage medium.

The cumulated thermal energy within certain mass of the concrete material can be expressed as:

$$Q = \rho . c_p . V . \Delta T \tag{5.1}$$

In Equation 5.1, V is the volume of the concrete material and given by:

$$V = N \frac{\pi}{4} ({d_o}^2 - {d_i}^2) L \tag{5.2}$$

Where

- d_o represents the external radius of hollow concrete material
- d_i the inner radius of hollow concrete material
- L the length of concrete element
- N the number of concrete elements

Where the specific heat has a mean value within the exercise temperature range. As previously reported, for being a material usable in a TES-type application, a low cost is needed as well as a good thermal capacity $\rho . c_p$. An additional fundamental parameter for sensible heat TES is the velocity at which heat can be released or extracted; such a characteristic is function of the thermal diffusivity.

$$\alpha = \frac{k}{\rho c_p} \tag{5.3}$$

Where k is the material thermal conductivity. It is evident that the thermo-physical properties of the concrete materials is of its aggregate materials.

5.3 Modeling of the Storage Unit

A storage unit as the one considered here is composed by a tube register embedded within concrete for allowing fluid flow through it. The pipes, parallel one to the other, have axes (with reference to Figure 5.1 at a distance d_o. For the definition of the physical model, the same conditions have been assumed for each parallel channel, so that the storage module is considered to be composed by sub-units, named elements, put in parallel (Yongfang et al., 2014).

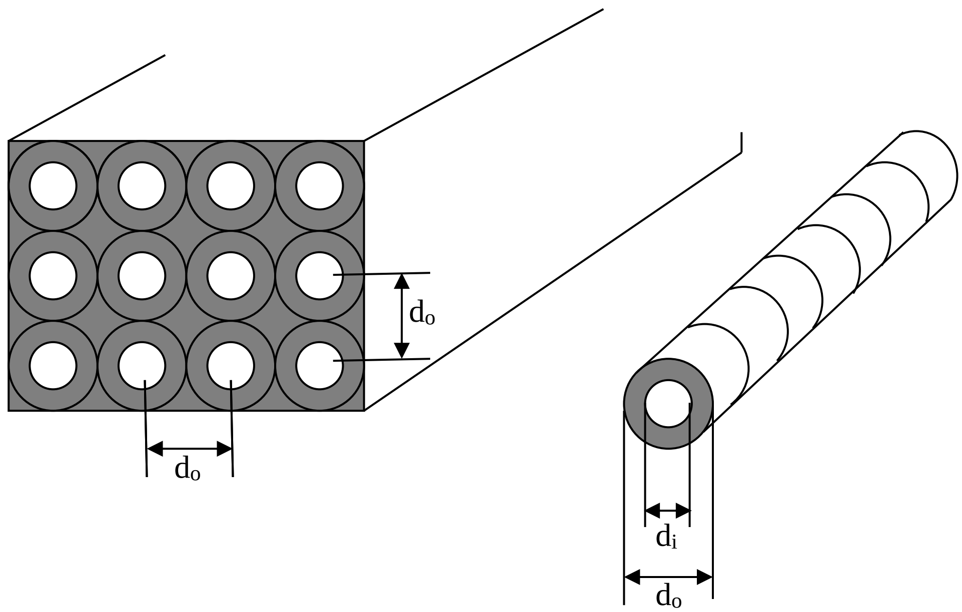

Figure 5.1: Simplified diagram of concrete storage

One element is made by a concrete drilled cylinder with diameter d_o, in contact with a pipe with internal diameter d_i. By having this in mind, the problem of analyzing the storage system moves from the study of the module to that of the single channel for which the initial section is the one of the incoming HTF during charge, whereas the final section is the outgoing one during the same phase. Even if the storage material outside the cylindrical elements is neglected, such a simplification is necessary for implementing an efficient model (Valentina et al., 2014).

Model assumptions

- The storage module has the same thermal behavior as the cylindrical heat storage unit.
- Material and fluid contained in the channel initially at constant temperature on the whole domain, that is conditions of first heating;

- The implemented algorithm for analyzing the discharge phase assumes as initial temperature fields, both for fluid and solid, those calculated at the end of the charge phase;
- The geometry is axis-symmetric.
- Thermal conduction in the axial direction in the fluid is negligible
- Axial heat conduction in the solid can be neglected
- The HTF is assumed to be in direct contact with the solid material. This is due to the small thickness of the tube so that its thermal resistance is negligible;
- There are no heat losses from the storage unit to the surroundings (perfect insulation of the storage)
- concrete is modelled in a simplified manner as an homogeneous, continuous and isotropic material

In addition to that, lumped capacitance method with some modifications, is applicable to the thermal conduction in the solid media in the radial direction; thus, $\frac{\partial T_s}{\partial r} = 0$. The two dimensional transient model for the solid storage unit can then be simplified to a one dimensional model.

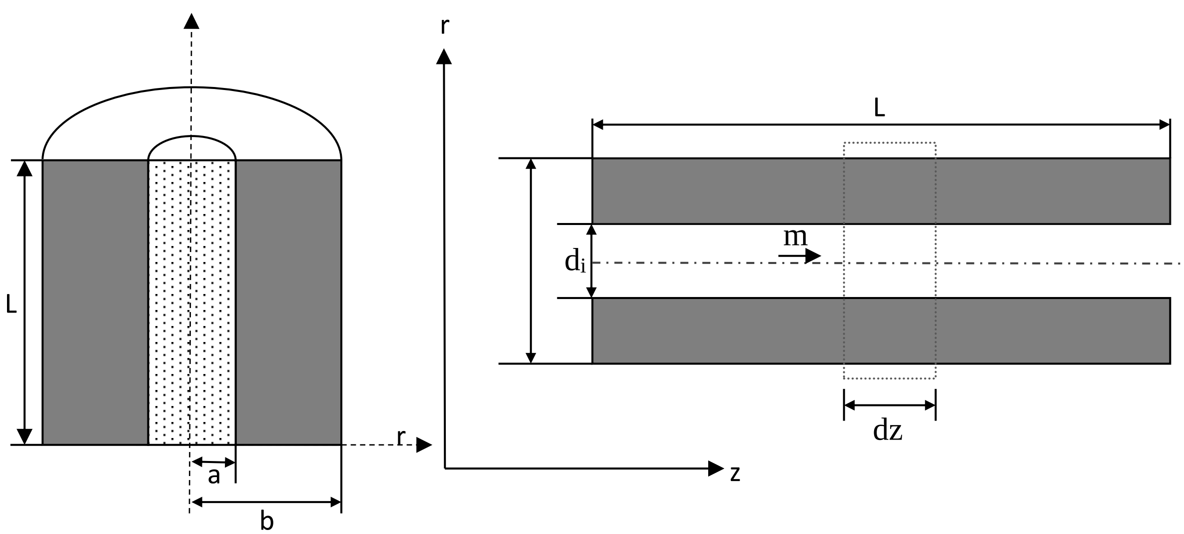

Figure 5.2: Schematic of cylindrical heat storage unit model

Assuming that the fluid mass flow rate, m_{HTF}, in the tubes is constant, the thermal energy balance for the fluid in the differential control volume, dz, as shown in Figure 5.2 is:

$$h_E P dz(T_s - T_{HTF}) + m_{HTF} C_{HTF} T_{HTF,z} = m_{HTF} C_{HTF} T_{HTF,z+\Delta z} + \rho_{HTF} A_{HTF} dz \frac{\partial T_{HTF}}{\partial t} \quad (5.4)$$

Where h_E represents the effective heat transfer coefficient in the tube, πd_i the heat transfer surface perimeter and A_{HTF} is the wetted area in the tube where the fluid flows. i.e. $A_{HTF} = \frac{\pi d_i^2}{4}$.

The average fluid velocity in the cylindrical heat storage unit is given by:

$$U = \frac{m_{HTF}}{\rho_{HTF} A_{HTF}} \tag{5.5}$$

Rearranging Equation 5.4 and substituting Equation 5.5 the fluid energy balance equation becomes (Yongfang et al., 2014):

$$\frac{\partial T_{HTF}}{\partial t} + U \frac{\partial T_{HTF}}{\partial z} = \frac{h_E P}{\rho_{HTF} A_{HTF} C_{HTF}} (T_s - T_{HTF}) \tag{5.6}$$

Similarly, the energy balance for the solid storage material uses the same control volume, can be given by (Yongfang et al., 2014):

$$h_E P dz (T_s - T_{HTF}) = -\rho_s A_s dz C_s \frac{\partial T_s}{\partial t} \tag{5.7}$$

Where A_s is the sectional area of the solid material calculated, $A_s = \pi({d_o}^2 - {d_i}^2)/4$. Rearranging equation 5.7, the energy balance equation can be written as:

$$\frac{\partial T_S}{\partial t} = \frac{h_E P dz}{\rho_S A_S C_S} (T_s - T_{HTF}) \tag{5.8}$$

The effective heat transfer coefficient (h_E) which is developed for modification of lumped capacitance method for large Biot number can be used for the cylindrical concrete heat storage unit. The relationship between the convective coefficient, h_{HTF}, and effective convective coefficient, h_E, in Equation 5.6 is the same as the relationship in Xu et al., (2012), but the effective heat transfer coefficient is derived with the transient terms retained in the fluid energy equation, since the fluid temperature varies during the charging/discharging processes for the solid energy storage system. Therefore, the validity of the effective heat transfer coefficient in equation 5.6 can be extended to the condition of the fluid temperature varying during the charging/discharging processes.

$$\frac{1}{h_E} = \frac{1}{h_{HTF}} + \frac{1}{k_s} . \frac{4ab^4 \ln\left(\frac{b}{a}\right) - 3ab^4 + 4a^3b^2 - a^5}{4(b^2 - a^2)^2} \tag{5.9}$$

Where a and b represents the inner and outer radii of the cylindrical storage unit and k_s is the thermal conductivity of the solid. h_{HTF} is the convection heat transfer coefficient of the HTF inside the tube which is given by:

$$h_{HTF} = Nu\frac{k_{HTF}}{d_i} \tag{5.10}$$

Where:

- k_{HTF} the thermal conductance of the HTF at T_{HTF}
- Nu_{d_i} the Nusselt number based on d_i

The Nusselt number depends on the type of flow through the tube registers. Here a turbulent flow is considered. The Nusselt number can be given by Equation 5.11 and is valid for $0.5 < Pr < 2000$ and $10^4 < Re < 10^6$ (Valentina et al., 2014).

$$Nu = \frac{Re.Pr.f}{1.07+12.7(Pr^{\frac{2}{3}}-1)\sqrt{f}} \tag{5.11}$$

Where the friction coefficient is given by (Valentina et al., 2014):

$$f = 2(2.236ln(Re) - 4.639)^{-2} \tag{5.12}$$

$$Re = \frac{\rho_{HTF}.U.d_i}{\mu_{HTF}} \tag{5.13}$$

5.4 Finite Difference Formulation

A forward finite difference for temporal variation and backward finite difference for spatial variation is used.

Fluid

$$\frac{({T_{HTF,i}}^{t+\Delta t}-{T_{HTF,i}}^{t})}{\Delta t} + U\frac{({T_{HTF,i}}^{t}-{T_{HTF,i-1}}^{t})}{\Delta z} = \frac{h_E P}{\rho_{HTF}A_{HTF}C_{HTF}}(({T_{s,i}}^{t} - {T_{HTF,i}}^{t}) \tag{5.14}$$

After some arrangements

$${T_{HTF,i}}^{t+\Delta t} = (1 - x - y){T_{HTF,i}}^{t} + x{T_{HTF,i-1}}^{t} + y{T_{s,i}}^{t} \tag{5.15}$$

Solid

$$\frac{(T_{s,i}{}^{t+\Delta t} - T_{s,i}{}^{t})}{\Delta t} = -\frac{h_E P}{\rho_S A_S C_S}((T_{s,i}{}^{t} - T_{HTF,i}{}^{t}) \qquad (5.16)$$

After some arrangements

$$T_{s,i}{}^{t+\Delta t} = (1-z)T_{s,i}{}^{t} + zT_{HTF,i}{}^{t} \qquad (5.17)$$

In equation (5.15) and (5.17)

$$x = U\frac{\Delta t}{\Delta z} \qquad (5.18)$$

$$y = \Delta t \frac{h_E P}{\rho_{HTF} A_{HTF} c_{HTF}} \qquad (5.19)$$

$$z = \Delta t \frac{h_E P}{\rho_S A_S C_S} \qquad (5.20)$$

Initial conditions

- The heat transfer fluid and the concrete element are assumed to be at the same initial temperature

Boundary conditions

- The fluid from the solar field is fed in to the storage system as a boundary condition. However, for parametric study a constant heat transfer fluid temperature is taken.

5.5 Characteristics of the Storage Element

Since there are standards for choosing the inner diameter, d_i, and the wall thickness, of the heat transfer tube, the inner diameter and thickness of the tube were selected from d_i=16mm, 18 mm or 20 mm and thickness, d_h=1 mm, 2 mm or 3 mm according to the pressure requirements of the heat transfer fluid. The number of heat transfer tubes, N, can be selected based on the required total energy that should be released from the storage module. The diameter ratio (the ratio of the internal and external diameter of a single element) affects the charging time and the cost of the storage. Table 5.1 shows dimensions and parameters of the concrete TES system.

Table 5.1: Summary of dimensions and parameters of the concrete TES material (Yongfang et al., 2014; Valentina et al., 2014)

Parameters	**Values**
Length of one concrete element (L)	20 m
Diameter of the tube (D_i)	20 mm
Diameter ratio (DR)	5-9
Mass flow rate (m) in a single element	0.05-0.075 (kg/s)
Properties of concrete material	
ρ	3100 (kg/m^3)
c_p	1.18 (kJ/kg.K)
k	2.56 (W/m.K)

5.6 Effect of some Parameters

To study the effect of some important parameters on the storage performance, a simulation is performed by varying the inlet temperature, the mass flow rate and basic geometrical characteristic of the HTF. For parametric study the inlet HTF temperature is assumed to be constant (no variation with time).

5.6.1 Effect of Inlet Temperature

Figure 5.3 shows the effect of inlet temperature of the HTF on the storage for a concrete TES with a diameter ratio of 5. It is evident that as the inlet temperature of the HTF increases the corner temperature of the storage also increases. In all cases the storage temperature increases first and after a specific charging time it becomes constant, attaining the HTF temperature.

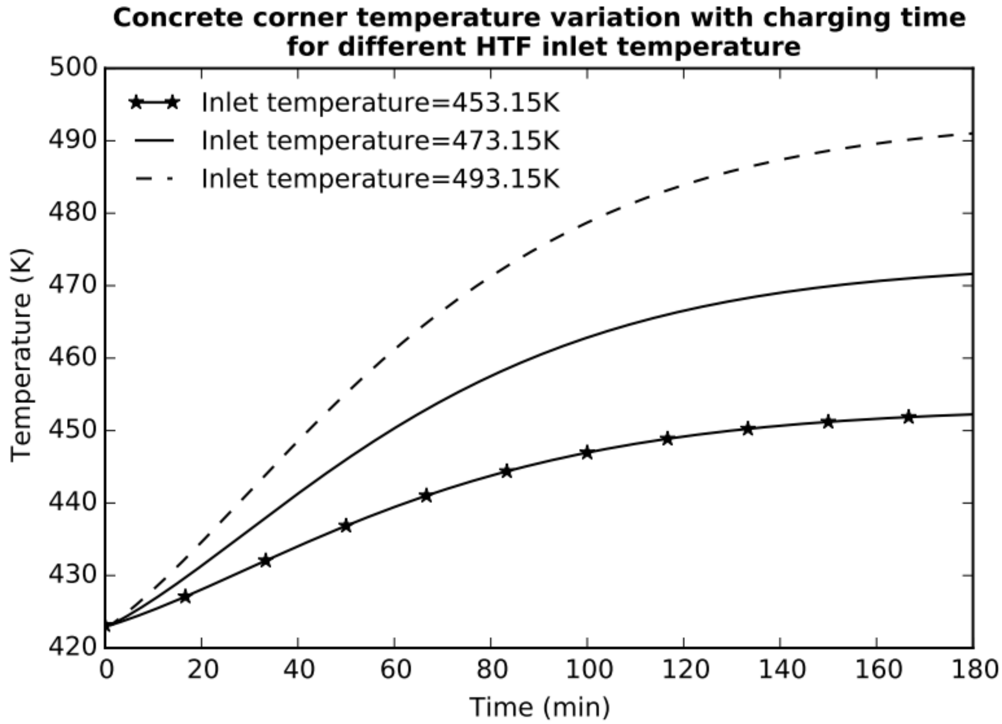

Figure 5.3: Effect of inlet temperature on the concrete TES

5.6.2 Effect of HTF Mass Flow Rate

Based on Figure 5.4, increasing the mass flow rate of the HTF can improve the heat transfer process inside the concrete element. This is due to the fact that as the mass flow rate increases, the heat transfer coefficient inside the tube also increases. In real operational condition, the mass flow rate inside the pipe is restrained by the mass flow rate from the solar field. In this simulation the inlet temperature to the concrete TES element is 473.15 K and the diameter ratio is 5.

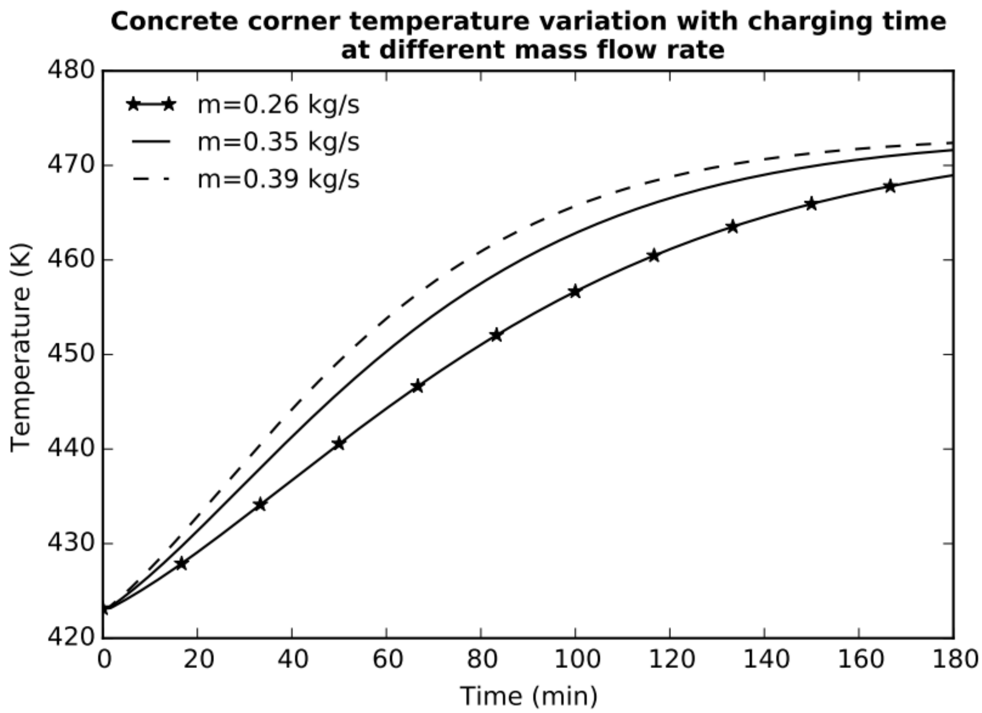

Figure 5.4: Effect of mass flow rate on the concrete TES

5.6.3 Effect of Diameter Ratio

The results in Figure 5.5 show that increasing the diameter ratio results in an increase of charging time of the storage element This is because it takes much larger time for heat to reach the corner of the storage element and reach a certain charging temperature. The simulation is based on an inlet HTF temperature of 473.15.

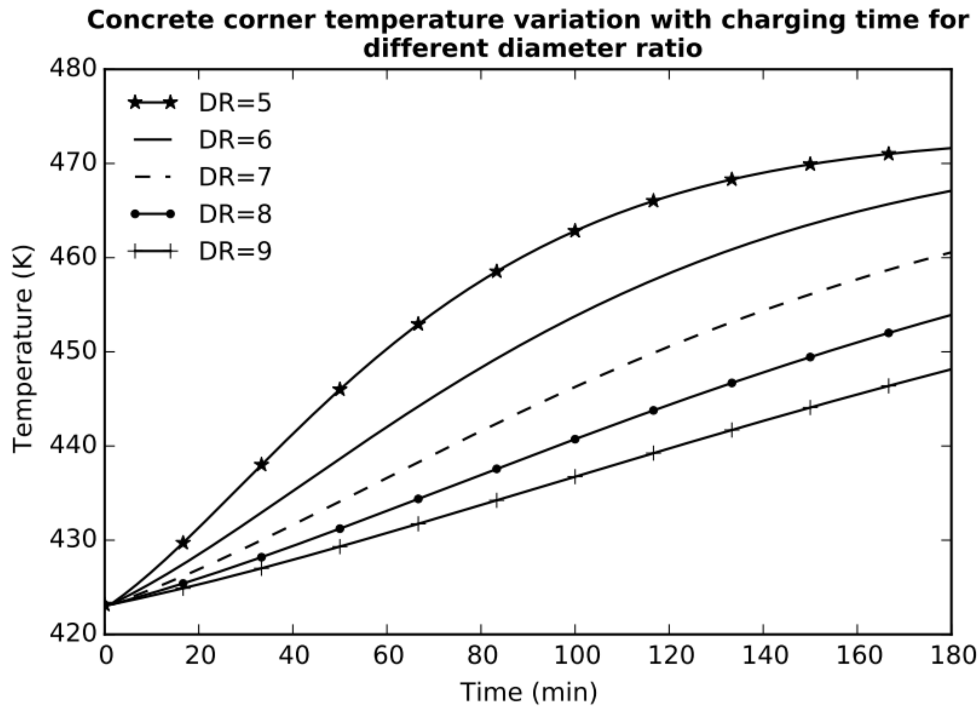

Figure 5.5: Effect of diameter ratio on the concrete storage element

5.7 Validation of the Model

The result of numerical simulation of the concrete TES for charging and discharging processes were validated with a similar work of numerical investigation result of Tamme et al., (2003) for solid TES systems. Figure 5.6 shows the charging and discharging process of the concrete TES for inlet temperature of 200 ^{o}C during charging whereas Figure 5.7 shows the effect of tube diameter on charging and discharging process of the solid storage from Tamme et al., (2003).The two numerical investigation result curves have similar shape. The differences on charging and discharging rate and time is due to difference in geometry and some thermo-physical properties of the solids.

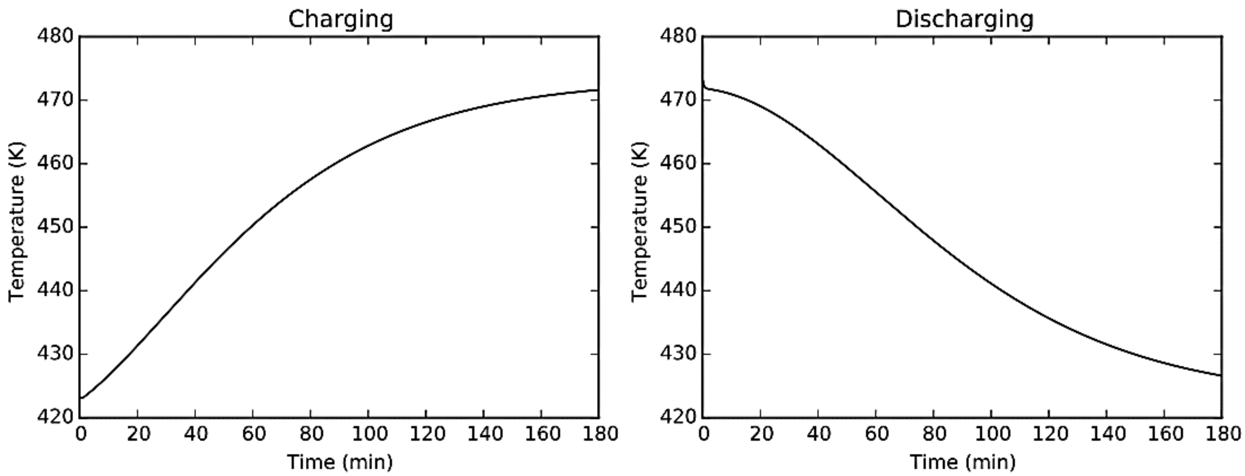

Figure 5.6: Charging and discharging of the concrete TES element

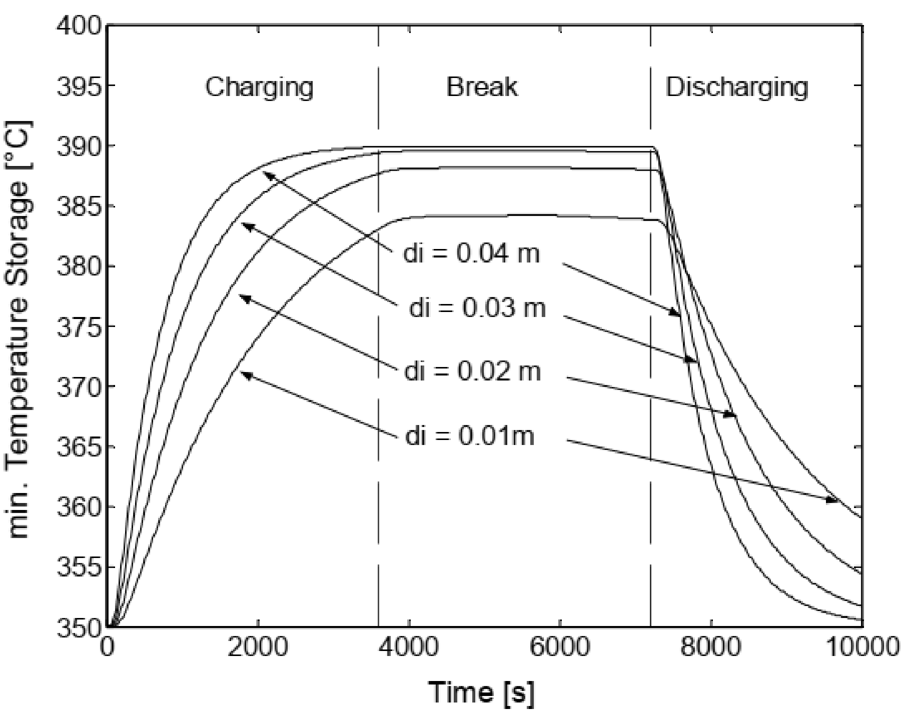

Figure 5.7: Charging and discharging of the concrete TES element with variation of inner diameter of tubes (Tamme et al., 2003)

CHAPTER SIX

RESULT AND DISCUSSION

In this chapter, results obtained from linear Fresnel collector (LFC) and concrete thermal energy storage models is discussed in detail. Validation of the model is done by comparing with numerical experimental results from literatures. LF collector's daily and monthly energetic performance for varying weather conditions is described.

6.1 Heat Transfer Fluid Temperature Variation at the Outlet of LFC

The heat transfer fluid outlet temperature variation throughout the day for different seasons are calculated iteratively using Python software for each second temporal variation of solar radiation incidence on the LF collector pertaining the transient nature of the system and the concrete TES. The heat transfer coefficients and fluid properties are considered temperature dependent. Figure 6.1 shows the temperature variation of heat transfer fluid.

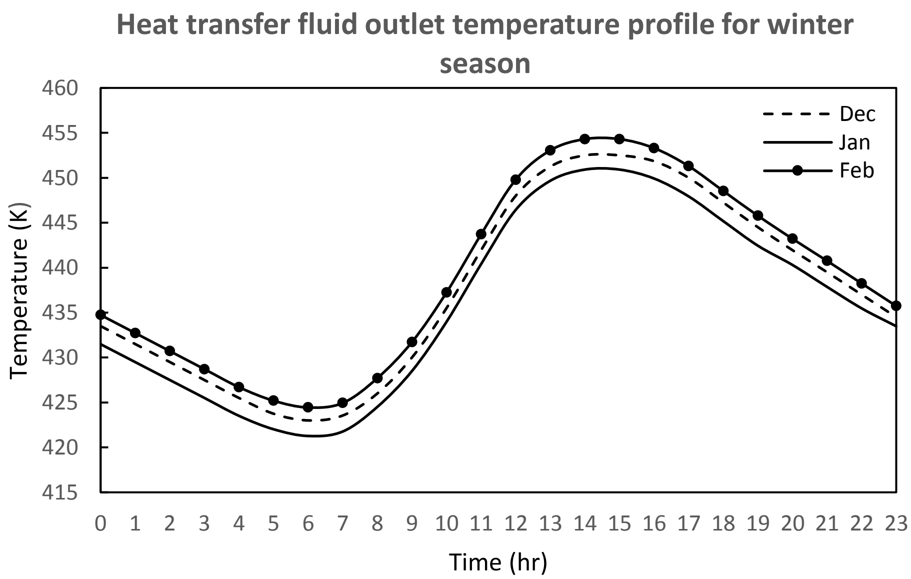

(a)

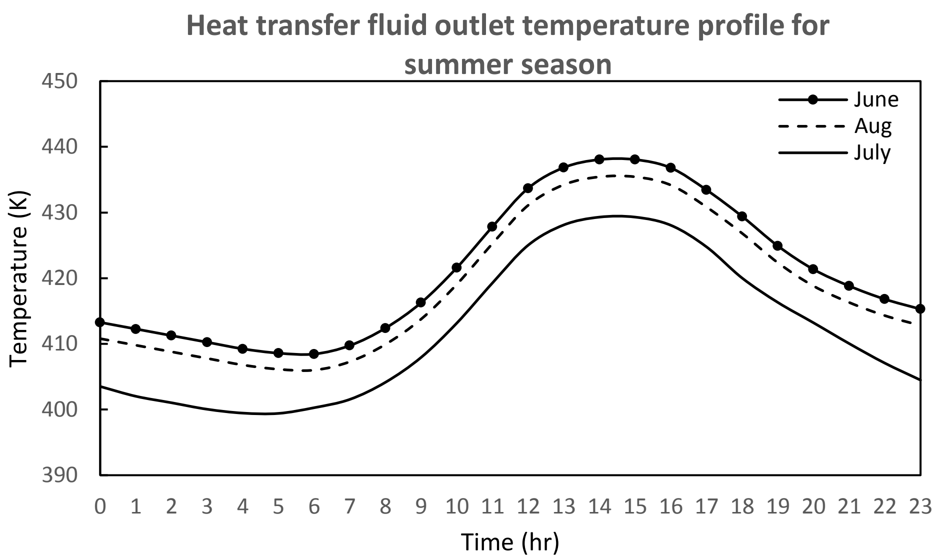
Heat transfer fluid outlet temperature profile for summer season
June
Aug
July
Temperature (K)
Time (hr)
450
440
430
420
410
400
390
0 1 2 3 4 5 6 7 8 9 10 11 12 13 14 15 16 17 18 19 20 21 22 23

(b)

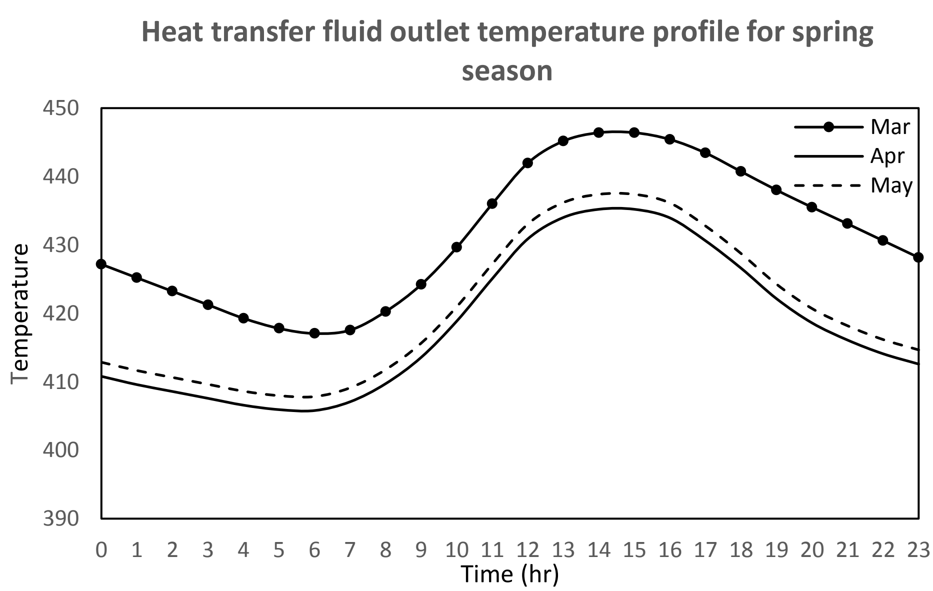
Heat transfer fluid outlet temperature profile for spring season
Mar
Apr
May
Temperature
Time (hr)
450
440
430
420
410
400
390
0 1 2 3 4 5 6 7 8 9 10 11 12 13 14 15 16 17 18 19 20 21 22 23

(c)

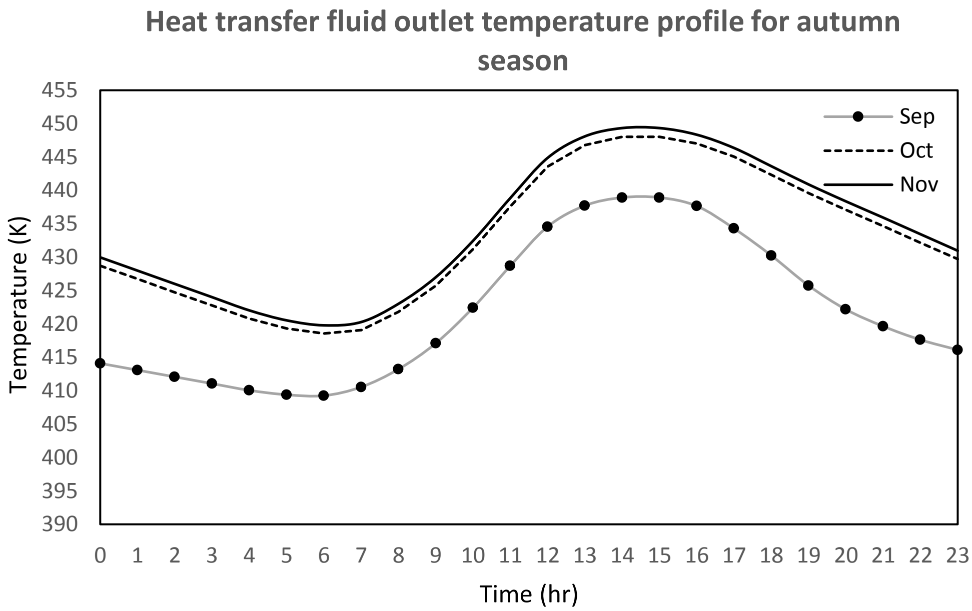

(d)

Figure 6.1: Collector outlet temperatures; winter (a), summer (b), spring (c) and autumn (d) seasons

As shown in the Figure 6.1 at the initial hours of the day, the heat transfer fluid in the linear Fresnel collector-concrete TES system decreases until morning by discharging from the thermal storage during off times for solar irradiation. Then it starts as the sun rises and starts rising the heat transfer fluid temperature until the sun sunsets and discharging from the thermal energy storage continues.

Evidently, winter season experience maximum solar irradiation in the middle of the day (at noon) on a normal surface. These high available solar resources cause higher useful heat transfer to the linear Fresnel collector which raises the heat transfer fluid temperature. The maximum temperatures achieved at the exit of the LFC-concrete TES system for winter, summer, and autumn seasons are 455K, 437K and 450K respectively. It is important to note that there is also a temperature variation in each months of the seasons.

6.2 Variation of Water Temperature

The amount of energy transferred to the circulating water in the drying line of the industry depends on the energy production of the LFC-concrete system.

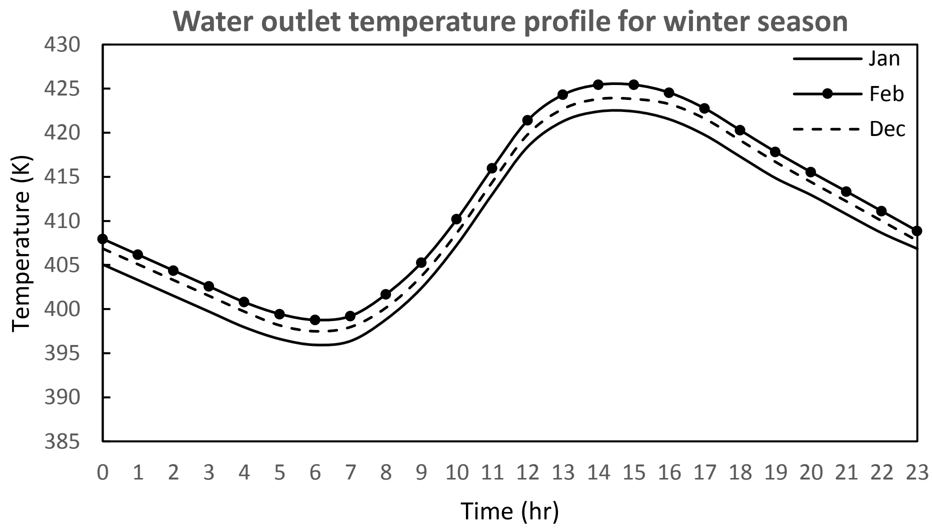

(a)

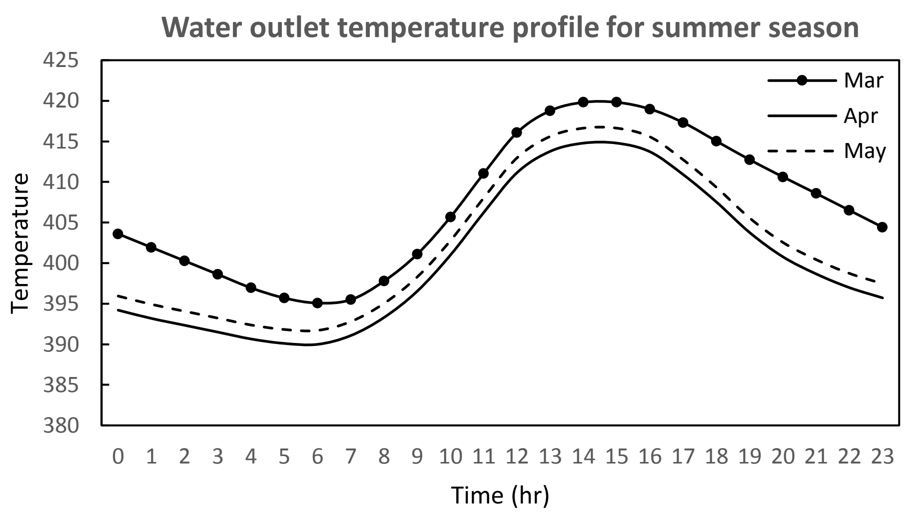

(b)

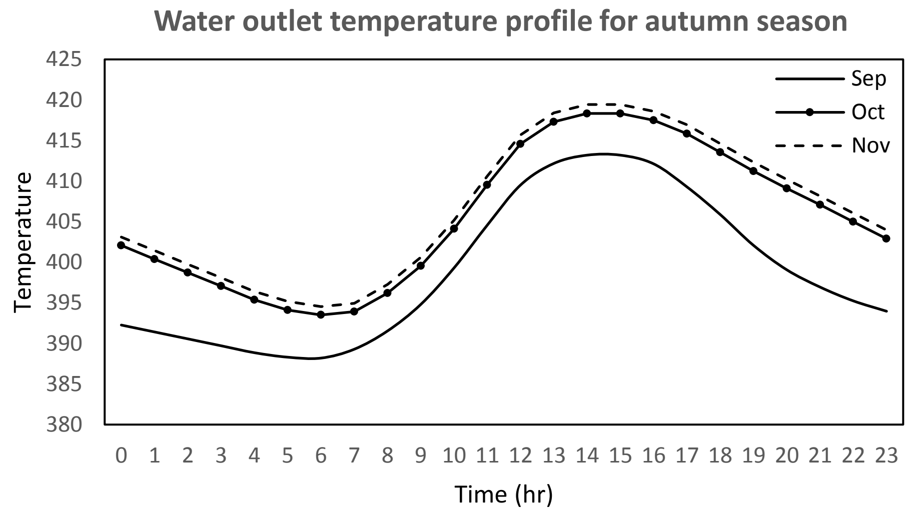

(c)

Figure 6.2: Water outlet temperatures; winter (a), summer (b), and autumn (c) seasons

6.3 Temperature Variation of the Absorber

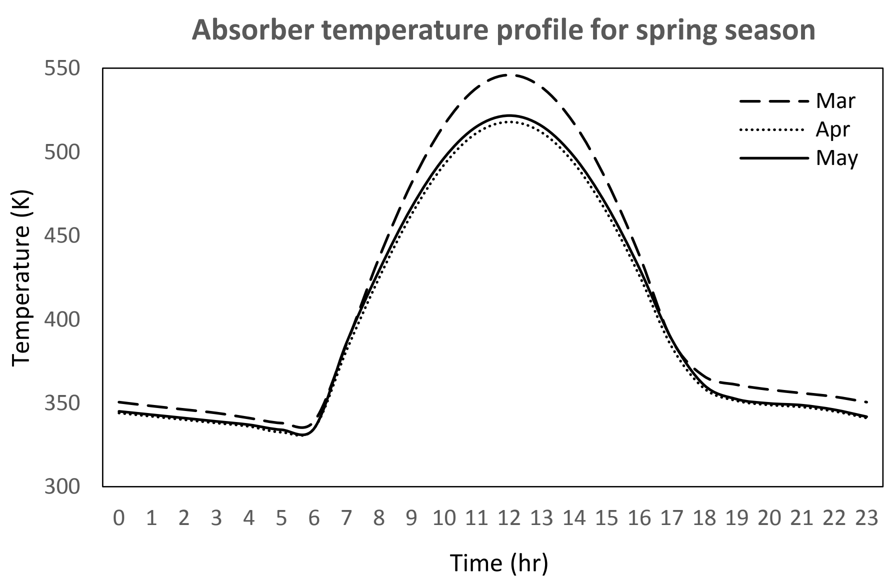

Figure 6.3: Absorber temperature for spring season

6.4 Useful Energy, Sizing and Validation

6.4.1 Instantaneous Useful Energy Collected

The instantaneous useful energy is determined from the inlet and outlet temperatures of LFC, mass flow rate, and specific heat of water. It is calculated based on the outlet temperature of the collector for three modules in series (12m in length). The specific heat capacity of the HTF is considered temperature dependent to get an accurate result.

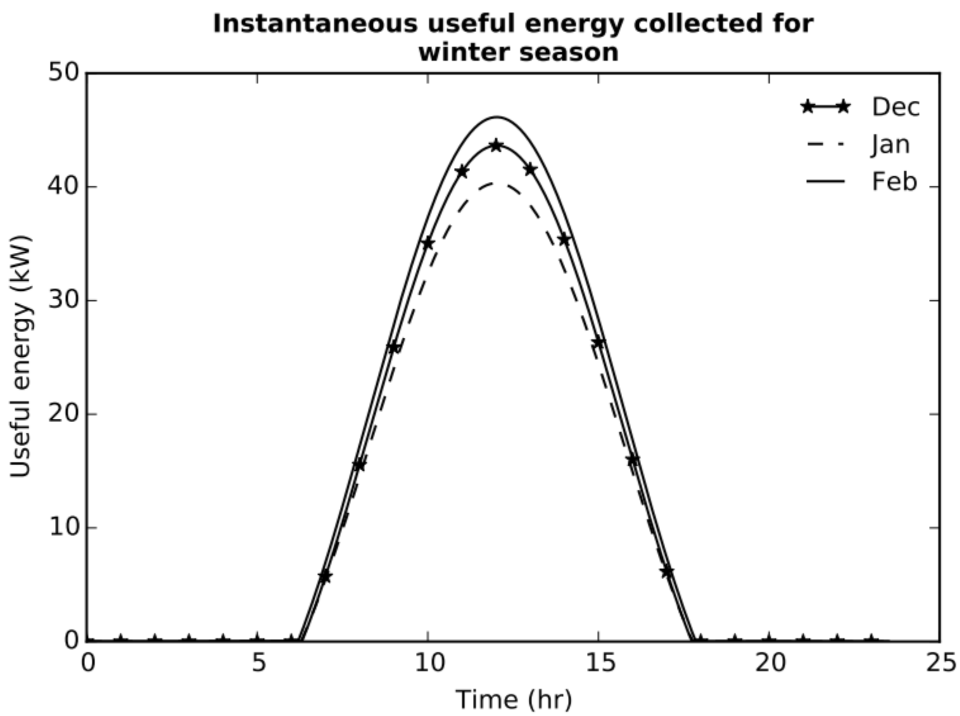

(a)

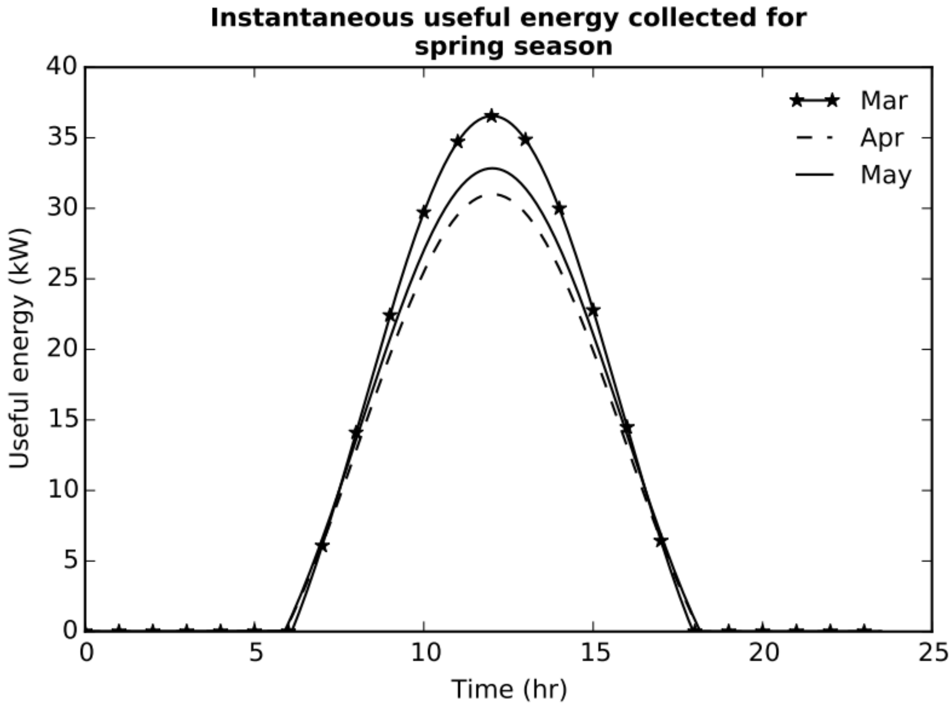

Instantaneous useful energy collected for spring season
Mar
Apr
May
Useful energy (kW)
Time (hr)
0
5
10
15
20
25
30
35
40

(c)

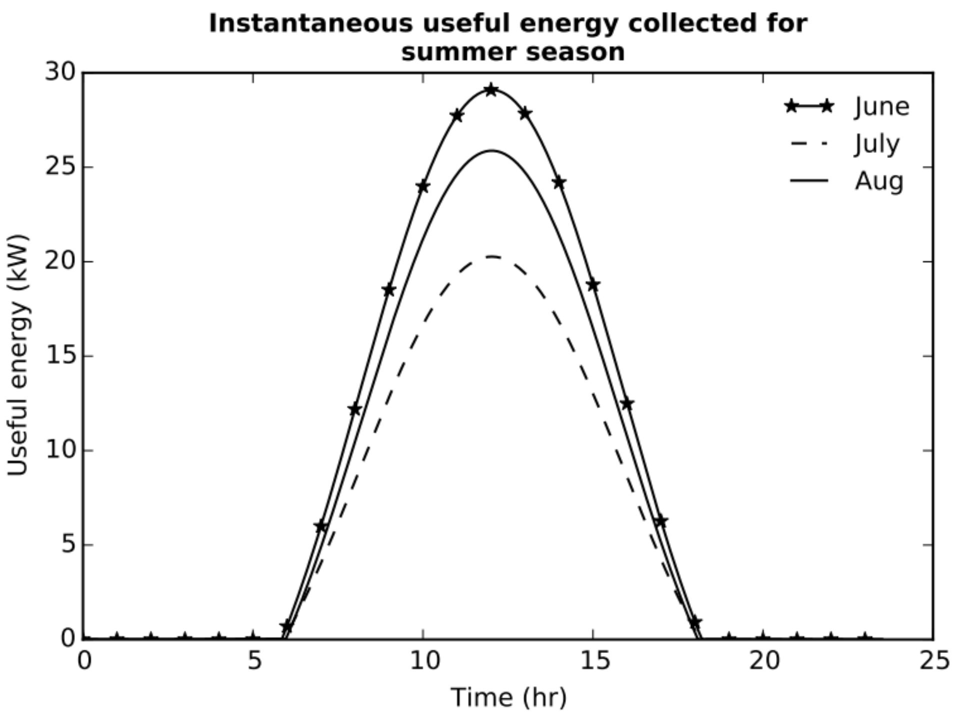

Instantaneous useful energy collected for summer season
June
July
Aug
Useful energy (kW)
Time (hr)
0
5
10
15
20
25
30

(b)

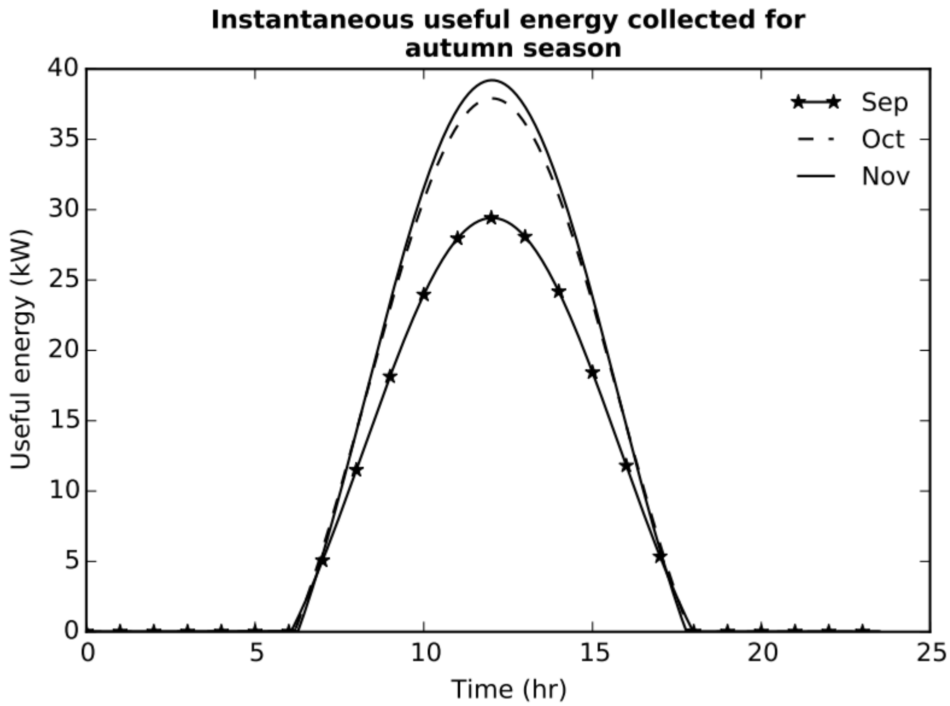

(d)

Figure 6.4: Useful energy; winter (a), spring (b), summer (c), and autumn (d)

Figure 6.3a through Figure 6.3d represent the useful rate of heat transfer to the LFC heat transfer fluid in all seasons of the year. The maximum available useful energy to the LFC vary significantly for the winter and summer seasons due to the difference in solar radiation. The peak instantaneous values for useful energy winter and summer are 46 kW in February and 29 kW in June. July attains a useful energy of 20 kW, least among the representative days and for the shortest time of brighter sunshine hours.

6.4.2 Monthly Average Useful Energy

Useful energy results depicted in Section 6.4.1 vary throughout the day depending on the position of the sun. Due to this, it is important to calculate the average useful energy for sizing of the required collector for the system.

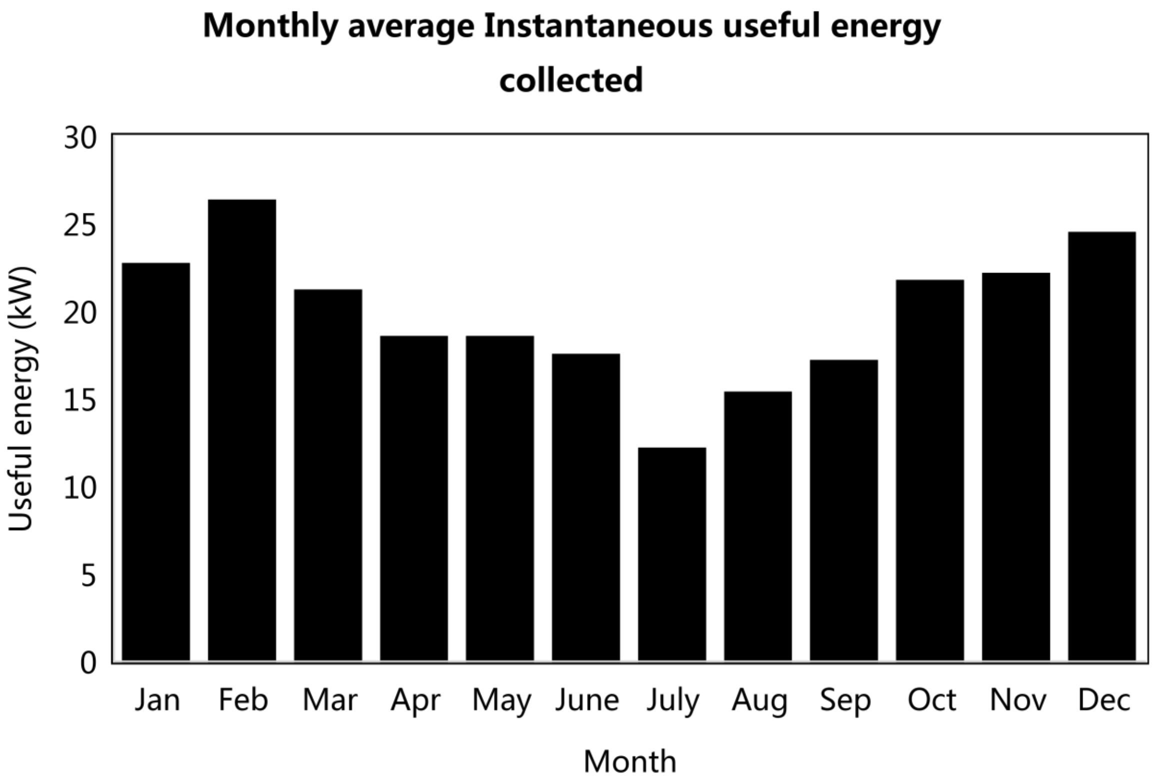

Figure 6.5: Average monthly useful heat gain of the LFC

Base on the result as shown in Figure 6.4 the average monthly instantaneous energy collected by the LFC varies from 26 kW in February to 12 kW in June. This is due to the significant difference in available solar radiation in this months.

6.4.3 Validation of the Collector Model

The collector model is validated by comparing the results of useful power of this study with the works of Beltagy et al., (2017) in which theoretical and experimental performance analysis of LFC is studied. Both studies shows similar curves of useful power with the difference accounting for the variation of solar resource models and experiment.

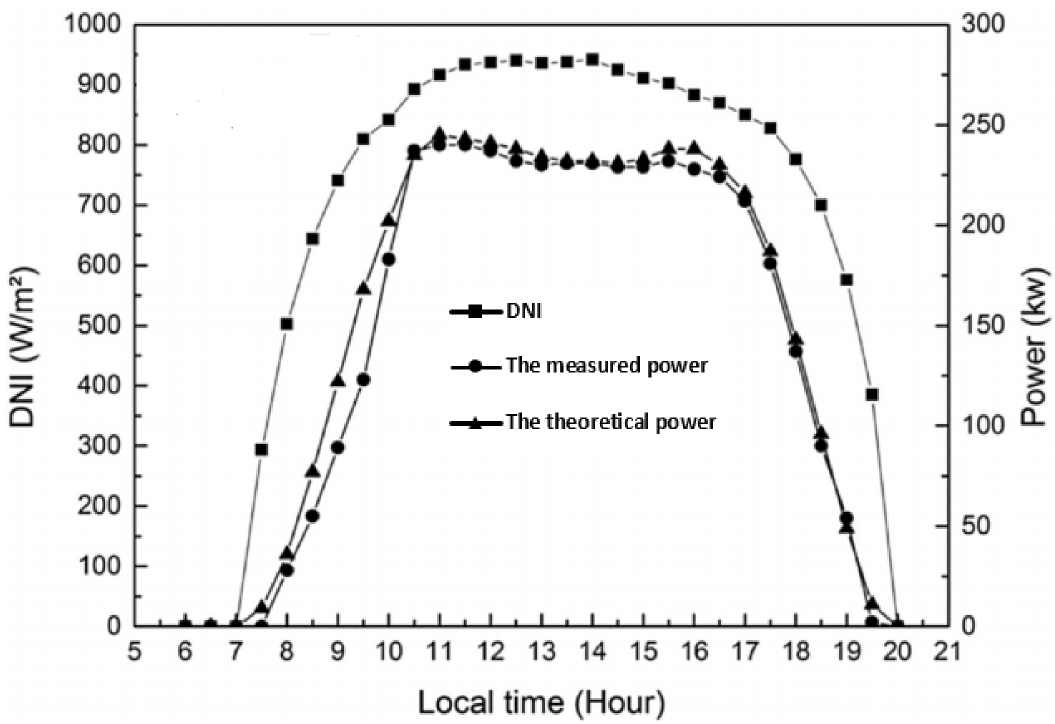

Figure 6.6: Hourly power output of a LFC (Beltagy et al., 2017)

6.4.4 System Sizing

The average useful energy gained from the LFC is variable for each months of the year. So the sizing of the LFC system is done on the basis of average annual daily useful energy collected from three collectors in series (12 m in length). The area of the LFC is calculated to produce an average useful energy of 19.7 kW. In order to calculate the desired number of LFC, specifications in (Table 3.1) are considered as constant whereas length of the LFC is the only variable. From the design conditions, the number of collectors required is calculated from Equation 6.1.

$$number\ of\ collectors = \frac{Desired\ power}{Annual\ average\ useful\ energy} \tag{6.1}$$

Which comes out to be 86 collectors. Considering oversizing the collector with accounting six hours of thermal energy storage a total amount of 120 modules with an aperture area of 2838 m^2 and a total length of 480 m. Assuming a packing density of 0.67, which is the ratio of aperture area and ground area, a ground area of 4236 m^2 is needed to fulfil the daily energy requirement of the company.

6.5 Collector Loop Pressure Drop

The pressure drop inside the absorber loop is calculate based on formulas in Section 3.6. Figure 6.7 shows the trend of pressure loss across the LFC at different mass flow rates, which logical replicates the pressure drop relation, as the velocity increases so as the pressure drop. It is important to note that the mass flow rate is for three collector modules in series (collector length of 12 m) whereas the total pressure drop is found by multiplying by number of paired modules.

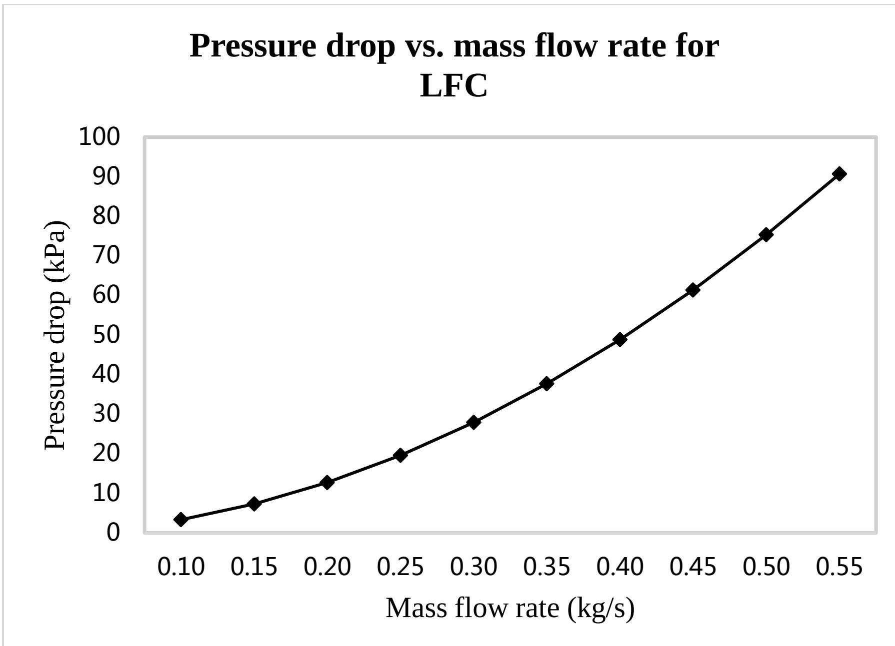

Figure 6.7: Pressure drop vs. mass flow rate on the LFC loop

6.6 Efficiency of the LFC System

The basic efficiency terms that are important to describe the performance of the LFC system are optical and thermal efficiencies.

6.6.1 Optical Efficiency

The optical efficiency of the LFC system depends on the Incident Angle Modifier which varies throughout the day as a function of incident angle. However, to simplify the analysis a daily mean IAM is used. Shown in Figure 6.8, the optical efficiency of the LF collector varies from 0.62 in April to 0.576 in May.

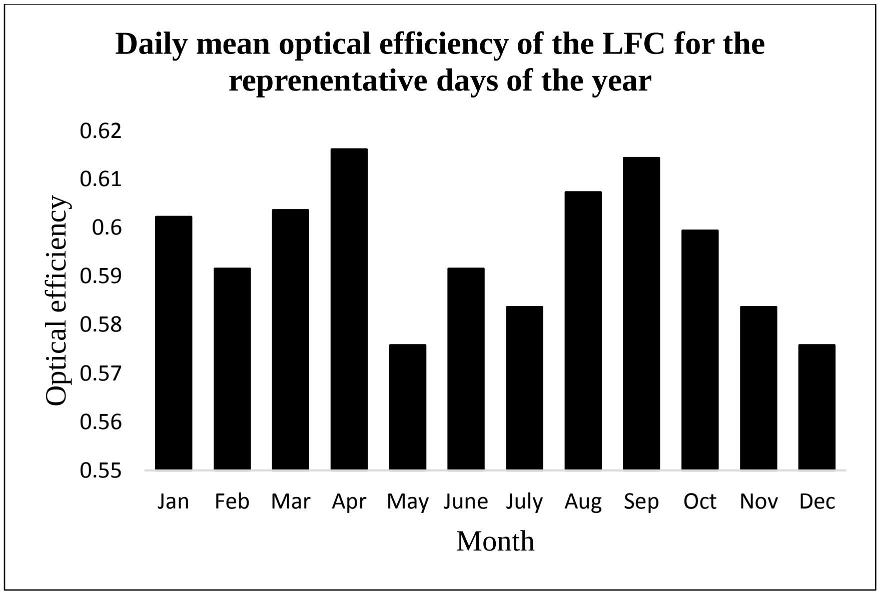

Figure 6.8: Daily mean optical efficiency of the LFC

6.6.2 Instantaneous Thermal Efficiency of the Collector

The instantaneous thermal efficiency of the LFC, η_{th}, is calculated based on the heat gain, solar intensity and aperture area of the collector.

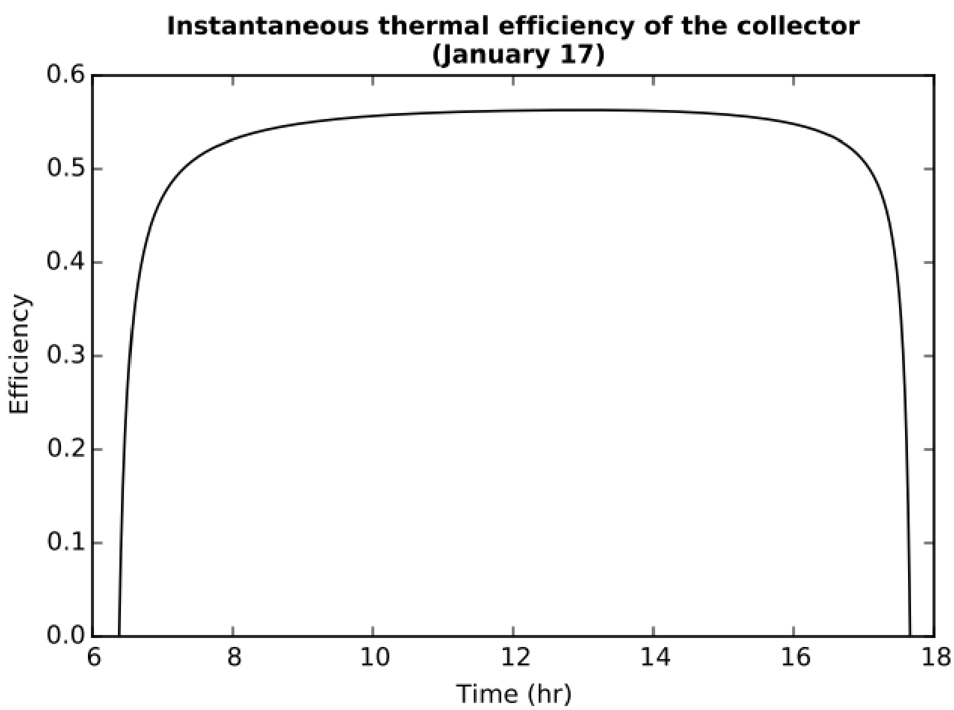

Figure 6.9: Instantaneous thermal efficiency of the LFC for January 17

It can be noticed that the thermal efficiency of the collector is relatively uniform throughout the day except during the sunset and sunrise hours. This is due to the fact that thermal loss to the environment is much lower due to evacuation. During sunset and sun rise, thermal efficiency is relatively lower due to the storing characteristics of receiver elements. In addition to that, the thermal efficiency may be further reduced if tracking errors, degradation of absorptivity etc. are considered.

6.7 Charging of Concrete Thermal Energy Storage

The charging and discharging process of the concrete TES system for a constant inlet temperature of HTF and some parametric studies have been already discussed in chapter five. For real operational case, the charging process of concrete storage is simulated based on the flow rate and temperature of the heat transfer fluid from the solar field for representative days of the year. Figure 6.9 shows the temperature variation of the storage for the first month of the year. The storage increases its temperature and attains its peak value sometime after solar noon. This is due to the temperature of HTF vary throughout the day.

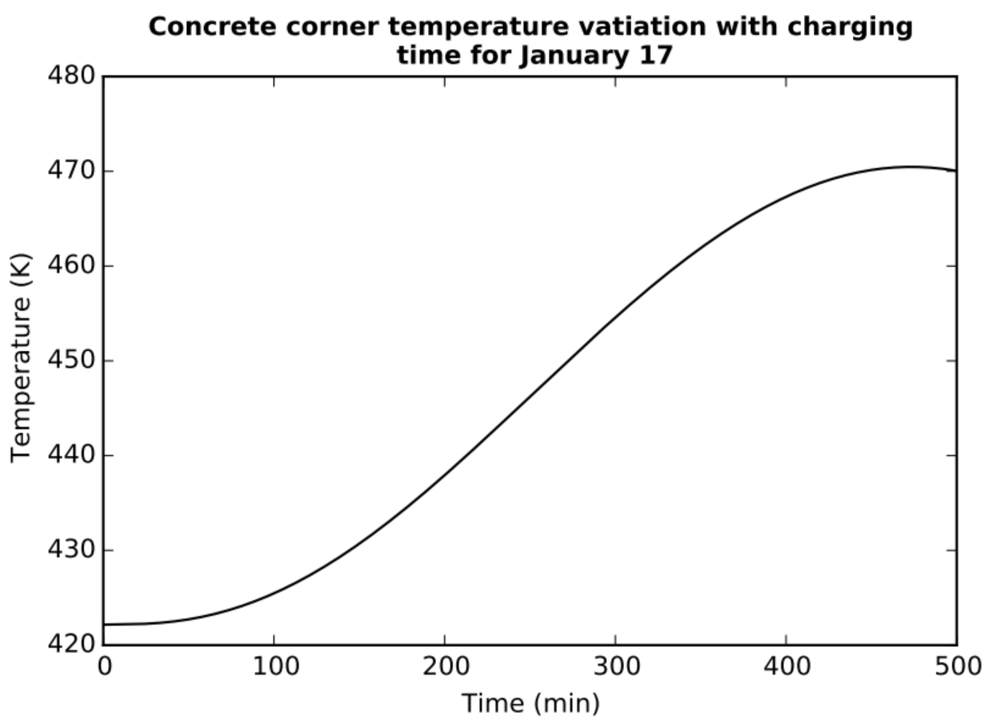

Figure 6.10: Concrete corner temperature variation with charging time for January 17

The concrete TES thermal model developed is for a single element from which an energy capacity for one element is evaluated. A complete storage is build up by multiplying this capacity until the required capacity is reached. This number of storage elements will then be operated in parallel. Figure 6.11 shows the rate of thermal energy stored on a single storage element during charging process. It is important to note that if during the charging period not enough energy is available to use the full capacity of the storage systems, only a reduced number of flow channels should be used. This needs modularization of the system with a control strategy, not included in this study.

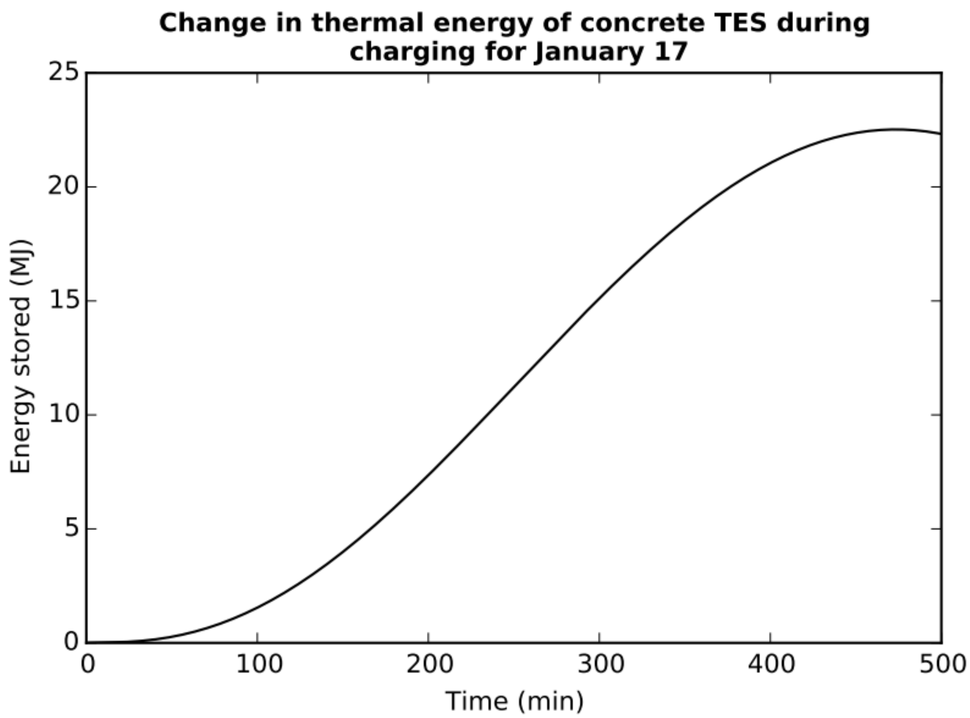

Figure 6.11: Change in thermal energy of concrete TES during charging for January 17

A tube with a diameter of 20 mm is used as heat exchanger between the concrete material and the HTF. Based on the analysis 98 m^3 of concrete material is required to store the energy consumption of the industry for 6 hours. A total number of the studied concrete element required to store the desired quantity of heat were 258.

CHAPTER SEVEN

CONCLUSIONS AND RECOMMENDATIONS

7.1 Conclusions

In this study, performance analysis of linear Fresnel collector for industrial heat generation is performed. The heat requirement of the company was found by analyzing the daily fuel consumption data. The company consumes around 740,918 liters of diesel fuel per year, costing it approximately 12 million of Ethiopian birr.

A detailed numerical modeling of Linear Fresnel collector and concrete thermal energy storage by taking into account the inherent transient nature is carried out, which helped in coping up with the variable solar input. First, the collector model was presented as coupled partial differential equations based on energy balance on its components. For the implementation in computer, the sets of partial differential equations were obtained and through discretization of the governing energy equations using finite element method linear algebraic equations were obtained. A program in python was developed for the analysis including solar resource, collector and concrete TES model. The models were validated through a comparison with numerical and experimental studies in literature.

The useful energy absorbed by the LFCs through the course of the day highly depends upon several factors such as temperature across the LFC pipes, ambient temperature, mass flow rates and solar radiation. The solar radiation varies significantly through the course of the day which demands a dynamic model study the heat transfer phenomenon. Solar resources (Direct normal irradiance) for Adama city is evaluated based on data found from National Metrological Agency and used as an input parameter for the simulations.

Based on the simulation results, the mass flow rate is the main parameter to control the output temperature of the system. The temperature output of the system has reached 455K at a mass flow rate of 0.39 kg/s. The instantaneous thermal efficiency of the collector can reach 55%. It was found that an aperture area of 2838 m^2 which corresponds to 120 modules of the selected LFC is required to fulfil the daily process heating energy demand of the factory. In addition, it was found that 258 elements of the studied concrete TES (total of 98 m^3) is required to store 6 hours of thermal energy based on the requirement of the factory. The storage can serve as a thermal battery for smoothing the output from the collector field and buffer storage in cloudy hours of the day.

7.2 Recommendations and Future Work

- A detailed study of optical characteristics of the collector using ray tracing software can increase the accuracy of the model. In addition, the effect of secondary concentrator on the thermal performance of the system can be studied using this method.
- In this study, a uniform flux distribution is considered around the circumference of the receiver tube. Similar study can be performed accounting the non-uniformity of flux on the receiver tube to get a more accurate result. Usually, this method requires a comprehensive three dimensional modeling.
- For the system to work with uniform temperature a storage with higher energy density like phase changing materials can be studied.
- Studying the concrete TES system with consideration of thermal loss to the environment can increase the accuracy of the model.
- Outlet temperature control strategy for the LFC and concrete TES systems can be studied.
- In addition to technical assessment, an economic analysis can provide more insight into feasibility of LFC for Industrial process heat generation.

REFERENCES

Askari I., & Ameri M. (2017). The application of Linear Fresnel and Parabolic Trough solar fields as thermal source to produce electricity and fresh water, *Desalination*, 415, 90–103.

Baharoon D.A., Rahman H.A., Wan Omar W.Z., & Fadhl S.O. (2015). Historical development of concentrating solar power technologies to generate clean electricity efficiently – a review. *Renew. Sustain. Energy*, 41, 996–1027.

Bai F., Wang Z., & Liye X. (2008). Numerical simulation of flow and heat transfer process of solid media thermal energy storage Unit. In Proceedings of ISES World Congress 2007 (Vol. I – Vol. V). Springer, Berlin, Heidelberg

Bastian S. (2016). Classification of industrial heat consumers for integration of solar heat. *Energy Procedia*, 91, 650-660.

Bellos E., & Tzivanidis C. (2018). Assessment of linear solar concentrating technologies for Greek climate, *Energy Convers. Manage*, 171, 1502–1513.

Bellos E., & Tzivanidis C. (2019). Alternative designs of parabolic trough solar collectors. *Prog. Energy Combust*, 71, 81–117.

Beltagy H., Semmar D., Lehaut C., & Said N. (2016). Theoretical and experimental performance analysis of a Fresnel type solar concentrator, *Renewable Energy*, 101, 782-793.

Ben X., Pei-Wen L., & Cho Lik C. (2012). Extending the validity of lumped capacitance method for large Biot number in thermal storage application. *Solar Energy*, 86, 1709–1724.

Benyakhlef S., AlMers A., Merroun O., Bouatem A., Boutammachte N., El Alj S., & Erregueragu Z. (2016). Impact of heliostat curvature on optical performance of Linear Fresnel solar concentrators. *Renew. Energy*, 89, 463–474.

Christian Z., & Oliver I. (2012). Solar process heat for sustainable automobile manufacturing *Energy Procedia*, 30, 775 – 782.

Duffie, J.A., & Beckman, W.A. (2013). *Solar engineering of thermal processes*. New York: John Wiley & Sons, Inc.

Evangelos B. (2018). Progress in the design and the applications of linear Fresnel reflectors: A critical review. *Energy Reviews*, 91, 193-204.

Evangelos B., & Christos T. (2018). Development of analytical expressions for the Incident Angle Modifiers of a linear Fresnel reflector. *Applied Thermal Engineering*, 133, 70-80.

Farid M.M., Khudhair.A.M, Ali.S & Razack.K (2004). A review on phase change energy storage : materials and applications. 45, 1597–615.

Forristall R. (2008). Heat transfer analysis and modeling of a parabolic tough solar receiver implemented in engineering equation solver. *National Renewable Energy Laboratory*.

Gunther M. (2017). Linear Fresnel Technology, enerMENADLR, www.energyscience.org, last visited on June 2019.

Haagen M., Zahler C., Zimmermann E., & Al-najami M. (2015). Solar process steam for pharmaceutical industry in Jordan. *Energy Procedia*, 70, 621–625.

He J., Qiu Z., Li Q., & Zhang Y. (2012). Optical design of linear Fresnel reflector solar concentrators. *Energy Procedia*, 14, 1960–1966.

Heimsath A., Cuevas F., Hofer A., Nitz P., & Platzer W. J. (2013). Linear Fresnel collector receiver: Heat loss and temperatures. *Energy Procedia*, 49, 386–397.

Hofer A., Cuevas F., Heimsath A., Nitz P., Platzer W. J., & Scholl S. (2015). Extended heat loss and temperature analysis of three linear Fresnel receiver designs. *Energy Procedia*, 69, 424–433.

Huang F., Li L., & Huang W. (2014). Optical performance of an azimuth tracking linear Fresnel solar concentrator. *Sol. Energy*, 108, 1–12.

Incropera F.P., & De Witt D.P. (2011). *Fundamentals of Heat and Mass Transfe*r. New York : John Wiley & Sons,Inc.

Industrial Solar, http://www.industrial-solar.de/content/en, last visited on June 28, 2019

Jian Y., Bai F., Falcoz Q., & Wang Z. (2014). Control strategy of the module concrete thermal energy storage for parabolic trough power plants. International Conference on Concentrating Solar Power and Chemical Energy Systems, *Energy Procedia*, 69, 891–899.

Kalagirou S. (2009). *Solar Energy Engineering Processes and Systems*. First edition. Massachusetts: Elsevier.

Kalaiselvam. S & Parameshwaran. M (2014). Thermal energy storage technologies for sustainability: systems design, assessment and applications. 1st edition, Academic express.

Laing D., Lehmann D., & Bahl C. (2008). Concrete storage for solar thermal power plants and industrial process heat, in: 3rd International Renewable Energy Storage Conference, Berlin 103 , 303–315

Lillo, E. Pérez & S. Moreno (2017). Process heat generation potential from solar concentration technologies in Latin America: The case of argentina.

Mohamed H. Ahmed & Amr M. A. Amin (2016). Thermal analysis of the performance of linear Fresnel solar concentrator. *Journal of Clean Energy Technologies*, 5(4).

Mokhtar G., Boussad B., & Noureddine S. (2016). A linear Fresnel reflector as a solar system for heating water: Theoretical and experimental study. *Case Stud. Therm. Eng.*, 8, 176–186.

Mokhtar G., Boussad B., Zafar S., and Evangelos B. (2019). A numerical simulation of a linear Fresnel solar reflector directed to produce steam for the power plant. *Journal of Cleaner Production*, 231, 494-508.

Montes M., Abbas R., Muñoz .M, Muñoz-Antón .J, & Martínez-Val J. (2017). Advances in the linear Fresnel single-tube receivers: hybrid loops with non-evacuated and evacuated receivers. *Energy Convers. Manage*, 49, 318–333.

Negi, S. Mathur, & T. Kandpal (1989). Optical and thermal performance evaluation of a linear Fresnel reflector solar concentrator. *Solar Wind Technol.*, 6(5), 589-593.

Pino F. J., Caro R., Rosa F., & Guerra J. (2013). Experimental validation of an optical and thermal model of a linear Fresnel collector system. *Applied Thermal Engineering*, 2(50), 1463–1471.

Pye, J.D., Morrison, G.L., & Behnia,M. (2006). Pressure drops for direct steam generation in line-focus solar thermal systems: proceedings of ANZSES, Canberra, Australia

Qiu Y., He L., Wu M., & Zheng ZJ (2016). A comprehensive model for optical and thermal characterization of a linear Fresnel solar reflector with a trapezoidal cavity receiver. *Renew Energy*, 97, 129-144.

Reddy K. & Kumar K. (2014). Estimation of convective and radiative heat losses from an inverted trapezoidal cavity receiver of solar linear Fresnel reflector system. *Int. J. Therm. Sci.*, vol. 1(80), 48–57.

Rungrudee B., Sukrudee S. (2016). Energy and exergy analysis of thermal energy storage prototype by using concrete material in Thailand. *Applied Mechanics and Materials*. 839, 14-22

Samuel T. & Getachew B. (2014). Resource assessment and optimization study of efficient type hybrid power system for electrification of rural district in Ethiopia, *International Journal of Energy and Power* Engineering, V3.

Sen, P. K., K. Ashutosh, K. Bhuwanesh, Z. Engineer, S. Hegde, P. V. Sen, and P. Davies (2013).Linear Fresnel Mirror Solar Concentrator with tracking. Procedia Eng., vol. 56, pp. 613–618.

Sharma V, Nayak J., Kedare S. (2013). Effect of shading and blocking on available energy at the receiver of a linear Fresnel reflector field. International Conference on Solar Heating and Cooling for Buildings and Industry. September 23-25, Freiburg, Germany

Tzivanidis C., Bellos E., & Papadopoulos A. (2018). Optical and thermal analysis of a linear Fresnel reflector operating with thermal oil, molten salt and liquid sodium. *Appl. Therm. Eng*. 123, 70–80.

U.S. Energy Information Administration (EIA) (2017). Annual energy outlook, https:// www.eia.gov/outlooks/aeo/, last visited on May 2019

Valentina A., Carmelo E., Giuseppe M., Adio M., Rosa D., Fabrizio G., Domenico M., & Marco L. (2014). Thermal storage of sensible heat using concrete modules in solar power plants. *Solar Energy*, 103, 303–315.

Wagner M. (2012), Results and comparison from the SAM linear Fresnel technology performance model. NREL/CP-5500-54758.

Xu G., Song G., Zhu X., Gao W., Li H., & Quan Y. (2015). Performance evaluation of a direct vapor generation supercritical ORC system driven by linear Fresnel reflector solar concentrator. *Appl. Therm.Eng.*, 80, 196–204.

Yongfang J., Fengwu B., Quentin F., Chao X., Yan W., & Zhifeng W. (2014). Thermal analysis and design of solid energy storage systems using a modified lumped capacitance method. *Applied Thermal Engineering*.

Zhu G. (2013). Development of an analytical optical method for linear Fresnel collectors. *Sol. Energy*, 94, 240–252.

Zhu G., Wendelin T., Wagner M., & Kutscher C. (2014). History, current state, and future of linear Fresnel concentrating solar collectors. *Sol. Energy*, 103, 639–652.

APPENDIX

ANNEX A: Material Properties

<u>Properties of absorber tube (Stainless steel cermet coated) (@150 ºC)</u>

Specific heat = 435 (J/kgK)

Thermal conductivity = 54 (W/mK)

Density (ρ) = 8073 (kg/m^3)

Emittance (ε) = 0.091

<u>Properties of the glass cover (Low iron glass) (@30ºC)</u>

Specific heat = 500 (J/kgK)

Thermal conductivity = 1.05 (W/mK)

Density (ρ) = 2000 (kg/m^3)

Emittance (ε) = 0.4

<u>Properties of the air @ 20 ºC</u>

Specific heat (C_p) = 1005 (J/kgK)

Density (ρ) = 1.205 (kg/m^3)

Viscosity (μ) = 18.207*10^{-6} (Pa.sec)

Thermal conductivity (k) = 0.0257 (W/mK)

Thermal diffusivity (α) = 2.12*10^{-5} (m^2/s)

<u>Properties of pressurized superheated water (@ 130 ºC and 4.5 bar)</u>

Specific heat (C_p) = 4.2643 (kJ/kgK)

Density (ρ) = 934.925 (kg/m^3)

Viscosity (μ) = 21.294*10^{-5} (Pa.sec)

Thermal conductivity (k) = 0.6838 (W/mK)

<u>Properties of the oil (Paratherm NF)</u>

Temperature (ºC)	**Specific Heat (J/kg)**	**Density (kg/m^3)**	**Thermal Conductivity (W/mK)**	**Viscosity (mPa-s)**
0	1574	953.16	0.1388	15.33
40	1643	917.07	0.1312	7.0
80	1711	881.68	0.1237	3.86
120	1779	846.35	0.1162	2.36
160	1847	810.45	0.1087	1.54
200	1916	773.33	0.1012	1.05
240	1984	734.35	0.0936	0.74
280	2052	692.87	0.0861	0.54
320	2121	648.24	0.0786	0.41

Specific heat (Cp) = 1.7073 T + 1574.3 (J/kgK)

Density (ρ) = -0.9841 T + 960.06 (kg/m^3)

Viscosity (μ) = 0.0132 exp (-0.011 T) (Pa sec)

Thermal conductivity (k) = -0.0002 T + 0.1388 (W/mK)

ANNEX B: Nameplate of the Boiler

	FERROLLI CE
Type	Prex.Asl 1740
Safety Accessories	493/14-492/14
	01780020
Serial No/Year	8045/2014
Fuel	/// Ltr
Rated Heat Output	1740 kW
Rated Heat Input	1933 kW
Design Pressure	4.9 Bar
Max.Working Temperature	158^{o}C
Min/MaxDesign Temperature	0-250 ^{o}C
Hydraulic Test Pressure/Date	0.57/26-02-14
Min Level Content	/// Ltr
Total Content	2600 Ltr
Order No-	05837uax

ANNEX C: Solar Resource Model Simulation Program

This program is written for one month and can be used for other months by changing sunshine hours and representative days. Plot commands are not included for the sake of clarity.

#Sunshine hours

[Jan	Feb	Mar	Apr	May	June	July	Aug	Sep	Oct	Nov	Dec]
[8.8	10.3	8.7	7.8	8.3	8.0	6.1	7.1	7.5	8.8	8.7	9.4]

#Representative days

[17 47 75 105 135 162 198 228 258 288 318 344]

```
from scipy import *
from numpy import *
from pylab import *


#Initializing constants

ISC = 1367.0  #Solar constant
PSI = 8.54    #Latitude of the location
N   = 17.0    #Representative day
ns  = 8.8     #Sunshine hours

#Defining global variables

GAMMA =0.0   #Declination angle
OS    = 0.0   #Sunset hour angle
Ns    = 0.0   #Number of daylight hours
A1    = 0.0
B1    = 0.0
A2    = 0.0   #Regression constants
B2    = 0.0
HO    = 0.0   #Daily extraterrestrial radiation
H     = 0.0   #Monthly average daily radiation
HD    = 0.0   #Monthly average daily diffuse radiation
HB    = 0.0   #Monthly average daily diffuse radiation

OMEGA= [0.0]*86400 #Hour angle (for each second) of the day
I     = [0.0]*86400 #Monthly average instantaneous global radiation
ID    = [0.0]*86400 #Monthly average instantaneous diffuse radiation
IB    = [0.0]*86400 #Monthly average instantaneous diffuse radiation
```

```
# Functions

def calculateOMEGA(sec):
    return (15.0/3600)*(sec-43200)
def calculateI(H,A2,B2,OMEGA,OS):
    return max(H*math.pi/(24)*(A2+B2*math.cos(OMEGA
          *math.pi/180))*(math.cos(OMEGA*math.pi/180)-
           math.cos(OS*math.pi/180))/(math.sin(OS*math.pi/180)
          -OS*math.pi/180*math.cos(OS*math.pi/180)),0)
def calculateID(HD,A2,B2,OMEGA,OS):
    return calculateI(HD,A2,B2,OMEGA,OS)
def calculateIB(I,ID):
    return I-ID
def calculateGamma(n):
    return 23.45*math.sin((360*(284+n)/365.0)*math.pi/180)
def calculateOS(psi,gamma):
    return math.acos(-math.tan(psi*math.pi/180)*math.tan
                     (gamma*math.pi/180))*180/math.pi
def calculateNS(os):
    return 2.0/15*os
def calculateA1(psi,ns,NS):
    return -0.11 + 0.235 *math.cos(psi *math.pi/180) + 0.323*(ns/NS)
def calculateB1(psi,ns,Ns):
    return 1.449 - 0.533 *math.cos(psi *math.pi/180) - 0.694*(ns/Ns)
def calculateA2(os):
    return 0.409 + 0.5016*math.sin((os - 60)*math.pi/180)
def calculateB2(os):
    return 0.6609 - 0.4767*math.sin((os - 60)*math.pi/180)
def calculateHO(isc,n,psi,gamma,os):
    return 24*isc/math.pi*(1+0.033*math.cos(360*n/365*math.pi/180)*
          (math.cos(psi*math.pi/180)*math.cos(gamma*math.pi/180)
           *math.sin(os*math.pi/180)+math.pi*os/180*
           math.sin(psi*math.pi/180)*math.sin(gamma*math.pi/180)))
def calculateH(HO,a1,b1,ns,NS):
    return HO*(a1+b1*(ns/NS))
def calculateHD(H,ns,NS):
    return H*(0.931-0.814*(ns/NS))

def main():
    GAMMA = calculateGamma(N)
    OS    = calculateOS(PSI,GAMMA)
    Ns    = calculateNS(OS)
    A1    = calculateA1(PSI,ns,Ns)
    B1    = calculateB1(PSI,ns,Ns)
    A2    = calculateA2(OS)
    B2    = calculateB2(OS)
    HO    = calculateHO(ISC,N,PSI,GAMMA,OS)
    H     = calculateH(HO,A1,B1,ns,Ns)
    HD    = calculateHD(H,ns,Ns)
```

```
 for sec in range(86400):
        OMEGA[sec]  =(calculateOMEGA(sec))
        I[sec]      =(calculateI(H,A2,B2,OMEGA[sec],OS))
        ID[sec]     =(calculateID(HD,A2,B2,OMEGA[sec],OS))
        IB[sec]     =(calculateIB(I[sec],ID[sec]))


def getIB():
    return IB  #Exporting beam radiation

if __name__ ==  "__main__":
    main()
```

ANNEX D: Collector Simulation Program

The following program is written for collector performance analysis. The solar radiation data is imported from solar resource model code. The code is based on the chapter 4 and the finite difference method formulation in Chapter 5. Result output files are text files and their plot commands are not presented here for the sake of brevity.

```
import math
import Beam radiation

#Receiver geometrical parameters

Dabs_e   = 0.07     #Absorber outer diameter
Dabs_i   = 0.065    #Absorber inner diameter
Dgc_e    = 0.125    #Glass outer diameter
Dgc_i    = 0.115    #Glass inner diameter
Aap      = 5.5*2    #Aperture area per unit length (2 modules)
Aabs_i   = math.pi* Dabs_i             #Inner surface area of the absorber
Acabs_i  = (math.pi*Dabs_i**2)/4       #Cross sectional area of absorber

#Volume of the absorber per unit length
Aabs     = math.pi*( Dabs_e**2-Dabs_i**2)/4

 #Volume of the glass per unit length
Agc      = math.pi*( Dgc_e**2-Dgc_i**2)/4

#Receiver optical properties

AlphaAbs = 0.95  #Absorber absorbptance
Alphagc  = 0.02  #Glass absorptivity
Eabs     = 0.095 #Absorber emittance
Tg       = 0.95  #Glass transmitance
Egc      = 0.84  #Glass emittance

sigma    = 5.67*pow(10,-8) #Stafen Boltzman constant
g      = 9.81              #Gravitational constant


#Thermo-physical properties of absorber

Cabs   = 435.0   #Specific heat
Rho_abs= 8073    #Density

#Thermo-physical properties of glass-cover

Cgc    = 500     #Specific heat
```

```
Rho_gc = 2000    #Density


#Mass flowrate

m_HTF = 0.39     #can be changed as required

#Primary mirror and CPC optical properties

l      = 0.94   #Primary mirror reflectivity
r      = 0.94   #Intercept factor

#Defining beam radiation

IB   = [0.0]*86400

#Air properties

Rho_AIR_amb = 1.1614
K_AIR_amb   = 0.0263
C_AIR_amb   = 1007.0
mu_AIR_amb  = 1.846*pow(10,-5)

#Discretization..(Can be changed as required)

dz     = 0.25
length = 8
n      = length/dz+1    #33 nodes in this case

#Accepting Beam radiation from solar-resource code

def init_IB():
    Beam radiation.main()
    return Beam radiation.getIB()
IB   =init_IB()

# HTF thermo-physical properties

def Rho_HTF(T):    #Density
    T=T-273.15     #Degree Kelvin to degree Celsius
    return (-0.9841*T + 960.06)

def V_HTF(T):      #Kinematic viscosity
    T=T-273.15
    return = (0.0132 * pow(math.e,(-0.011 T)))

def C_HTF(T):      #Specific heat
    T=T-273.15
    return (1.7073*T + 1574.3)
```

```
def K_HTF(T):      #Thermal conductivity
    T=T-273.15
    return (-0.0002*T + 0.1388)

     #Defining functions

#Absorber temperature

def calculateTAbs(A,B,C,D,Tabs,QAbs,Tgc,THTF):
    return ((1-B-C-D)*Tabs)+(A*QAbs)+((B+C)*Tgc)+(D*THTF)

#Glass-cover temperature

def calculateTgc(H,I,J,Tgc,Tabs):
    return ((1.0-H-I-J)*Tgc) + ((1.0*H*Tabs)) + (1.0*(I+J)*Tamb)

#HTF temperature

def calculateTHTF(THTF,E,Tabs,F,THTF1):
    return ((1.0-E-F)*THTF) + (E*Tabs) + (F*THTF1)

#Absorbed energy

def calculateQAbs(IB):
    return IB*Aap*AlphaAbs*l*Tg*r*IAM

#A
def calculateA():
    return (1/(Rho_abs*Cabs*Aabs))

#B
def calculateB(Tabs,Tgc):
    V_Air   =  mu_AIR_amb/Rho_AIR_amb  #Kinematic viscosity of air
    Pr_air  = mu_AIR_amb/(C_AIR_amb*K_AIR_amb) #Prandtl number
    alphaAir=K_AIR_amb*(Rho_AIR_amb*C_AIR_amb) #Thermal diffusivity
    Ral     =(g*(1/(Tgc+Tabs))*(Tabs-Tgc)/(V_Air*alphaAir)) #Reylen number
    Rac     =(pow(math.log(Dgc_i/Dabs_e),4)*Ral)/(pow((pow(Dabs_e,-3/5)
             +pow(Dgc_i,-3/5)),5))
    KeffAir =0.386*pow((Pr_air/(0.861+Pr_air)),1/4)*pow(Ral,1/4)*K_AIR_amb
    hc_int  =2*math.pi*KeffAir/(Dabs_e*(math.log(Dgc_i/Dabs_e)))
    return((math.pi*Dabs_e*hc_int)/(Rho_abs*Cabs*Aabs))

#C
def calculateC(Tabs,Tgc):
    return(math.pi*Dabs_e*((sigma*((pow(Tabs,2)+pow(Tgc,2))*(Tabs+Tgc))
            /((1/Eabs)+((1-Egc)/Egc)*(Dabs_e/Dgc_i))))/(Rho_abs*Cabs*Aabs))

#D
def calculateD(THTF):
    V_htf   = V_HTF(THTF)
```

```
    K_htf   = K_HTF(THTF)
    Rho_htf = Rho_HTF(THTF)
    C_htf   = C_HTF(THTF)
    Re_HTF = 4*(m_HTF)/(math.pi*Dabs_i*V_htf*Rho_htf) #Reynholds number
    f = pow(1.82*math.log(Re_HTF,10)-1.64,-2)         #Friction factor
    pr_htf = (V_htf*Rho_htf*C_htf)/K_htf              #Prundtl number
    Nu_abs_i = f/8*(Re_HTF-1000)*pr_htf/(1+12.7*math.sqrt(f/8)
              *(pow(pr_htf,2/3)-1))                   #Nusselt number
    return(math.pi*Dabs_i*(Nu_abs_i*K_htf/Dabs_i)/(Rho_abs*Cabs*Aabs))

#E
def calculate(THTF):
    CHTF = C_HTF(THTF)
    V_htf   = V_HTF(THTF)
    K_htf   = K_HTF(THTF)
    Rho_htf = Rho_HTF(THTF)
    C_htf   = C_HTF(THTF)
    Re_HTF = 4*(m_HTF)/(math.pi*Dabs_i*V_htf*Rho_htf)
    f = pow(1.82*math.log(Re_HTF,10)-1.64,-2)
    pr_htf = (V_htf*Rho_htf*C_htf)/K_htf
    Nu_abs_i = f/8*(Re_HTF-1000)*pr_htf/(1+12.7*math.sqrt(f/8)
              *(pow(pr_htf,2/3)-1))
    return (Aabs_i*(Nu_abs_i*K_htf/Dabs_i)/(Rho_htf*CHTF*Acabs_i))

#F
def calculateF(THTF):
    rho_htf = Rho_HTF(THTF)
    return m_HTF/(rho_htf*Acabs_i*(dz))

#H
def calculateH(Tabs,Tgc):
    V_Air=mu_AIR_amb/Rho_AIR_amb
    Pr_air=mu_AIR_amb/(C_AIR_amb*K_AIR_amb)
    alphaAir=K_AIR_amb*(Rho_AIR_amb*C_AIR_amb)
    Ral=(g*(1/(Tgc+Tabs))*(Tabs-Tgc)/(V_Air*alphaAir))
    Rac=(pow(math.log(Dgc_i/Dabs_e),4)*Ral)/(pow((pow(Dabs_e,-3/5)
        +pow(Dgc_i,-3/5)),5))
    KeffAir=0.386*pow((Pr_air/(0.861+Pr_air)),1/4)*pow(Ral,1/4)*K_AIR_amb
    hc_int=2*math.pi*KeffAir/(Dabs_e*(math.log(Dgc_i/Dabs_e)))
    return((math.pi*Dabs_e*((sigma*((pow(Tabs,2)+pow(Tgc,2))
            *(Tabs+Tgc))/((1/Eabs)+((1-Egc)/Egc)*(Dabs_e/Dgc_i))))
             +math.pi*Dabs_e*hc_int)/(Rho_gc*Cgc*Agc)

#I
def calculateI():
    prAir_amb = mu_AIR_amb*C_AIR_amb/(K_AIR_amb)
    ReDEnv = Rho_AIR_amb*Vwind*Dgc_e/(mu_AIR_amb)
    NUDEnv_e  = (0.3+0.62*pow(ReDEnv,1/2.0)*pow(prAir_amb,(1/3.0))
                /pow((1+(0.4/pow(prAir_amb,2/3.0))),(1/4.0)))
                *(pow((1+pow((ReDEnv/282000.0),5/8.0)),4/5.0))
```

```
    hc_ext = (NUDEnv_e*K_AIR_amb)/Dgc_e  #External convection
    return(math.pi*Dgc_e*hc_ext)/(Rho_gc*Cgc*Agc)


#J
def calculateJ(Tgc):
    hr_ext =(Egc*sigma*(pow(Tgc,4)-pow(Tsky,4)))/(Tgc-Tamb)
    return (math.pi*Dgc_e*hr_ext)/(Rho_gc*Cgc*Agc)

#Useful heat

def calculateQu(THTFout):
    result = m_HTF * C_HTF(THTFout)*(THTFout-423.15)
    if(result<0):
        return 0
    return result

#Instantaneous efficiency

def calculateEff(IB,Qu):
    if(IB==0):
        return 0;
    return Qu/(Aap*8.0*IB)

#Boundary conditions

Tgc_init  = 298.15 #Glass cover
Tabs_init = 310.15 #Absorber
THTF_init = 423.15 #Heat transfer fluid

#Initializing constants of finite difference formulation

A = 0.0,B = 0.0,C = 0.0,D = 0.0,E = 0.0,F = 0.0,H = 0.0,I = 0.0,J = 0.0

QAbs = 0.0

Tgc  = [[0.0 for y in range(86400)] for z in range(n)]
Tabs = [[0.0 for y in range(86400)] for z in range(n)]
THTF = [[0.0 for y in range(86400)] for z in range(n)]
QU   = [0.0]*86400 #useful heat
Eff  = [0.0]*86400 #Instantaneous efficiency

def main():
    tgc  = open("result\\TGC\\1.txt","w")
    thtf = open("result\\THTF\\1.txt","w")
    tabs = open("result\\TABS\\1.txt","w")         #Result output files
    qu   = open("result\\QU\\1.txt","w")
    eff =  open("result\\Eff\\1.txt","w")
```

```
for sec in range(86400):
       for node in range(n):

           if sec==0:
               Tabs[node][sec] = Tabs_init
               Tgc[node][sec]  = Tgc_init
               if(node==0):
                   THTF[node][sec] = 423.15
               else:
                   THTF[node][sec] = THTF_init
               if(node==32):
                   QU[sec] = calculateQu(THTF[node][sec])
                   Eff[sec]= calculateEff(IB[sec],QU[sec])
                   qu.write(str(QU[sec])+"\n")
               A    = calculateA()
               B    = calculateB(Tabs[node][sec],Tgc[node][sec])
               C    = calculateC(Tabs[node][sec],Tgc[node][sec])
               D    = calculateD(THTF[node][sec])
               QAbs = calculateQAbs(IB[sec])
               H    = calculateH(Tabs[node][sec],Tgc[node][sec])
               I    = calculateI()
               J    = calculateJ(Tgc[node][sec])
               E    = calculate(THTF[node][sec])
               F    = calculateF(THTF[node][sec])
               tabs.write(str(Tabs[node][sec])+"\n")
               tgc.write(str(Tgc[node][sec])+"\n")
               thtf.write(str(THTF[node][sec])+"\n")
           else:


               Tabs[node][sec]=calculateTAbs(A,B,C,D,Tabs[node][sec-1],
                               QAbs,Tgc[node][sec-1],THTF[node][sec-1])
               Tgc[node][sec] = calculateTgc(H,I,J,Tgc[node][sec-1],
                                Tabs[node][sec-1])
               if(node==0):
                   THTF[node][sec] = 423.15
               else:
                   THTF[node][sec] = calculateTHTF(THTF[node][sec-1],E,
                                     Tabs[node][sec-1],F,THTF[node-1][sec-1])

               A    = calculateA()
               B    = calculateB(Tabs[node][sec],Tgc[node][sec])
               C    = calculateC(Tabs[node][sec],Tgc[node][sec])
               D    = calculateD(THTF[node][sec])
               QAbs = calculateQAbs(IB[sec])
               H    = calculateH(Tabs[node][sec],Tgc[node][sec])
               I    = calculateI()
               J    = calculateJ(Tgc[node][sec])
               E    = calculate(THTF[node][sec])
               F    = calculateF(THTF[node][sec])
```

```
                if(node==32):
                    QU[sec] = calculateQu(THTF[node][sec])
                    Eff[sec]= calculateEff(IB[sec],QU[sec])
                    qu.write(str(QU[sec])+"\n")
                    tabs.write(str(Tabs[node][sec])+"\n")
                    tgc.write(str(Tgc[node][sec])+"\n")
                    thtf.write(str(THTF[node][sec])+"\n")

    tabs.close()
    tgc.close()
    thtf.close()
    qu.close()
    eff.close()
if __name__ ==  "__main__":
    main()
```

ANNEX E: Storage Simulation Program

```
import math
#import matplotlib as plt

#Parameters of CTES

d_i=0.026      #Inner diameter of one element
d_o=0.130      #Outer diameter of one element

a=0.013        #Inner radius of one element
b=0.065        #Outer radius of one element

#Cross-sectional area of the pipe
s_HTF=(math.pi*d_i**2)/4

#Inner surface area of the pipe
p=math.pi*d_i

#Solid/concrete volume per unit length
s_s=math.pi*(d_o**2-d_i**2)/4

#Discretizing Computational domain
L=10
n=41
dz=0.25
dt=1

#HTF thermo-physical properties @ average temperature

Rho_HTF=891.5           #Density
V_HTF=0.3706*pow(10,-6) #Kinematic viscosity
C_HTF=2002.5            #Specific heat capacity
k_HTF=0.1099            # Thermal conductivity

#Concrete thermos-physical properties
Rho_c=3100 #Density
C_c=1180   #Specific heat capacity
K_c=2.65   # Thermal conductivity

# mass flow rate of HTF
m=0.065  #can be changed as required

#velocity of HTF
U=m/(Rho_HTF*s_HTF)

 #Reynholds number of HTF
Re = 4*(m)/(math.pi*d_i*V_HTF*Rho_HTF)
```

```
 #Friction factor of HTF
f = pow(1.82*math.log(Re,10)-1.64,-2)

 #Prandtl number of HTF
pr = (V_HTF*Rho_HTF*C_HTF)/k_HTF

 #Nusselt number of HTF
Nu = (f/8)*(Re-1000)*pr/(1+12.7*math.sqrt(f/8)
      *(pow(pr,2/3)-1))

#Convective heat transfer coefficient
h_HTF=Nu*k_HTF/d_i

#Effective heat transfer coefficient
h_E=1/((1/h_HTF)+((1/K_c)*((4*a*b**4*math.log(b/a)
    -3*a*b**4+4*a**3*b**2-a**5)/4*pow((b**2-a**2),2))))

#Constants of finite difference formulation
x=U*dt/dz
y=h_E*dt*p/(Rho_HTF*s_HTF*C_HTF)
z=h_E*p/(Rho_c*s_s*C_c)

# HTF temperature
def calculateT_HTF(T_HTF,T_HTF1,T_s):
   return ((1-x-y)*T_HTF+x*T_HTF1+y*T_s)

#Solid/Concrete temperature
def calculateT_s(T_s,T_HTF):
   return ((1-z)*T_s+z*T_HTF)


#Boundary conditions
Ts_init = 422.15
THTF_init = []

#Accepting HTF temperature from collector outlet for
January 17 (Note that it is also similar for other months)
THTFfile = open("1.txt","r")
for k in range(86400):
   if(k<21600):
      for l in range (33):
         THTFfile.readline()
   elif (k >= 21600 and k<64800):
      for l in range (33):
         if(l==32):
            THTF_init.append(float(THTFfile.readline()))
         else:
            THTFfile.readline();
   else:
      break
```

```
T_s =  [[0.0 for q in range(43200)] for j in range(n)]
T_HTF =[[0.0 for q in range(43200)] for j in range(n)]


def main():
    file1 = open("T_stm1.txt","w")  #Saving result files (for first month here)
    file2 = open("T_HTFm1.txt","w")
    for sec in range(43200):
       for node in range(n):

         if sec==0:
            T_s[node][sec] = Ts_init
            if(node==0):
                  T_HTF[node][sec] = THTF_init[sec]
            else:
                  T_HTF[node][sec] = 423.15
            file1.write(str(T_s[node][sec])+"\n")
            file2.write(str(T_HTF[node][sec])+"\n")
         else:
               T_s[node][sec] = calculateT_s(T_s[node]
               [sec-1],T_HTF[node][sec-1])
               if(node==0):
                   T_HTF[node][sec] = THTF_init[sec]
               else:
                  T_HTF[node][sec]=calculateT_HTF(T_HTF[node]
                  [sec-1],T_HTF[node-1][sec-1],T_s[node][sec-1])
               file1.write(str(T_s[node][sec])+"\n")
               file2.write(str(T_HTF[node][sec])+"\n")


    file1.close()
    file2.close()

if __name__ ==  "__main__":
    main()
```